

2017

Electromechanical Shape Memory Alloy Actuators for Blood Extraction

Berka, Martin

Berka, M. (2017). Electromechanical Shape Memory Alloy Actuators for Blood Extraction (Master's thesis, University of Calgary, Calgary, Canada). Retrieved from <https://prism.ucalgary.ca>. doi:10.11575/PRISM/25862
<http://hdl.handle.net/11023/4199>
Downloaded from PRISM Repository, University of Calgary

UNIVERSITY OF CALGARY

Electromechanical Shape Memory Alloy Actuators for Blood Extraction

by

Martin Jacob Berka

A THESIS

SUBMITTED TO THE FACULTY OF GRADUATE STUDIES
IN PARTIAL FULFILMENT OF THE REQUIREMENTS FOR THE
DEGREE OF MASTER OF SCIENCE

GRADUATE PROGRAM IN ELECTRICAL ENGINEERING

CALGARY, ALBERTA

SEPTEMBER, 2017

© Martin Jacob Berka 2017

Abstract

This thesis concerns the design, prototyping and testing of a series of compact electromechanical actuators for drawing capillary blood for analysis by the e-Mosquito wearable, autonomous glucose monitoring system for diabetes. All the designs used contracting shape memory alloy wires, fixed geometry and millimetre-scale moving parts, primarily to extend a disposable lancet needle from the device and into the skin. The lancet was to enter the skin at an acute angle that increased to 90° at full extension, with the goal of increasing blood flow. Attention was paid to isolation and replaceability of external parts, improving manufacturability and increasing actuator power. Satisfactory control and extension of the lancet along the intended path were achieved, leading to the conclusion that the increased elastic response of skin makes angled needle insertion impractical and to the investigation of other techniques for blood sampling with autonomous devices.

Preface

This thesis is original, unpublished, independent work by the author, M. Berka. Testing of the prototypes reported in Chapter 4, conducted under the supervision of Principal Investigator Martin Mintchev and Student Co-Investigator Gang Wang, was covered by Ethics Certificate number REB16-1060, “Evaluating Efficacy of a Wristwatch-type Minimally Invasive Blood Sampling Device Prototype - the eLeech”, issued by the University of Calgary Conjoint Health Research Ethics Board on August 22, 2016.

Acknowledgments

I thank my supervisor, Professor Martin P. Mintchev, for opening this area of research to me, and for his patience throughout many research iterations and setbacks. I also thank my co-supervisor — Professor Orly Yadid-Pecht — for her oversight and support.

I am grateful to the Johnson & Johnson Diabetes Foundation, the Alberta Diabetes Institute, the National Sciences and Engineering Research Council of Canada for funding the e-Mosquito project, and to CMC Microsystems for providing low-cost access to SolidWorks computer-assisted design software. Individually, I thank the Cosmopolitan International Club of Calgary for supporting my individual work with the Gerald L. Weber scholarship.

I thank my fellow students and lab members throughout the project — Michael D. Poscente, Thiago Valentin de Oliveira, Calena Marchand, Robert Wilkes, Nathan Kelly Ursenbach and especially Gang Wang — for their interest, time, insight and support.

This thesis is dedicated to my family —
Stanislaw, Anna, Jacek, Christine and Andrew Berka,
and grandparents living and departed —
without whom I would never have taken any of the
thousand steps of this wonderful journey.

Table of Contents

Abstract	ii
Preface	iii
Acknowledgments.....	iv
Dedication.....	v
Table of Contents.....	vi
List of Tables.....	viii
List of Figures and Illustrations.....	ix
List of Symbols, Abbreviations and Nomenclature.....	xii
Chapter 1: Introduction.....	1
Techniques for blood glucose measurement	2
Introduction to the prior system	5
Skin structure, insertion force and blood volume.....	8
Means of microactuation	13
Shape memory effect.....	15
Scope and requirements for redesign	21
Chapter 2: Materials and methods	23
Software.....	23
3D printing	24
Reliability	26
Fine features	27
CNC milling	30
Positioning and workholding.....	32
Toolpath planning.....	34
External production	35
Chapter 3: Initial translating-rotating designs.....	37
Early concepts	37
In vitro testing	43
Chapter 4: Translating-rotating refinements	50
Integration design	50
Multi-track design	57
Channel optimization	62

Parallel and asymmetric wire actuation.....	68
Lancet-holder design	71
Chapter 5: Alternative approaches.....	78
Spring-loaded actuator	78
Finger compressor for blood sampler.....	81
Chapter 6: Directions for future research	84
Bibliography.....	88
Appendix A: R code used in optimization calculations and plots.....	96
Undesired rotational degrees of freedom	96
Simulated lancet paths for ledge-driven rotation	96
Appendix B: Code of absolute-relative G-code converter	98
Appendix C: Manual G-code.....	101
Two-sided base piece	101
Aluminum slider.....	103
One-sided base piece for asymmetric actuator.....	103
Appendix D: Copyright permissions	106
Figures 1, 2 and 33	106
Figure 3.....	106
Figures 15, 21, 22, 24 and 25, and excerpts	107

List of Tables

Table 1: Considered 3D modeling software.....	24
Table 2: Summary of evaluated slicing software for 3D printing.	29
Table 3: List of end mills used with the CNC mill.	31
Table 4: Lancet extension lengths measured during porcine skin penetration testing.....	46
Table 5: Summary of refinement designs discussed in Chapter 4.	84

List of Figures and Illustrations

Figure 1: Side-view representation of the e-Mosquito functional prototype	5
Figure 2: The actuation process for the existing e-Mosquito functional prototype	6
Figure 3: Cross-sectional diagram of the anatomy of the skin, with major layers and features. ©2014 Cancer Research UK.....	8
Figure 4: Cut-away view of the blood vessels of the skin [29].	9
Figure 5: Illustration of the relationship between the nitinol phases of martensite (twinned and detwinned) and austenite.	16
Figure 6: Sample hysteresis loop for the martensitic fraction of an SMA as a function of temperature.	17
Figure 7: Relevant features of the "Replicator 2X" 3-D printer used for prototyping.	24
Figure 8: Key features of the Nomad 883 Pro CNC mill used in prototyping.	30
Figure 9: Features on a PCB milled with the Nomad 883.	31
Figure 10: Screenshot of the custom G-code conversion application	35
Figure 11: A base part printed with a "high-precision" resin.	36
Figure 12: Sample dimensions of a 30-gauge needle welded to a wire crossbar.	37
Figure 13: Dimensions of the sliding rack in the prior e-Mosquito actuator (1.75 mm thick).	37
Figure 14: Sample dimensions of an early slider for driving the crossbar of Fig. 12.	38
Figure 15: Basic concept of guiding a needle into skin using a channel whose geometry alters the angle of the needle relative to the skin as the needle advances.	38
Figure 16: Multi-cross-sectional side view of an early concept for a means of enforcing translation and rotation of the needle-crossbar.	39
Figure 17: Sample schematic of L-shaped needle.	40
Figure 18: Slider design used in first working prototype.	40
Figure 19: Key dimensions of the first physical implementation of the base.	41
Figure 20: Model assembly of the first physical implementation of the base.	41
Figure 21: The revised slider design, shown from below.	42
Figure 22: Key section of the redesigned base.	43
Figure 23: Model of the test assembly, showing SMA wire (red), casing base (grey), slider (green), needle (yellow), and steel wire (black rings).	44
Figure 24: Model of the test assembly used for force testing, with a machined PMMA casing for better visibility.	44
Figure 25: Vertical force-distance characteristic produced with the assembly represented in Fig. 24.	45
Figure 26: Graph of measured lancet extension versus actuation time for light and firm pressure of the test assembly base against porcine skin.	47
Figure 27: Undesired rotation of the lancet in the xz plane, due to channel width exceeding lancet diameter.	49
Figure 28: Undesired rotation of the lancet shank in the xy plane, enabled by a trench width greater than the lancet diameter.	49
Figure 29: Design of a two-cell base floor piece with tabs for press-fit attachment of two base- channel pieces (Fig. 30).	50

Figure 30: A channel piece implementing the press-fit concept, compatible with the floor piece in Fig. 29.50

Figure 31: Initial design of two-cell actuator PCB for in-plane actuator.51

Figure 32: Electrical schematic of the pre-existing control circuitry of the e-Mosquito actuator PCB52

Figure 33: Architecture of the pre-existing, autonomous e-Mosquito wearable, as presented in [27].53

Figure 34: Dimensions of the slider cover, shown from below.54

Figure 35: Isolation milling toolpath generated for bottom side of revised PCB.57

Figure 36: Actuator concept with a revised channel, as presented at IEEE Sensors 2016.57

Figure 37: Dimensions of the revised unified base.58

Figure 38: Dimensions of the revised slider design with three ridges, compatible with Fig. 37. ...59

Figure 39: Bottom side of the milled PCB with one actuator cell attached.61

Figure 40: Cross-section of the channel (yz) as produced by the code of Appendix C.62

Figure 41: Simplified representation of geometry relevant to idealized motion of the lancet during insertion into the skin, based on the channel geometry of Fig. 40.62

Figure 42: Graph of lancet extension rate (3) and angle (2) relative to the skin as functions of translation of the driven part of the lancet;64

Figure 43: Visualization of the path of the lancet during insertion into the skin, for the same geometry as Fig. 42.65

Figure 44: Re-labeled blade concept from the patent application [87].66

Figure 45: Visualization of the path of the lancet, analogous to Fig. 43, when the corner is brought closer to the skin.67

Figure 46: Side view of cutter toolpath for the revised channel.68

Figure 47: Electromechanical concept of parallel current actuation.69

Figure 48: Screenshot of CutViewer Mill (GRZ Software) simulation illustrating the slider as it would be ideally cut by the G-code written for it.70

Figure 49: Examples of wire-pulley arrangements considered for one-sided actuation.71

Figure 50: Alternative needle configurations considered to increase the diameter of the part of the lancet interfacing with the reusable part of the system.72

Figure 51: Bottom view of the lancet-holder design based on Fig. 50d.73

Figure 52: Side, bottom and isometric views of the slider for use with the lancet holder of Fig. 51, with dimensions.74

Figure 53: Dimensions of the base design for use with the sliding lancet holder.75

Figure 54: Bottom view of the (5-mm-long) milled lancet holder with the lancet inserted.76

Figure 55: Bottom view of the milled aluminum slider described in Fig. 52, mounted on the PCB.76

Figure 56: Bottom view of the lancet holder (Fig. 54) and slider (Fig. 55), assembled.76

Figure 57: Lancet holder and latch for the spring-loaded actuator.78

Figure 58: Inside view of the half of the actuator casing with holes.78

Figure 59: Inside view of the half of the actuator casing with pegs.78

Figure 60: Model of the assembled spring-loaded system, in the loaded position.79

Figure 61: Operation sequence for the spring-loaded concept, corresponding to the assembly in Fig. 60.80

Figure 62: Physical implementation of the lancet holder of Fig. 57 for the spring-loaded actuator concept.81

Figure 63: Dimensions of the base for the finger compressor.82

Figure 64: Bottom view of the PMMA wire base for the finger compressor, with SMA wire wrapped around the screws.....83

List of Symbols, Abbreviations and Nomenclature

α	Angle between the needle axis and the skin plane (complement of θ)
η_{Carnot}	Carnot efficiency
θ	Angle between needle axis and axis normal to skin plane
ρ_{wire}	Resistivity of SMA
φ	Angle of undesired rotation of lancet during insertion (φ_{xy} : component of φ enabled by features in the xy plane, etc.)
Ω	Ohms
A_f	Austenite finish temperature
A_s	Austenite start temperature
A_{wire}	Cross-sectional area of wire
I_{wire}	Current through wire
I_{net}	Net current drawn by activated actuator
l	Length of lancet excluding the driven part
l_{wire}	Length of wire supplied by a voltage
M_f	Martensite finish temperature
M_s	Martensite start temperature
P	Power (dissipated)
R_{SMA}	Resistance of SMA
r_{wire}	Radius of wire
t_1	Thickness of the base overhang containing the ledge
t_2	Height of the space in the base below the ledge
V_{app}	Voltage applied
x	Variable position of driven part from starting position during insertion
x	Actuator directional axis representing lateral motion of the slider
X	CNC machine axis pointing from the left side of the build plate to the right
x_{ledge}	Horizontal distance of rotation ledge from starting point of lancet shank
y	Actuator axis parallel to the translation of the slider.
Y	CNC axis pointing from the front of the build plate to the back
z	Actuator axis normal to the skin.
Z	CNC axis pointing upwards from the build plate.
ABS	Acrylonitrile butadiene styrene
base	The bottom layer of the e-Mosquito, adjacent to the skin.
CAD	Computer-aided design
CAM	Computer-aided manufacturing
CGM	Continuous glucose monitoring
channel	The opening through which the lancet extends from the e-Mosquito.
CNC	Computer numerical control
DC	Direct current
DFM	Design for manufacturability
driven part	The part of the lancet interfacing with the slider and never emerging from the base.
DOF	Degree of freedom
e-Mosquito	Electronic Mosquito

EAP	Electroactive polymer
FDA	Food and Drug Administration
FDM	Fused deposition modeling
FGM	Flash glucose monitoring
gf	Grams-force
GOx	Glucose oxydase
HIPS	High-impact polystyrene
LADA	Latent autoimmune diabetes in adults
lancet	A solid lancet needle, typically beveled.
ledge	A protruding edge in the ceiling of the channel which drives rotation of the lancet.
Li-ion	Lithium ion
LOC	Length of cut (cutting bit parameter)
mAh	Milliampere-hour
MDI	Manual Data Input
MEMS	Microelectromechanical system
mmHg	Millimetre of mercury (standard in medicine; ~133.3 pascals)
NiTiNOL	Nickel titanium Naval Ordnance Laboratory
OLED	Organic light-emitting diode
PAD	Peripheral artery disease
PCB	Printed circuit board
PLA	Poly(lactic acid)
PMMA	Poly(methyl methacrylate)
PVDF	Poly(vinylidene fluoride)
PZT	Lead zirconate titanate
SD card	Secure Digital memory card
slider	The component that holds the driven part of the needle and is pulled by the SMA wire.
SMA	Shape memory alloy
SMBG	Self-monitoring of blood glucose
SMP	Shape memory polymer
T1DM	Type 1 diabetes mellitus
T2DM	Type 2 diabetes mellitus
track	A space in the base that accommodates a part of the slider or the driven part of the lancet, the boundaries of this space restricting motion of the driven part.
trench	A long, shallow depression in the bottom of the slider, which holds and moves the needle.
V	Volts
WCS	Work coordinate system

Chapter 1: Introduction

This research was motivated by development of an automated blood sampling system for improved management of diabetes. As of 2014, diabetes mellitus affected an estimated 422 million people worldwide, projected to rise to over 700 million by 2025 [1]. The disease is defined by inadequate cellular absorption of sugars (primarily glucose) from the blood, which leaves the cells with less available energy and the blood with an excessive glucose concentration. Untreated, it results in deteriorating bodily function, with potentially extreme effects including organ failure, blindness and limb loss.

The population of people with diabetes is divided into groups by mechanism [2]:

- Type 1 diabetes mellitus (T1DM) is defined by destruction of the beta cells of the pancreas by the immune system, leading to insufficient production of the hormone insulin.
- Type 2 diabetes mellitus (T2DM) is characterized by insufficient insulin production (without autoimmune destruction) or insufficient response to the hormone by other cells (insulin resistance). It is most directly tied to lifestyle and represents the clear majority of cases.
- A variety of less common mechanisms are associated with genetic disorders, foreign chemicals, pregnancy and other factors.

While T1DM and T2DM were traditionally differentiated by age of onset, with T1DM constituting 5–10% of all cases [3], the autoimmune mechanism has been found to occur over the age of 30, a condition sometimes known as adult-onset T1DM or “latent autoimmune diabetes in adults” (LADA) [4] and accounting for a significant share of people otherwise classified as T2DM [5].

Treatment of mild cases of diabetes may involve improved diet or exercise, coupled with self-monitoring of blood glucose (SMBG) to track efficacy and progression. People with T1DM (including the slower-onset group with LADA) and a share of those with T2DM further require regular external administration of insulin to maintain safe blood glucose concentrations and avoid symptoms. The extra insulin must be carefully timed and dosed to avoid both hyperglycemia and its more acute and potentially fatal counterpart, hypoglycemia. The recommended frequency of SMBG for this group is thus elevated to at least three times per day [2]. The actual frequency of SMBG is overreported, and even so, most patients in studied samples report testing less often than

recommended, with cited reasons including pain, inconvenience and difficulty in extracting enough blood [6], [7]. The prospects of improving management of diabetes, and thus of improving health outcomes, rest on reducing these barriers to SMBG. This requires an in-depth investigation of the available methods of monitoring.

Techniques for blood glucose measurement

The gold standard for accurate measurement of glucose concentration involves collecting a fixed volume of whole blood and allowing the glucose in that volume to participate in a measurable chemical reaction. In an age of electronic devices, this is typically an electrochemical reaction, most often using an electro-oxidation enzyme, such as glucose oxidase (GOx) or a glucose dehydrogenase, and a mediator such as ferricyanide [8]. The reaction releases an electric charge, which may be measured directly (in the case of coulometric glucose meters) or in terms of a resulting current (amperometric) to quantify the glucose present in the known, limited volume of the test strip and thus calculate the glucose concentration. The primary weakness of this method is the need to physically deliver the sample to a test site. The traditional approach for SMBG is to collect blood from a wound made in the fingertip with a lancet needle [6]. Drawbacks include:

- possible contamination of the sample with trace amounts of glucose present on the skin [8], leading to misleading, elevated readings;
- risk of infection and concern about risk of infection [6];
- the short-term pain associated with breaking highly innervated skin [6] and squeezing around the wound site, possibly repeating until adequate blood emerges;
- ongoing pain or discomfort over subsequent days or weeks due to wounds and bruising in the part of the body most used for interaction with and manipulation of foreign objects;
- potential social stigma associated with public self-injury during pricking [6] and with the physical stigma remaining after pricking;
- added difficulty in testing newborn, elderly or hemophobic patients [9].

A non-invasive means of monitoring would increase patient adherence [6], [10] and a number of technologies have been proposed to eliminate or at least reduce the burden. For truly non-invasive measurement, two classes of options exist. The first involves measurement of the tissue response

to energy delivered by the interrogating system. A wide variety of glucose-related phenomena have been investigated [10], [11] including:

- resistance, ion migration or other response to electricity or magnetism;
- emission, polarization, absorption, scattering or other interactions with light of a particular wavelength;
- thermal excitation by light or acoustic wave; and
- nuclear magnetic resonance, rate of regeneration of pigment in the retina, etc. [10].

The second class consists of sensors seeking to chemically access glucose without impinging on bodily tissues. Since it is found in blood, glucose also occurs in other bodily fluids, of which sweat, tears and saliva are accessible outside the body. A variety of products, worn directly on surfaces from which these emit or incorporated into items of clothing or wearable devices, have attempted to deduce blood glucose from these media [9], [10].

Despite decades of effort, no implementation of a non-invasive technology for SMBG has thus far been approved by the United States Food and Drug Administration (FDA) for standalone use in decisions on insulin dosing [10]. This is unsurprising given the difficulty of remotely measuring a modest concentration of one organic molecule in a solution of many others, flowing through a complex network surrounded by yet other organic molecules. Any of these substances could potentially exhibit a glucose-like response for a phenomenon. With the FDA listing over two dozen “known or potential interferents for SMBGs”, non-invasive systems cannot meet its seemingly modest standard of readings usually accurate to within 15% [12].

Accuracy thus far requires a degree of invasiveness. This has traditionally meant direct access to blood, though temporarily implanted sensors can access the interstitial fluid and provide continuous glucose monitoring (CGM) or flash glucose monitoring (FGM, making readings available to the user on-demand, but omitting alarm capacity). Recent versions of commercial CGM systems are beginning to demonstrate errors small enough for direct use of their measurements for insulin dosing decisions [13] and have begun to receive FDA approval for this purpose [14], with European certifications already in place. Weaknesses remain; as CGM sensors:

- require calibration with vascular blood samples obtained by finger-pricking [2], [15] and

- are less accurate when blood glucose levels are extreme or are changing rapidly (e.g., after meals or insulin administration), lagging by “five to twenty minutes” [16].

The latter issue results less from the technology than from the test sites — less sensitive and reasonably accessible locations, such as on the upper arms and abdomen [17]. Finger-pricks rely on capillary blood, while samples encountered at these “alternate test sites” by deeply embedded CGM sensors are a mixture of blood and interstitial fluid (which, intuitively, reflects changes in overall blood glucose concentration more slowly) [10]. Even the blood glucose levels at these sites may be delayed, due to a key factor behind the medical emphasis on pricking of the fingers: blood perfusion. Among capillaries, blood is replaced most quickly in the fingertips and the glucose concentration in blood drawn there can thus be expected to most closely track the concentration in the entire circulatory system. The difference is not fixed, as stimulation of a particular area, such as by rubbing, can substantially increase blood flow and reduce the delay in that area [16]. Studies have found blood glucose levels in capillaries in different locations to be largely the same overall ([7], [17], [18]); throughout the day; the difference is fleeting.

The fingers bear additional benefits as test sites:

- They are frequently uncovered and readily accessible for testing. Excessive bleeding or complications there are unlikely to be overlooked.
- The high density of capillaries [19] and thinness of the skin make it easier to obtain the required blood volume, particularly around the sides of the finger [20].

Medically, the test site is optimal (though not ideal: certain sub-sites of the fingers are subject to concerns about calluses and excessively thin tissue [21], the latter offering less blood and increasing risk of complications due to needle-bone contact). In practice, it is underutilized.

It is not merely a matter of minimizing pain or producing more blood, or else the problem could be fully addressed with a creative handheld device. Regardless of how simple such a device may be to use, there will remain the obstacles of human forgetfulness, busyness, distraction, reluctance, and simple physical ability to manually initiate and operate it. Research at the Low Frequency Instrumentation Laboratory sought a wearable alternative, which would have autonomicity – the ability to test on demand or at any pre-set time – relieving the user of a task and allowing technology to serve in a greater assistive capacity.

Introduction to the prior system

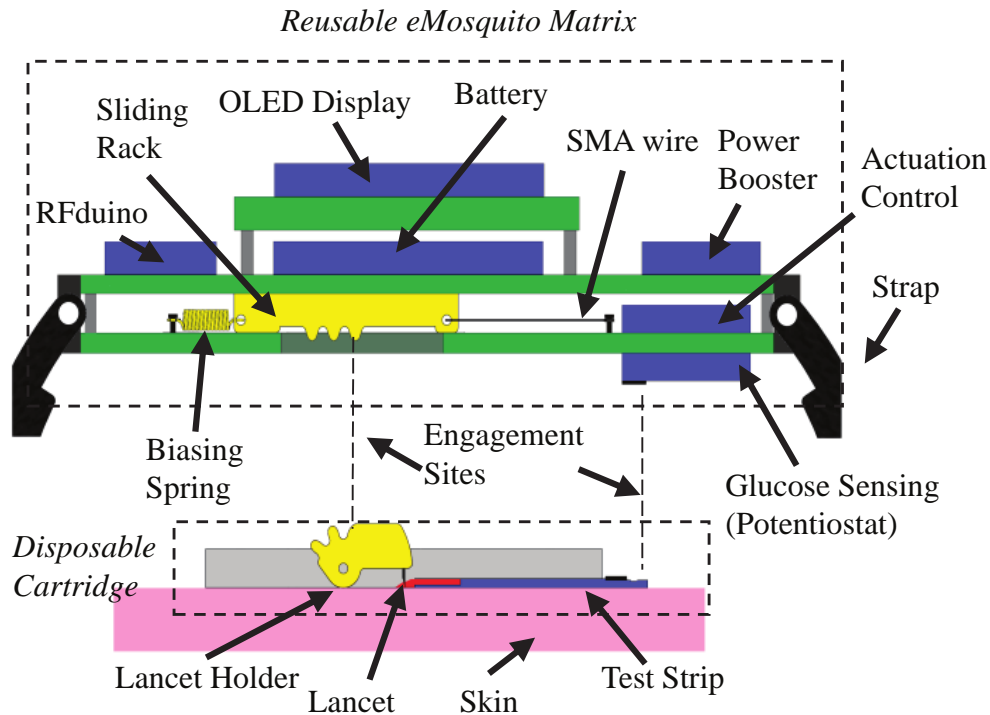


Figure 1: Side-view representation of the e-Mosquito functional prototype, as presented in [27]. ©2016 IEEE.

The e-Mosquito was an autonomous microelectromechanical system (MEMS) with the potential to improve the health of people with diabetes by automating finger-pricking-style blood glucose measurements and minimizing pain and inconvenience [22]–[27]. An initial concept [22], [23] was miniaturized into a wearable prototype resembling a bulky wristwatch. It possessed three layers of printed circuit boards (PCBs) [26], represented in Fig. 1 (all subsequent discussion treats the skin as the horizontal floor of the e-Mosquito system). The top PCB contained display electronics. The one below accommodated a lithium ion (Li-ion) battery, power supply management, data processing and wireless communication electronics (an RFduino Bluetooth module — RFduino, Hermosa Beach, CA, USA). A third PCB contained potentiostat circuitry for glucose sensing on the underside, while the top was occupied by current-control electronics connected to a number of nitinol wires. Each wire was wound around two pulleys (Fig. 2) and passed through one end of a sliding rack, the opposite end of which was pulled by a biasing spring. The rack spurs extended into slots cut through the bottom PCB, interfacing with those on the curved circumference of a lancet holder, which could rotate perpendicular to the plane of the disposable base piece in which

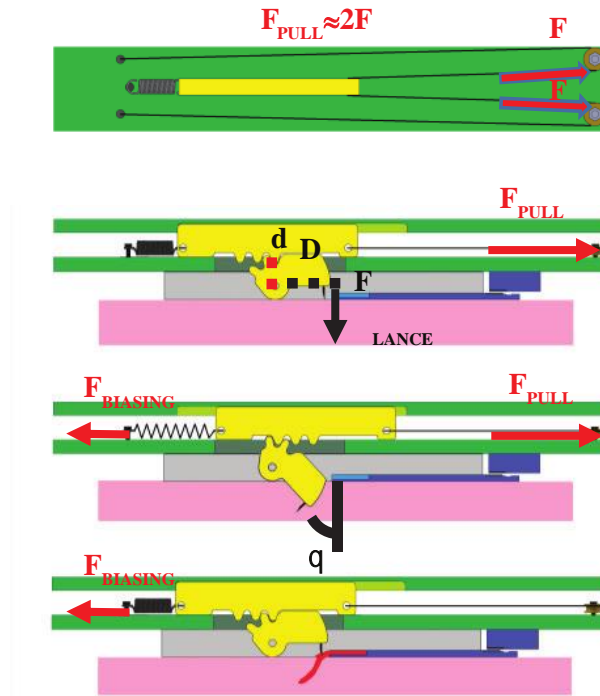


Figure 2: The actuation process for the existing e-Mosquito functional prototype, as presented in [27]. ©2016 IEEE.

it was mounted. A lancet needle was fixed on the arm, pointing down through a slot in the base piece. The PCBs were connected by metal screws and attached to the forearm with a wristwatch strap.[26], [27].

The preferred prototype contained two electromechanical actuators, each consisting of the parts shown in Fig. 2 along with control electronics. A successful blood-testing sequence consisted of the following:

1. The control electronics activated a transistor, supplying current of around 340 mA to the SMA wire in one actuator. The SMA wire was resistively heated and contracted, overcoming the force exerted by the biasing spring and pulling the sliding rack.
2. Gears on the underside of the rack pulled gears on the curved perimeter of the lancet holder, causing the holder to rotate and move the needle downwards.
3. The needle emerged from the bottom of the e-Mosquito casing and pressed against the skin of the wearer, puncturing the outer surface and ideally reaching a capillary blood vessel.

4. After 10 seconds, the electronics halted the supply of power from the transistor, allowing the wire to cool and the spring to retract the slider and thus the needle.
5. A drop of blood would emerge from the wound and be absorbed by the glucose test strip.
6. The altered electrical resistance of the test strip would be measured by the device electronics and displayed on an organic light-emitting diode (OLED) display.

Activating each of the cells at a different time, the e-Mosquito provided automated, sequential *ex vivo* measurements, which could be independently utilized for insulin control or for calibration of CGM systems.

This specific motivation for this research was the fact that needles driven by the e-Mosquito consistently entered the skin, but often failed to draw blood on their own (blood would emerge when the area was squeezed, as is often done by people with diabetes during a manual finger-prick test) [26]. It was hypothesized that a needle inserted into skin at a shallow angle (a large angle θ relative to the vertical) would face lower resistance and could then be straightened (smaller θ) to widen the wound and promote bleeding. The rack-and-pinion mechanism employed by the existing e-Mosquito MEMS, while able to convert the contraction of the nitinol wire into extension of a single-use needle [25], entailed several drawbacks:

- The implementation required two large, moving components, the rack and the lancet holder, arranged vertically. This increased the thickness, and thus the volume, of the prototype.
- The sequence of angles that the needle could assume relative to the skin was limited to one determined by the circular path of the rotating element.
- The needle needed to be attached far from the center of rotation, so that the needle entered nearly perpendicular to the skin and saw little angular change relative to the skin after that. Contrary to the representation of Fig. 2, the lancet holder did not substantially encroach upon the skin, so the range of θ remained small.

In short, the new concept required development of a distinct actuator, beginning with the most fundamental considerations underlying its function — the biomechanics of skin and blood impinged upon by a needle.

Skin structure, insertion force and blood volume

The skin consists of distinct layers of soft tissue: the outer epidermis, the underlying dermis and the subcutaneous tissue (Fig. 3). In inward order, the epidermis consists of:

- a hard layer of dead skin cells – the stratum corneum;
- a layer of dying, hardening squamous skin cells which replenish the stratum corneum – the stratum granulosum;
- the squamous cell layer, consisting of protein-producing keratinocytes – the stratum spinosum; and
- the basal cell layer responsible for division of basal cells to produce keratinocytes, and for production of pigmentation via melanocytes – the stratum basale [28].

The transition between these sublayers is gradual, and the exact composition of the epidermis varies with body site. For example, the skin of the palms and foot soles has an additional, translucent layer of dead cells (the stratum lucidum) between the stratum granulosum and the stratum corneum [28]. The overall thickness of the epidermis ranges from 0.02 to 1.4 mm, thickest on the soles and palms [29], which experience regular wear due to contact with foreign bodies. Callouses may further thicken the stratum corneum.

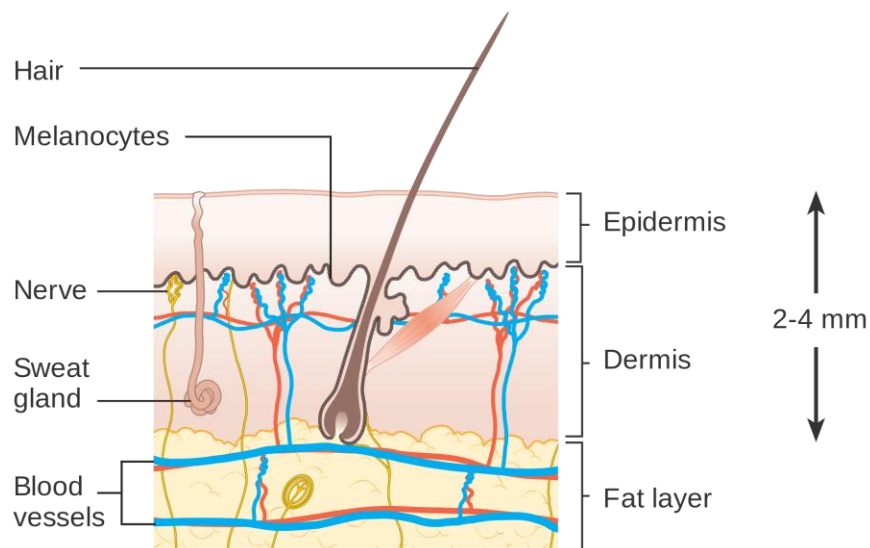


Figure 3: Cross-sectional diagram of the anatomy of the skin, with major layers and features. ©2014 Cancer Research UK.

The epidermis contains nerve endings (also variable in number) but no blood vessels [29]. This ceases to be the case at the lower boundary, where the epidermis meets the upper sublayer of the dermis: the papillary layer. This sublayer has a high density of papillary blood vessel loops [7]. Below lies the thicker reticular layer, with a thinner network of capillary vessels [30] (see Fig. 4). The dermis also contains nerves and the bases of hair follicles and sweat glands).

Larger blood vessels run through the lower part of the reticular layer and the throughout the subcutaneous layer, which contains fat cells and begins 2 to 4 mm below the skin surface (Fig. 3). Injury to these vessels is potentially dangerous, and the needles used for the fingerstick test are generally of a length suitable to penetrate through the epidermis and reach capillary vessels in the upper dermis while leaving veins and arteries intact [7].

This length must be greater than the depth that the needle is intended to reach. An instrument impinging upon skin first causes the skin to deflect away (indent), then rupture when the local yield strength of the skin is exceeded by tension (resistance of the surrounding skin to displacement) or compression (resistance of underlying tissues). A prior publication [25] on the e-Mosquito listed

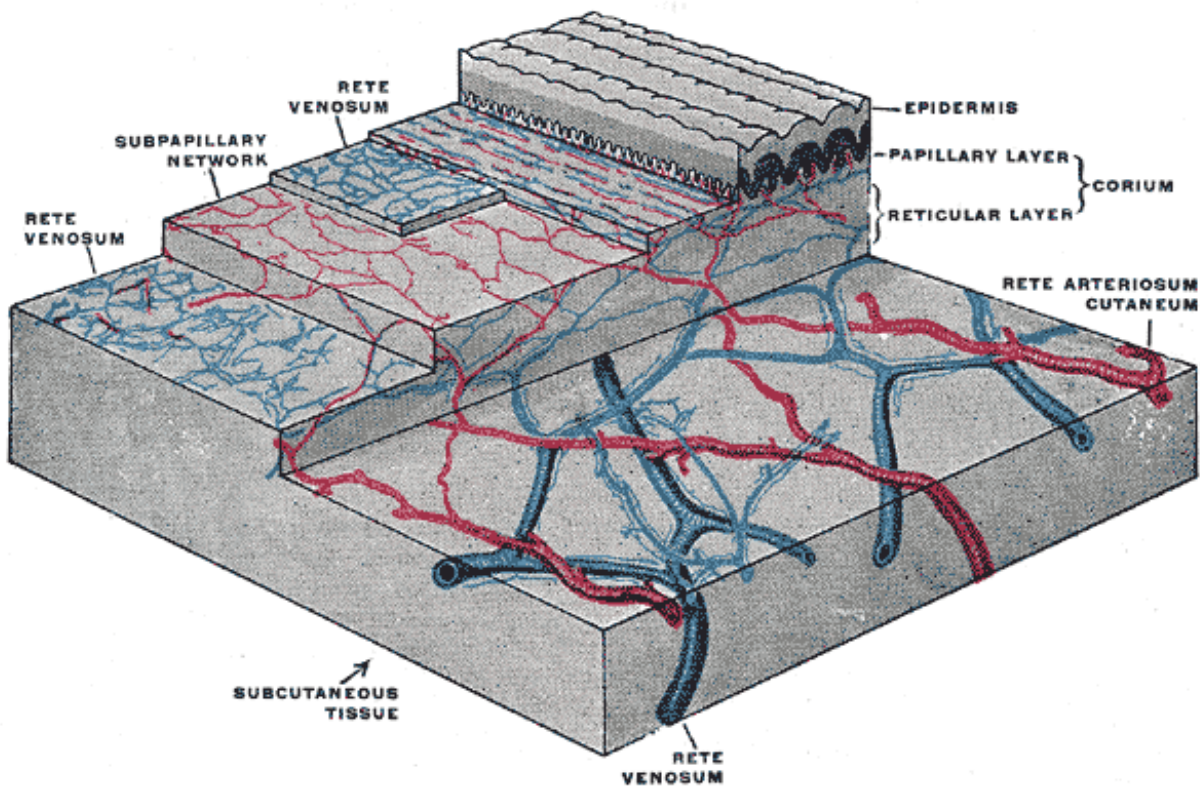


Figure 4: Cut-away view of the blood vessels of the skin [29].

the minimum force needed to penetrate the skin to be 30 gf (grams-force, about 0.29 N) based on the indentation load experienced by a 200 μm (33-gauge) needle entering perpendicular to the skin to a depth of 2.45 mm in [31]. This particular value could not be applied globally: the force required to pierce the skin (i.e., for an instrument to transition from elastically indenting the outer surface to cutting through tissue below it) varies based on a number of factors related to the manner in which the instrument is inserted:

- Large values of standard mechanical properties of different skin layers — thickness, hardness, elastic modulus, etc. — imply greater insertion force. These are known to vary with age, personal history, location on the body [32], [33] and, of course, species [34] ([31] employed chicken skin, an uncommon choice when most skin experiments involve the skin of mammals, human or otherwise).
- A sharper instrument (one able to transmit force to a smaller area, resulting in greater pressure) penetrates more easily, in accord with finding ([34], [35]) that the tip of an instrument entering a soft solid acts as a wedge that propagates a crack, instead of creating a simple cylindrical opening by compressing displaced tissues radially away from the axis. Thus, peak insertion force increases with instrument diameter and tip angle [32]. On the dull extreme, a flat-bottomed punch penetrating a soft solid faces greater resistance relative to its cross-sectional area than a sharp one [35]. Among needles, beveled tips face less resistance than conical ones [34], [36].
- The orientations of local instrument features, such as bevels, alter the distribution of volume of an, affecting the amount of material displaced by an instrument following a given path. A needle inserted into the dura requires less force, and produces a smaller opening, when the bevel is oriented parallel to the dura fibres [37]. Similarly, in the case of angled insertion, downward-facing bevels displaced less tissue (14% smaller width change of accessed blood vessels) and faced less resistance (33% lower peak insertion force) than upward-facing bevels [36]. In both examples, force is reduced because the bevel represents undisplaced volume otherwise occupied by needle material and is oriented so that pressure is applied to a smaller surface of the tissue boundary.
- The angle of insertion relative to the surface of the skin affects the resistance that the instrument will encounter. A needle inserted at a 90° angle ($\theta = 0$) has been found to face

the least resistance, with insertion force increasing markedly as the insertion angle decreases (θ increases) [38].

- Various forms of dynamic insertion reduce the necessary force or at least reduce variability. Multiple studies have reported reduced insertion force with increasing insertion velocity [38], though some found no relation [34]. Rotation [34] and vibration [39], [40] of the instrument have both been associated with reductions.

In effect, any change in the form and motion of an impinging instrument would alter the mechanical resistance of the skin. It is thus unsurprising that a review of the literature [34] identified a range of axial forces, with reported maxima for each contributing force (puncture, cutting, friction) varying by two or more orders of magnitude.

Even when all the above variables are held constant, the behaviour of the skin will vary. Skin is “highly non-linear, anisotropic, viscoelastic and nearly incompressible” [33], exhibiting a variety of properties not considered by basic solid material models.

- Skin adapts to stress on long and short time scales. In the short term, blood drains from an area under relatively higher pressure, and the amount of blood present and rate of draining are affected by microcirculation factors such as the aforementioned response to external stimulation [16]. In the long term, skin adapts to withstand ongoing tension along and compression normal to its surface. Tension in the skin varies in direction and magnitude by location, resulting in tension lines such as Langer lines [33], [41].
- While empirical models based on testing whole samples of skin may treat it as transversely isotropic out of necessity [33], [41], it is known to be at best orthotropic [35] and is modeled as such [33] by more detailed models taking account of microstructure and layers, with the most extensive including dozens of parameters [41].
- With regards to layers, those below the skin are also important: the presence of a firm backing limits deflection and results in a lower penetration force [42]. Outside an *in vitro* setting, this resistance is variable and deflection thus poses a substantial challenge to the ongoing miniaturization of skin-accessing needles [43].
- Water content, due to both whole-body hydration [44] and surface contact with water, as well as treatment with other substances [45], affect stiffness.

One may thus expect the exact same insertion procedure to result in different insertion forces, skin deflections, insertion depths, external and internal wound surface areas, wound volumes, pain levels and (most importantly for the purpose of sampling) blood volumes.

As the mechanics of the skin are unpredictable, a wearable lancing device must supply greater force and extension than are normally required for rupture. As alternate test sites may not produce adequate blood when punctured with finger-pricking lancets [7], a device for sampling there cannot make too many sacrifices with regards to factors that contribute to blood flow. These factors include:

- wide needle diameter [46];
- greater depth of needle insertion [46], [47]; and
- mechanical stimulation of the wound area, which may involve:
 - applying positive pressure away from the wound to drive blood towards it, e.g., “milking” during the standard finger-prick test [21],
 - applying negative pressure (“suction”) at the wound site [7], [47] or
 - (as investigated here) deforming the wound [47] to widen it following insertion of the needle.

Not coincidentally, these factors are also associated with pain [48]. Nerves and microvasculature in the skin are similarly distributed [7] and nociceptors can be activated by compounds found in blood [49]. A degree of force and pain is unavoidable for wounds producing substantial blood volumes.

The mechanical actuator of a blood-sampling wearable faces a unique challenge in delivering force sufficient to consistently puncture the skin while satisfying constraints on size and power consumption.

The matter is simple for manual lancing devices: the force driving the lancing component is typically provided either directly by the user (holding a needle or pressing a trigger) or by the relaxation of a spring loaded with manual power or (for disposable units) during manufacturing. Both forms of actuation are reliable – whether or not the resulting wound bleeds, the ability of direct or stored human power to wound human skin has been demonstrated for millennia, and these

handheld devices are large enough to take advantage of that power source. Of the two approaches, spring-loading is superior in terms of consistent speed of extension and the lesser pain experienced [50] and has become the norm [20]. The major distinction among spring-driven lancing devices involves the mechanical system used – linear motion or cam actuation [20]).

Electrical lancing systems have recently been introduced, controlling needle motion using electromechanical actuators such as solenoids and voice coils. These are more expensive than strictly mechanical systems, but offer finer motion control and potential for integration [20].

Critically, these mechanical and electrical systems are handheld, not wearable, and thus lack autonomy. A manual system will always be dependent on the memory and convenience of the user, and may thus remain unused at important moments regardless of the details of the blood sampling process. To reduce the burden of diabetes instead of providing an extra chore, the technology must be wearable, dependent only on machine memory. This in turn requires miniaturization and a transition to a class of small, muscle-free systems on the verge of microactuation. Subsequent discussion will focus on technologies that can convert energy to motion at smaller scales.

Means of microactuation

Device-driven mechanical actuation has traditionally been electromagnetic (using motors or solenoid systems), pneumatic or hydraulic [51]. While motors and hydraulics are applied in upper-limb prostheses [52], further miniaturization makes them impractical. At the time of development, the smallest commercially available “micromotors” were 3 mm in diameter and intended for phone vibration [53], orders of magnitude too fast (and weak) to drive a needle directly or load a spring. The gear system necessary to provide adequate conversion would add to cost and especially volume. Linear actuators, whether based directly on solenoids or rotary motor gear systems, were thicker and cost far more.

As commercially available electromagnetic actuators producing linear displacement (such as might drive a needle) remain slightly bulky for wearable applications, more compact technologies are required. For the capillary blood sampling attempted by the e-Mosquito, a suitable actuator would need to:

- produce multi-millimetre displacement (sufficient to drive a needle into the skin or load a spring sufficiently to drive such extension at a later time);
- deliver force on the order of at least 10 gf (past work used 30 gf as a benchmark, based on [31]) throughout needle extension to the desired depth;
- occupy sufficiently little volume to allow integration into a compact, limb-worn device, ideally directly with a PCB; and
- consume power available from a rechargeable power source that is also compact enough for said device, without the use of bulky additions such as a high-gain DC/DC boost converter.

The range of available technologies consisted of ones normally employed in MEMS, even though the required displacements and forces for the desired blood extraction remained in the range of “macroactuators”. The major classes of phenomena in MEMS actuation are electrostatic, piezoelectric, thermal and magnetic [54]. The diverse technologies within these classes are compared by plots relating specific parameters [51], [54], those showing force-displacement (stress-strain) being of greatest interest. Actuators based on a number of technologies could potentially operate in the desired range [54]:

- Thermal bimorph actuators are based on the differing thermal expansion coefficients of solid layers of two adjacent materials subjected to heating. While good displacements are available, the work product is low in compact applications, as is efficiency [51].
- Electroactive polymers (EAPs) change shape in response to electric current or voltage. EAPs provide extremely large strains and efficiency, at the cost of high voltages impractical in wearable devices [55]. They remain an area of active research, and barriers to their use may be reduced in the future.
- Piezoelectric materials, e.g., lead zirconate titanate (PZT), are the ceramic counterparts of EAPs, varying in volume in response to electricity. Actuators based on these are similarly fast and efficient, exhibiting much lower strains and voltages. Early versions of the e-Mosquito used PZT “piezobenders” (piezoelectrically driven bimorph cantilevers), the electrically induced bending of which drove a central platform and needle downwards [22]–[24]. The technology was expensive, (still) required substantial voltage, and most importantly, dropped in output force as it was scaled down [24].

- The most recent implementation abandoned PZT in favour of another mature actuation technology bearing similarities to thermal bimorphs, EAP and piezoelectric ceramics: alloys exhibiting the shape memory effect.

Shape memory effect

Most broadly, the shape memory effect (SME) describes the ability of a material to recover from an apparently non-elastic deformation and return to an earlier geometry — under the influence of an external stimulus [56]. This outcome-based definition overlaps with many mechanism-based classifications, with representatives in each major class of materials.

- Shape memory ceramics include piezoelectric materials, the broader class of electrostrictive materials (deforming in response to electricity, without the inverse transformation), and ones that transform in response to temperature.
- Shape memory polymers (SMPs) may respond to stimuli such as temperature, light, chemicals [56], electricity (EAPs) and magnetic fields [57].
- Shape memory alloys (SMAs) primarily respond to temperature.

Despite being limited to a single phenomenon, SMAs are by far the most common in practical actuation. The drawbacks of piezoelectric ceramics apply to other shape memory ceramics along with the advantages. SMPs offer high deformation and force-to-weight, but are quite weak compared to SMAs [56]–[58] — to the point that ones recently developed in a lab and able to lift a 50-gram weight were described as having “high force capabilities” [58]. Furthermore, any electromechanical actuation requiring an intermediate component introduces extra volume and complexity, problematic for a wearable device. SMAs, while not strictly electroactive, are conductive and can be brought to the desired temperature via Joule heating. In contrast to other shape memory technologies, they had been used in outside research on needle insertion [31], [59]. On this basis, the technology was reviewed in greater detail, and all subsequent discussion of the SME refers to the thermal transformation occurring in specific alloys.

In metals, the SME is a thermal phenomenon based upon transformation between two solid crystalline phases, occurring when grains of a material cross a temperature boundary. Differences in the dimensions of crystals of these phases result in a macroscopic change in the free dimensions of a part made from a material exhibiting SME, as its temperature changes near the boundary [60].

Transition to one of the phases (or either phase in the case of two-way “shape memory”) results in restoration of the shape previously “memorized” in that phase [60].

Among the best-known SMAs is the one used in recent versions of the e-Mosquito — the nickel-titanium alloy nitinol [60] (formally NiTiNOL, the “NOL” denoting its discovery by the US Naval Ordinance Laboratory). At room temperature, it assumes an anisometric geometry known as martensite (Fig. 5), consisting of unit cells in the shape of rhombic prisms. Cell edges defining the rhombus are longer than edges perpendicular to it, some 60% greater in the case of edges along the longest axis. Cells may be arranged in one of two ways — a twinned (monoclinic) structure naturally produced when the material enters the phase, or a detwinned (orthorhombic) structure produced when external forces cause the longest axes of neighbouring cells to become aligned. Above a threshold, grains of the material adopt a face-centred cubic structure known as austenite (or “parent phase”, as both martensite phases can be produced from it [61]). The edges of an austenitic cube are about 4% longer than the shortest edges of the martensitic prism, and thus much shorter than the longer edges [62].

Other phases of the material are possible under specific conditions [61].

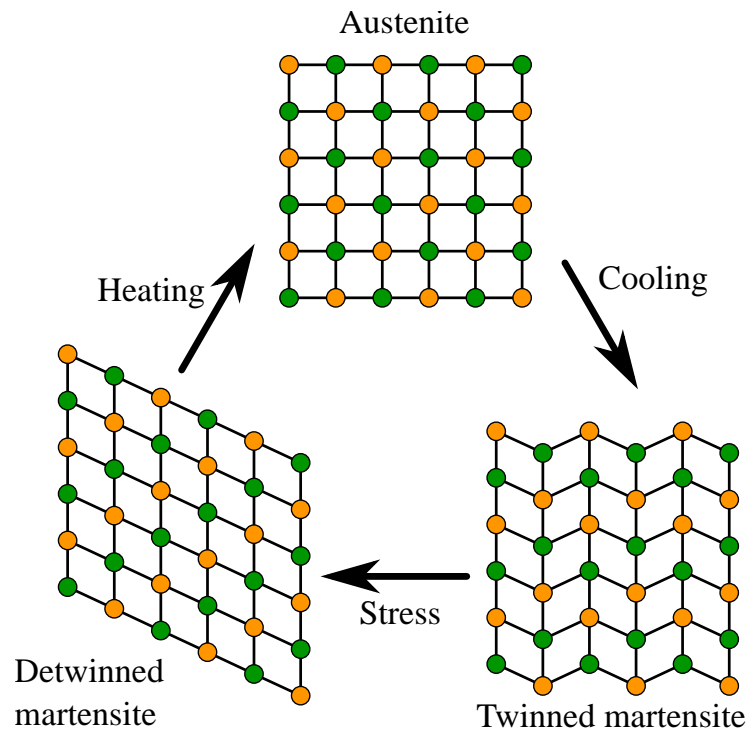


Figure 5: Illustration of the relationship between the nitinol phases of martensite (twinned and detwinned) and austenite. The phase structure also applies in the third dimension. This is not a precise representation of unit cell edge lengths or angles.

The actuation cycle (Fig. 6) consists of controlling the alloy temperature to maintain the desired fraction of grains in each phase. The threshold at which a grain transforms depends on the atoms within it and their arrangement. As the composition of an alloy varies locally due to unequal distribution of solutes and impurities, and grain structures begin to diverge through dislocations from the moment of crystallization, one can expect the thresholds of any two grains to be at least marginally different. Furthermore, the temperature of

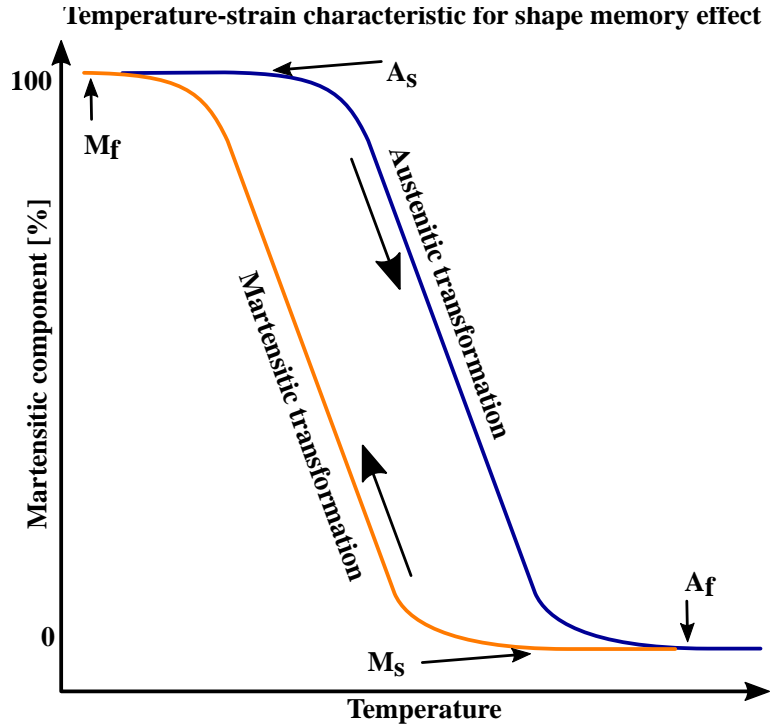


Figure 6: Sample hysteresis loop for the martensitic fraction of an SMA as a function of temperature. Labeled points indicate the beginnings and ends of transformation to the given phase: A_s — austenite start; A_f — Austenite finish; M_s : martensite start; M_f : martensite finish.

a material is an average from which different areas will deviate. It is therefore no surprise that the transformation of grains can only be predicted statistically, as a process occurring between a start temperature and a finish temperature. A nitinol part composed entirely of martensite will begin to transform to austenite at the “austenite start” temperature A_s , with the probability density of grain transformation increasing as the temperature rises and the austenitic fraction approaches 50%. The probability density falls as the material approaches the austenite finish temperature A_f , at which the part is composed entirely of austenite. The cooling process is similar, with transformation to martensite beginning at M_s and finishing at M_f . The cycle exhibits hysteresis:

$$M_s < A_f, M_f < A_s.$$

In aggregate, the changes in the dimensions of the grains undergoing phase transformations produce macroscopic changes in the free dimensions of an SMA component, and a restoring force that acts on any bodies that hinder the component from adopting these dimensions. In the case of

commercially available nitinol wire, the result is a contraction of up to 8%, assuming full transformation to austenite. A reduced transformation is desirable, as is a limit on the external strain applied while the material is contracted: contraction induces stress, due to both the changes of inter-atomic distances within the material and the reactive forces of external bodies on which the SMA exerts force. When the combined stress from these sources exceeds the yield strength of the SMA, it is partly relieved through permanent deformations such as slip, their rate of occurrence rapidly increasing with external strain and percent deformation. Unlike the non-stress-inducing deformations subject to SME, internal dislocations are permanent and manifest as fatigue, reducing the magnitude of future contractions. Where the rated lifetime of a nitinol wire may be hundreds of thousands or more cycles for mid-range contraction (4–5%), it may fall to mere hundreds for greater contractions (6–8%) [63], [64].

SMA contraction is a gradual process due to the distribution of grain transformation temperatures and the gradual nature of heating (making spring-loading a potentially attractive, but more complex, avenue for storing energy for rapid release). For DC SMA actuation in a wearable, the normally trivial relationship expressing dissipated power P as a function of current I , applied voltage V_{app} and resistance R_{SMA} ,

$$P = I^2 R_{SMA} = I * V_{app} = \frac{V_{app}^2}{R_{SMA}},$$

takes on greater importance due to the presence of constraints on all three components. The simplest involves V_{app} , which must be supplied by a compact power source; rechargeable Li-ion battery technology supplies a nominal voltage of 3.7 V.

Increasing

$$I = \frac{V_{app}}{R_{SMA}}$$

through a wire accelerates heating, but will also increase the stable value that the temperature of the wire will approach if the current is not subsequently reduced. In the absence of closed-loop feedback control of the wire temperature through current regulation or active cooling, the value of I must be fixed.

Finally, continuing to focus on the wire case,

$$R_{SMA} = \frac{\rho_{SMA} l_{wire}}{A_{wire}} = \frac{\rho_{SMA} l_{wire}}{\pi r_{wire}^2},$$

where ρ_{SMA} is the average resistivity (nominally fixed for a given SMA, though varying slightly with temperature and phase [61], [65]), A_{wire} is the cross-sectional area of the wire (related to the wire radius r_{wire}) and l_{wire} is the wire length. The spatial variables are all constrained by the mechanical aspects of SMA actuation. Greater A_{wire} increases

- the force produced for a given contraction [63], [64];
- the tensile strength [63], [64];
- stiffness (mechanical resistance of the wire to bending); and
- heating and especially cooling times [63], [64], due to skin effect for the former and the cross-sectional equivalent of the square-cube law for the latter.

The first two constraints enforce minimal diameters, the last two — maximal ones (given the benefits of being able to wind wire and actuate promptly). l_{wire} of course determines the absolute length of contraction,

$$\Delta l_{wire} = k * l_{wire}$$

where k is the relative contraction (e.g., 4%). Designs using SMA for actuators delivering substantial strokes have either increased wire length (whether by winding a single strand of wire [66], [67] or by combining multiple wire segments with multiple rigid parts [68]), used leverage at the expense of force [69], or both [70]. However, neither approach as described is practical given the volume restrictions of a wearable. Expressing R_{SMA} in terms of V_{app} and I and solving the resistance equation for wire length,

$$l_{wire} = \frac{V_{app}}{I} * \frac{A_{wire}}{\rho_{SMA}},$$

which yields the maximum length of wire available for a linear tension actuator with a voltage V_{app} applied across l_{wire} . The idealized quotient of area and resistivity does not consider the skin effect and is better replaced with the real-world, Ω/m equivalent — standard resistance, which manufacturers typically provide along with a recommended current I .

In practice, this meant that the existing e-Mosquito actuator, using a nitinol wire 150 μm in diameter with $A_s = 70$ $^\circ C$ (BMF-150, Toki Corporation, Tokyo, Japan, [64]), might supply a current of over

340 mA to obtain ~4% contraction of a free length of 158 mm , in 1–2 s, with relaxation slower due to cooling by free air convection (compared to flowing air or oil [71]). This set a maximum frequency of operation that the wire, if cycled constantly, might endure for days on end before its performance greatly degraded [64]. When used only a few times per day, the SMA lifetime stood to exceed the lifetime of any device within which it may be employed. Such was the hypothetical use case of the prototype — an array of single-use needle cells would be replaced daily. Each cell had a dedicated SMA wire, so contraction of each wire would also occur only daily. Products with other diameters were viable, ranging from 100 μm (BMF-100, Toki Corporation) to 250 μm (3-080, Dynalloy, Irvine, CA, USA [63]), and while these varied proportionally in their current and force capacities, 4% contraction could be employed for all of them without concern for phase transformation lifetime.

While SMAs are renowned for the high achievable ratio of work performed to volume occupied (power density) [71], the cost of carrying out this work is high. The most fundamental limitation on the efficiency of the SME in cyclic actuation (see Fig. 6) is defined by the corresponding Carnot cycle [71], with an efficiency

$$\eta_{Carnot} = 1 - \frac{T_L}{T_H}, = 1 - \frac{M_f \sigma_{yield}}{A_f \sigma_{recov}}$$

where T_L is the lowest temperature reached by the SMA (corresponding to the cold reservoir in the classic Carnot definition), T_H is the highest (corresponding to the hot reservoir), σ_{yield} is the yield stress and σ_{recov} is the recovery stress. η_{Carnot} grows with the difference between T_L and T_H , and in a non-entropic, ideal-gas system, this difference would be maximized. However, the cycle corresponding to the 4–5% length deformation reasonably available for an SMA actuator occurs between M_f and a temperature below A_f , and the ratio of σ_{yield} to σ_{recov} is limited to roughly two for nitinol. As a result, the Carnot efficiency for the simplest, most efficient SMA actuator configuration (unopposed tension [71]) has been calculated at 8.1% (values vary depending on methodology and assumed material parameters) [60]. Considering the losses due to physical factors — decreased transformation due to stress, heat losses from conduction and convection, etc. — the ideal efficiency of the configuration falls by more than half [60]. Ideal values vary from 2% [51] to 10% [71] and reported values are again lower, 1% or less depending on the actuator configuration

[60], [71]. This contrasts with efficiencies of at least 90% for traditional actuators delivering small (non-MEMS) force and displacement [71].

Though high, the power consumption was considered acceptable based on the low frequency and duration of sampling required for SMBG — in the extreme case, 12 actuations might consume

$$12 \times 340mA \times 10s = 11.3 mAh,$$

a modest fraction of the capacity of a typical Li-ion battery.

Based on all these considerations, it was concluded that SMAs remained a reasonable choice for blood sampling and that there was no superior alternative that might be readily integrated with the existing e-Mosquito design. Therefore, subsequent consideration focused on alternative designs using SMAs. Integration of a spring-loading mechanism with this technology to address the low insertion speed that might result from the low contraction velocity of nitinol remained feasible, but would complicate this maximally compact wearable system due to the need for multiple actuators (loading and release) per blood sampling cell, and require redesign of more of the e-Mosquito control system. Since direct nitinol propulsion had been proven sufficient during development of the existing e-Mosquito prototype, non-biasing springs were omitted in favour of minimal revisions.

Scope and requirements for redesign

The e-Mosquito cells displayed areas of possible improvement. The sliding rack and rotating lancet holder made the mechanical portion of the actuator relatively thick, and could not realize a large, yet decreasing, θ , as this would require the axis of rotation of the lancet holder to be located below the surface of the skin. As previously concluded, any replacement mechanism should rely upon the same actuation technology, and ideally only require modification of mechanical portions of the system — while revisions might be made to the actuator PCB and the mechanical parts, the circuitry on the upper boards would remain unchanged. Given the challenges involved in skin-penetrating actuation, any worthwhile alternative to the existing system should represent a genuine improvement.

On this basis, the following design requirements were identified [72]:

- The lancet needle must be able to puncture the skin and break capillary vessels; it must therefore extend at least 1 mm [73] into the skin.
- The parts of the e-Mosquito that contact the skin near the insertion point (i.e., the lancet, glucose test strip and nearby casing) should be easily replaceable, so that they can be made disposable and the main device reused multiple times without intensive sterilization.
- Parts conducting electrical or thermal current, particularly the (electrically heated) SMA wire, should be isolated from the skin to avoid causing discomfort to the patient and coagulation of the extracted blood sample.
- The thickness of the assembled mechanical section, including all moving and replaceable parts, should be at most 4 mm.
- Finally, for timely development rather than product effectiveness, it should be possible to produce actuator cells using rapid prototyping technologies, and to build a cell using at most three custom-designed parts produced with these technologies.

These requirements matched or exceeded the standards identified in the design of or implied by the implementation of the existing e-Mosquito MEMS [24].

Chapter 2: Materials and methods

In this chapter, we review the process of reducing the system's physical dimensions and the materials required for an e-Mosquito cell. Computer-aided design (CAD) and computer-aided manufacturing (CAM) enabled production of a large number of designs using basic rapid-prototyping equipment. Initially, a 3-D printer (Replicator 2 from MakerBot, New York, NY, USA) was available. This was later supplemented by a Computer Numerical Control (CNC) milling machine (Nomad 883 Pro from Carbide 3D, Torance, CA, USA).

Software

For both prototyping machines, a multi-program workflow was required to turn a concept into a physical part:

1. CAD involved a parametric modeling system. Popular software from several sources was considered, listed in Table 1, with SolidWorks ultimately selected due to its compatibility with existing e-Mosquito project files, prior use by the lab and easy simulation of irregular assembly mechanics.
2. The resulting design was exported to a CAM system. By default in both cases, this was software provided by the machine vendor, which accepted .stl (stereolithographic) files. Printing instructions were prepared with MakerBot Desktop (MakerBot). Milling instructions were initially prepared with MeshCAM (GRZ Software, associated with Carbide 3D), and later with the HSMXpress plugin for SolidWorks (Autodesk), which offered finer control and feature-based milling. Each system produced machine-specific G-code that would execute a set of movements within the machine's work coordinate system (WCS).
3. The G-code was delivered to a driver. With the printer, this could be achieved by allowing MakerBot Desktop to communicate with the Replicator 2X controller via a serial connection, or by producing a printer-specific .x3g file and transferring it via a Secure Digital (SD) memory card. The mill required serial communication between the proprietary Carbide Motion (Carbide 3D) PC-side software and the Nomad 883 driver.
4. The machine produced the part, which may require manual post-processing such as smoothing or cutting prior to assembly and testing.

Table 1: Considered 3D modeling software.

Name	Source	Conclusion
FreeCAD	Open source	Capable of part design, but unable to handle assemblies
Autodesk Inventor	Autodesk, Inc., San Rafael, CA, USA	Capable of assembly, but encountered difficulties in simulating cam motion.
Fusion 360		Full assembly and simulation capability.
SolidWorks	Dassault Systèmes, Vélizy-Villacoublay, France	Full assembly and simulation capability.

3D printing

The 3D printer (Fig. 7) implemented additive manufacturing via fused deposition modeling (FDM): a 1.75-mm-thick polymer filament, by default, would be extruded through one of two heated, 0.4-mm nozzles, producing a viscous thread that would quickly harden in a controlled position atop a heated print build plate. DC stepper motors precisely controlled x - and y -axis positioning of the nozzles via a gantry system, and z -axis positioning through elevation of the plate (movements expressed in terms of the internal WCS).

Available filaments (all from MakerBot) included:

- black acrylonitrile butadiene styrene (ABS),
- various colours of poly(lactic acid) (PLA, formally a polyester) and
- white “dissolvable filament” (high-impact polystyrene, HIPS).

ABS and PLA were typical filaments for part production, while HIPS was intended as an easily removable support material. Due to the natural presence of lactic acid in the human body PLA is considered biocompatible (though not without effects such as local acidification and minor

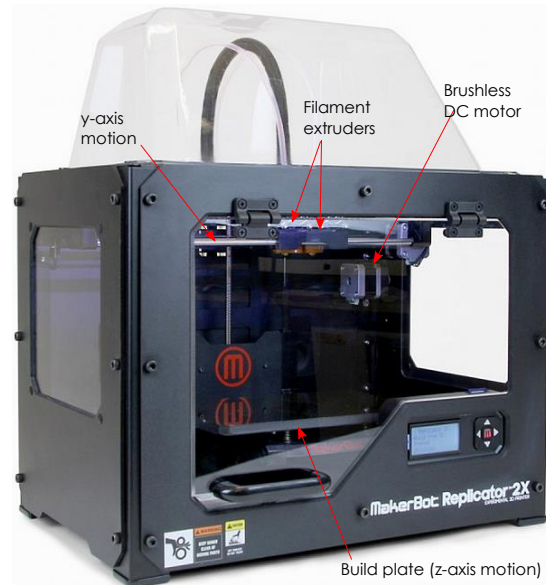


Figure 7: Relevant features of the "Replicator 2X" 3-D printer used for prototyping.

inflammation when implanted long-term [74]). By contrast, the components of ABS (acrylonitrile, butadiene and styrene) are toxic ([75]–[77]) — considered safe for skin contact, but worrisome in the event of entry into the body. ABS is used in external wearables, but less than ideal as a material against which the tip of a needle scrapes immediately before entering the skin: a minute quantity (perhaps micrograms) of the channel material may be removed from the part and deposited in the body, with unforeseen effects when this motion is repeated thousands of times through regular use.

However, PLA filament also has a lower melting point than ABS [78]. Prints produced with it were softer before cooling and subject to warping upon removal from the heated build plate. This made PLA less suitable for precise parts. It proved more practical to use ABS in most cases and save such concerns for possible future manufacture, which might involve more repeatable technologies such as moulding. Even using ABS, accuracy was a concern.

While the motors positioned the nozzles with accuracy below 0.1 mm, the reliable resolution of parts produced with the printer was limited by the mechanics of molten plastic, which exhibits variable degrees of viscosity and tension. The FDM process was highly sensitive to:

- the temperature of the extruder, nozzle and plate, controlled by a combination of two heaters and a cooling fan;
- the path and speed of the nozzle relative to the build plate, affecting the cooling of and forces acting upon the molten plastic; and
- part geometry and orientation, with feature quality affected by the available spatial positioning resolutions in different dimensions and by the need to support newly-extruded filament against gravity.

These diverse factors limited resolution — though the printer could produce filament layers as thin as 0.1 mm, it could not reliably form features below 1 mm in the *X* and *Y* (horizontal) dimensions. Small prints may fail to adhere, and small gaps may be narrowed by deformation and the “stringing” of material dragged from the nozzle even when nothing was extruded. However, the printer only used the amount of fibre needed to produce the part and any supporting components, and needed little time to produce a small part which might otherwise require machining from several directions. A centimetre-scale part required minutes to manufacture. Features of 0.8 mm could be produced through trial and error.

Reliability

Regardless of scale, a print would fail if it did not adhere to the plate until complete. Plate adhesion depended on:

- build surface material, texture and temperature;
- filament material and temperature at the moment of contact with plate;
- height, rate and temperature at which filament was extruded above the plate;
- speed and acceleration of the extruder relative to the plate; and
- ambient vibrations and air flow.

The build plate was reasonably smooth and covered with kapton tape (MakerBot) for improved adhesion [78]. This was not always sufficient: a thin strand of material tended to slide over the build surface, creating a tangle of melted plastic around the extruder nozzle instead of a fixed layer pattern, potentially leading to clogging. This could also occur when printing too close to the plate (no space for extruded material to escape the nozzle) or too far (no adhesion before hardening).

The manufacturer recommendation was to print rafts — multi-layer assemblies beneath the main part with wide first layers [78]. However, direct printing on the plate was desirable due to the resulting smoothness of the contacting surface of the printed part. Smoothness could reduce friction for a moving part, or increase the comfort of a skin-contacting surface.

Contact surface area between the first strand of plastic and the plate could be increased in two ways, related to the two dimensions of the first segments contacting the plate:

- The long test segments extruded at the beginnings of print sequences generated by MakerBot Desktop (to verify that filament was in position for printing) could serve as “anchors”. By themselves, these adhered weakly.
- Thicker, wider segments could be produced by controlling the relative extrusion speed, travel speed, and nozzle height. A larger amount of material deposited along a given length would spread more, due to gravity and the pressure of further filament being forced through the nozzle (excessive pressure would cause this material to back up and clog).

Travel speed and nozzle (layer) height could be controlled programmatically, but direct extrusion speed could not — for printing of the main part (rather than the raft), MakerBot Desktop targeted

an effective extrusion diameter similar to the nozzle diameter, adapting the extrusion speed to match the travel speed. Increasing the layer height was the main tool available to increase width, at the cost of *Z* resolution.

The Raft feature did include detailed width control for the base, interface, and surface layers of the raft, along with a variety of other parameters. No control over the raft pattern was available, but it was possible to:

- reduce the margins by which the raft extended beyond the printed part,
- set the bottom layer printing density to 99% and the gaps between adjacent strands to 0 (this did not result in a solid layer in practice, but came close),
- eliminate the higher raft layers,
- remove the “gap” setting normally used to print the first layer of a part further above the raft and thus have the bottom part layer adhere weakly to the top raft layer) and
- print the raft from the same material as the part.

In short, it was possible to incorporate the raft into the part being printed on it. The result was suitable for larger (multi-centimetre) parts. However, incorporating the raft was not effective for parts which:

- were too small to require a substantial length of strand in the bottom layer of the raft,
- had overhangs (these required support material, which would be trapped between the part and the raft and thus be impossible to remove) or
- had small openings.

Fine features

While the printer could deposited on the plate a strand both thicker (*Z* dimension) and wider (*X* and *Y*) than its nozzle, it could not reliably extrude threads much thinner than the nozzle diameter. With greater flattening and limited extrusion, layer heights of 0.2 mm or less were possible, but in the *X* and *Y* dimensions, the minimum thread width was close to the nozzle diameter. 0.4 mm represented the narrowest printable wall. The inverse of the minimum wall thickness is the minimum hole diameter or the minimum gap that can be reliably left free of plastic while surrounded by printed plastic on two or all sides. Ideally, it should be limited only by the flow of solidifying filament and the (fine) resolution of the positioning motors in the printer.

In practice, both parameters can be degraded by the software used to plan the printing toolpath (the slicer). Some slicers will only print a wall with at least two parallel layers of filament. Quickly printing the perimeter of a hole, or only pausing extrusion while traversing across a narrow gap, causes the filament to be dragged from the nozzle by tension and “strung” across the space.

MakerBot Desktop lacked algorithms to compensate for the real-world limitations responsible for bridging, as well as options for finer manual control of how it sliced files. Customizable slicing profiles in the program offered reasonable control over movement, extrusion and fan speeds; extruder and plate temperatures; layer heights and infill; and auxiliary structures such as purge walls, rafts and supports. They allowed the user little control over the way in which primary structures were generated (sliced).

A variety of freely available slicers offered levels of control ranging from total automation resembling MakerBot Desktop to line-by-line control of G-code only a level of abstraction above writing this code manually. Features included:

- “lift” or “hop”, which elevate the extruder a set distance relative to the build plate (in the case of the Replicator 2X, by lowering the plate) before executing a travel (non-extruding) move;
- per-layer printing parameters (including but not limited to temperature and filament feedrate);
- methods of improving plate adhesion, such as increasing first-layer width or printing a “skirt” — a detachable spiral of filament around the outside of the first, most fragile layer of a part (as opposed to a raft beneath it); and
- easy insertion of custom G-code routines.

Four hurdles stood in the way of using a different slicer. The Replicator 2X:

- differed in standard parameters, like every 3D printer;
- had two extruders and a heated build plate, requiring extra complexity in any slicer that would take advantage of these features;
- had a distinct flavour of G-code, with some commands from other flavours ignored or used differently; and
- required either real-time serial commands or compressed .x3g files on an SD card.

While the first hurdle is common to all printers, and is resolved by custom profiles, some programs (e.g. Cura [79]) lacked default profiles for the Replicator 2X or anything similar. Precise manual determination of parameters was rarely practical.

Support for dual extrusion and build plate heating was variable. Certain printing programs originated as single-extruder systems and viewed the second extruder as an addition whose detailed settings were an afterthought.

The most important obstacles involved G-code flavour and delivery format. Two programs, compared with MakerBot Desktop in Table 2, appeared promising in their ability to slice a file, generate G-code of a similar flavour, and produce .x3g.

Table 2: Summary of evaluated slicing software for 3D printing.

Program and source	Slicing engine	Profile / flavour	X3G generation
MakerBot Desktop, MakerBot [80]	MakerBot	MakerBot	Native
MatterControl, MatterHackers Inc. [81]	MatterSlice (only 2-extruder option)	RepRap	GPX
	Slic3r	“MakerBot”	GPX
ReplicatorG, open source [82]	Skeinforge	Replicator 2X	Native

The “MakerBot” flavour was designed specifically for compatibility with MakerBot products, RepRap was the open-source flavour from which the ultimately proprietary MakerBot flavour developed [83] and ReplicatorG was once the print driver for MakerBot products [83]. GPX is a command-line post processor for converting G Code to .x3g [84]; while it could potentially be used with the output of other programs, the effort was abandoned due to difficulties encountered with even these most closely related flavours: MatterControl was prone to incorrect operation of the Replicator 2X heaters, while ReplicatorG depended on old drivers and libraries and could not produce an X3G file for even a mildly complex toolpath.

The growing need for precision and reliability ultimately led to the replacement of the printer with a simpler subtractive technology for production of precise parts.

CNC milling

The Nomad 883 CNC mill (Fig. 8) represented subtractive manufacturing. It had three translational axes, allowing positioning of a rotating cutter at any Cartesian (X, Y, Z) coordinate in the work space, but not allowing any rotation. It was thus incapable of producing any feature that could not be cut out from above. The range of available geometries was thus limited compared to additive manufacturing, and any part that would require supports in a 3D printer would require careful manual reorientation of the stock in the mill.

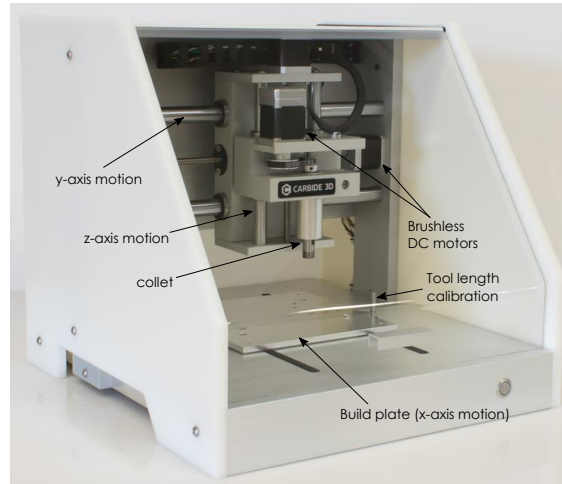


Figure 8: Key features of the Nomad 883 Pro CNC mill used in prototyping.

On the other hand, the mill possessed far greater precision:

- Mechanical resolution (of the positioning DC motors) was listed as .0005 in (.013 mm).
- Nominal mechanical repeatability was listed as .0015 in (.039 mm) [85].

The latter was an order of magnitude below the finest feature sizes required for the parts (0.4 mm) produced throughout the research, which were determined by the need to interface with and move the lancet needle. The lower limits on feature size achievable with the CNC mill were related to:

- the diameter of the cutting bit,
- the deformation of the stock material in contact with the cutting bit and
- the precision of positioning of the stock material (where multiple manufacturing steps required alignment of the new features with existing ones).

End mills (or “cutters”) with nominal cutting diameters as small as 1/64 in (0.4 mm) were reasonably available. Square end mills were preferred due to their ability to produce openings with flat floors, but a variety (Table 3) were used throughout later prototyping.

Table 3: List of end mills used with the CNC mill. The standard alloy for milling bits is tungsten carbide.

Tool #	Diameter		Type	Vendor	Product ID	Notes
	in.	mm.				
20	1/4	6.35	Square	Nomad Tools	201	3-flute; others are 2-flute
30	1/8	3.18	Square	Nomad Tools	102	
31	1/8	3.18	Ballnose	Nomad Tools	101	
40	1/16	1.59	Square	Nomad Tools	112	
50	1/32	0.794	Square	DGI Supply	15997	1/8 in. (3.2 mm) LOC
51	1/32	0.794	Ballnose	Nomad Tools	121	1/16 in. (1.6 mm) LOC
60	1/64	0.397	Square	DGI Supply	15995	1/32 in. (0.8 mm) LOC
83	0.004	“0.1”	Engraving	CNBTR	Q2E3	0.1–0.2 mm LOC; for PCBs

The mill was also capable of shaping a wider range of materials (stiff polymers, soft metals and composites of similar strength). Cutting stock used included:

- common printable polymers like ABS, whether printed or purchased in sheets;
- sheets and blocks of transparent plastics such as poly(methyl methacrylate) (PMMA) and poly(carbonate);
- sheets of soft metal, particularly 6061 aluminum; and
- composites, specifically double-sided copper-clad boards. (Fig. 9)

A far greater amount of cutting material was required, since everything surrounding a part must be removed and parts could not be produced in the very corner of the material. The process placed high stress on cutters. The thinner a cutter, the more fragile it was, and the more likely it was to break if faced with excess deflection. Deflection of the cutter was related to the force of resistance of the stock, which depended on factors such as:

- stock hardness, elasticity and friction;
- cutter depth and rate of advancement relative to the stock (feedrate);
- cutter runout (undesired side-to-side movement increasing the volume of material that was removed);

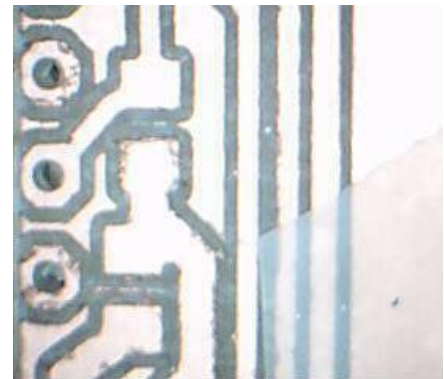


Figure 9: Features on a PCB milled with the Nomad 883. From left to right: three isolated holes; four pads for two surface-mounted resistors; three parallel traces and a ground fill. The narrowest cuts (dark) are 0.4 mm wide. Transparent tape (lower right) was used as a simple soldermask.

- accumulation of stock material on the cutter (due to melting of the stock, a problem for plastics with lower melting points such as PLA, but not for, e.g., ABS).

The primary means of preserving the cutters involved selection of appropriate size, feedrate, cutting depth and rate of rotation, and regular monitoring of the milling process.

While more expensive in terms of supplies, the mill exhibited unrivaled precision. A sample sliding rack cut from PMMA was examined under a backlit microscope (Eclipse TS200 from Nikon, Tokyo, Japan) and viewed with Q Capture Pro 7 imaging software (QImaging, Surrey, Canada). The part was designed to fit in a mold and leave a gap of 25 μm . The actual gap was measured as being 93 pixels in the software. Since 623 pixels corresponded to approximately 0.46 mm as determined by placing calipers in the field of view of the microscope, 93 pixels corresponded to approximately 68 μm . The gap was thus found to have increased by 43 μm , consistent with the nominal tolerance of 50 μm provided by the manufacturer of the CNC mill. The printer was capable of sub-millimetre features but might produce them with a tolerance of up to 0.5 mm for easily deformable materials or inadequate workholding (it was 10 times more precise given optimal conditions). It was used both for fine corrections and additions to printed parts, and as a standalone prototyping machine.

Positioning and workholding

While the Nomad 883 was very precise in positioning the cutter within its internal WCS, it had no direct information on the location of the stock. Great care was required to ensure that the implemented toolpath encountered the desired points in the stock.

A key challenge lay in fixing the stock on the 8x8 in. (20.3x20.3 cm) build plate. The plate possessed threaded holes which could be used to mount a variety of attachments, including:

- a milling vise,
- a wasteboard or
- independent screws (to serve as improvised clamps).

The milling vise allowed firm gripping of stock that was rigid enough to not deform under the pressure of the jaws and large enough that the jaws would not interfere with milling. Parts with any dimension on a millimetre scale were prone to deformation if this dimension was arranged parallel to the contacting planes of the vice jaws, or inadequate space for milling if perpendicular. Attempts

were made to use the vise for thin parts by printing ABS blocks that could provide a supportive under-layer for a part laid in the bottom of the vise. It proved impossible to ensure that the part in question would deform against the blocks (by positioning it slightly bent, with a small initial deformation in that direction) rather than upwards. The vise jaws also posed an excessive hazard for the cutting bits that needed to enter the vise space — the Carbide Motion driver software tended to bring the cutter to the origin (usually a point on the part, deep within the vise space), by the most direct path possible, often colliding with the vise.

A purpose-made wasteboard, attached to the plate, provided a surface that the cutter could approach with relative safety. It was an obvious choice for thin, flat-bottomed stock, which could be attached adhesively (e.g. with two-sided carpet tape — 3M, Maplewood, MN, USA) provided that there was a large contact surface. Wasteboards could also be used for relatively precise alignment of multiple orientations of a flat part: stock could be attached to the board with nails, milled, then flipped and nailed down again using the same nail openings in the board.

Improvised clamps were appropriate for a narrow class of parts that:

- were too thin for the vise,
- had too little surface area for adhesion to a wasteboard,
- had been partly produced with 3D printing,
- yet required precision features on the top surface.

For an example, see Chapter 4, “Multi-track design”. A rectangular prism was first printed atop a larger layer (the raft layer from the perspective of the MakerBot Desktop software) from which it could be removed given sufficient force. Clamping of the layer to the plate was achieved by either

- preparing holes in the bottom of the plate with diameters and spacing corresponding to that of holes in the build plate and clamping directly with the screws, or
- positioning the ends of the layer underneath a rectangular PMMA frame that was in turn pressed down by the screws.

The former method constrained the position of the part and was prone to motion of the part due to deformation of the layer. The latter did not ensure angular alignment of the part with the mill’s coordinate system and was prone to motion due to the weak grip provided by the PMMA layer

(which tended to deform under the pressure of the screws instead of delivering the same pressure to the layer beneath it).

Each time the stock was moved, a new coordinate system offset had to be manually defined using the Jog mode of the Carbide Motion interface software, so that the physical cutter location corresponding to the digital origin would match the location on the stock selected during planning of the toolpath. The spindle would be moved until the tip of the cutter barely touched the stock from a given direction. This would then be set as the zero point for a given axes (e.g., if the cutter touched from above, the internal Z coordinate for the current position would be set to 0). For X and Y, unless cutting parts from larger stock that had no pre-existing features to align with, cutter radius also had to be taken into account.

While a great deal of work was required to operate the mill, far less maintenance was required due to the absence of molten filament.

Toolpath planning

In the case of CNC milling, the workflow discussed in “Software” was briefly reduced to steps 2–4 when G-code routines for the CNC mill were written manually. This overcame several limitations of MeshCAM:

1. It was not possible to use cutters of a selected size only for selected features — the finest control involved rectangle-based selection of two-dimensional cutting areas. Within the selected area, all possible surfaces would be machined with all selected cutters (e.g. “roughing” and “finishing”).
2. The software tended to complicate routes due to its global adherence to user-provided parameters that were only necessary for key local features. The precision features (track and channels) required only a few simple, linear movements.
3. Unknown criteria were used to determine whether to mill certain features, and the software was tedious to use for drilling of certain openings needed for workholding and alignment.
4. It was difficult to coordinate multiple CNC routines for the different sides, resulting in repeated breakage of fine cutters that had to be replaced through specialized suppliers.

It proved possible to manually code all basic features, especially by reusing snippets of relative-coordinate code (the absolute coordinate instructions generated by MeshCAM were converted

using a custom program – Fig. 10, code in Appendix B: “Code of absolute-relative G-code converter”). Direct modification of key values allowed for changes to be made far faster than with the usual process of modifying a 3D model and converting it into a CNC routine.

This process was long and difficult to document, but was initially worthwhile compared to producing the entire part using MeshCAM’s toolpaths. G-code operations could be planned one-by-one and either executed individually using Carbide Motion’s Manual Data Input (MDI) mode, or written in .nc files for automated execution.

The manual approach was shortly supplanted by HSMXpress, as the latter allowed feature selection and extensive parameter control.

External production

Due to the challenges of producing parts with fine features, outside manufacturing was repeatedly considered. Sub-millimetre features are beyond the resolution of a typical machine shop, yet a number of companies offer rapid prototyping services, primarily involving 3D printers and CNC milling. It was found that many of the former were unable to produce the parts in question more precisely than the machines in the laboratory, due to the fundamental resolution limitations of FDM. Similar limits apply to other additive technologies: all processes involving non-uniform heating (whether of plastic filament, powder particles or hardening resin) are subject to thermal warping, tensions and the effects of gravity. Small-run prototyping was generally automated and handled without attention to the particulars of a part.

The variety of failed prints and abandoned inquiries is not discussed. An exception is made for a thin, flat part (62x35x3 mm) produced by an external company with “ultra-high precision resin” (Fig. 11). The key openings and sliding contacts (see the base in Chapter 4, “Multi-track design”) might have been printed correctly, had the product been oriented horizontally, instead of at the

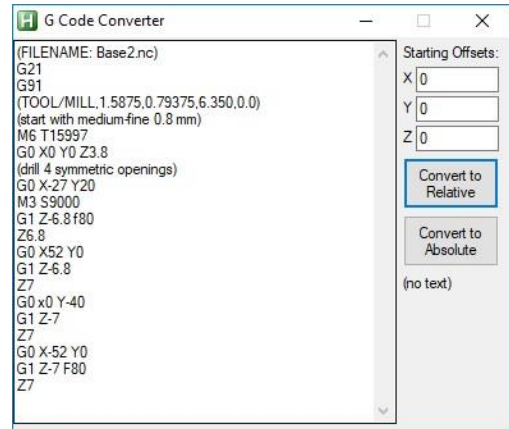


Figure 10: Screenshot of the custom G-code conversion application, showing the first 20 lines from Appendix C, “Two-sided base piece”, converted to relative coordinates.

entertaining, space-saving angle shown. This was the highest-resolution widely available additive technology, alongside polyjet printing. No companies using the two were able to guarantee sub-millimetre features.

One would expect CNC milling operators to offer higher resolution; fewer of these were available. One company required that all walls, including floors and overhangs, be increased in thickness to 1 mm. This was due less to absolute limits of the company's 5-axis CNC than to the fact that quick manufacturing turnaround times were achieved by running the machine largely unmonitored. Fine feature sizes tend to require small cutting bits that are especially prone to breaking. Other contacts were similarly unproductive:

prototyping companies cited prices upwards of 60 CAD for the most difficult part (the aforementioned base). Said part would ultimately be milled in under 20 minutes using a (tedious to plot but simple to execute) manual G-code routine.

A variety of other potentially high-resolution techniques were not thoroughly investigated, as they required specialized, less-available equipment that entailed higher costs and turnaround time:

- Micro-moulding involves injection of molten material into a precisely shaped enclosure.
- Hot embossing involves pressing two heated metal surfaces with inverses of the desired geometries against plastic stock, which promptly reflows to mould into the desired shape (rather than being injected into a closed mould).
- Laser cutting selectively vaporizes small quantities of material.
- MEMS techniques such as photolithography are appropriate for features slightly finer than needed here.



Figure 11: A base part printed with a “high-precision” resin, but not flat on the build plate as intended.

Chapter 3: Initial translating-rotating designs

Early concepts

It was first suggested to use needles with crossbars melded onto them in a T shape (Fig. 12), perhaps with wheels on the ends of a crossbar allowing it to ride along tracks in the surrounding material. The needles adopted for prototyping (as in the proven e-Mosquito actuator: 28-gauge OneTouch Ultrasoft Lancets from LifeScan Inc., Milpitas, CA, USA) were approximately 0.45 mm in diameter and could be cut up to several centimeters long; features of similar scale would be required to interface with one and control its motion.

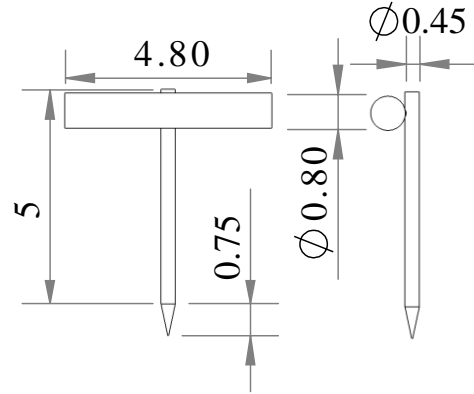


Figure 12: Sample dimensions of a 30-gauge needle welded to a wire crossbar.

I set out to iteratively redesign the proven actuator. In the interest of design for manufacturability (DFM), I sought a minimal design encompassing only critical components; these included a disposable casing, needle, chemical test strip, and a part to isolate the needle thermally and electrically from the SMA wire. The idea of wheels was quickly dropped in favour of having the crossbar in direct sliding contact with the tracks, as the wheels would increase complexity and add undesired degrees of freedom (DOF) without commensurate reduction in friction.

The crossbar could serve as the axis of rotation and no other lancet holder would be required. The main challenge relative to the prior design would be to enforce both rotation and translation of the crossbar. The original sliding rack (Fig. 13) was redesigned to enforce two-way translation of the crossbar while leaving open the possibility of rotation (Fig. 14). Any component serving in this role is hereafter referred to as a “slider”.

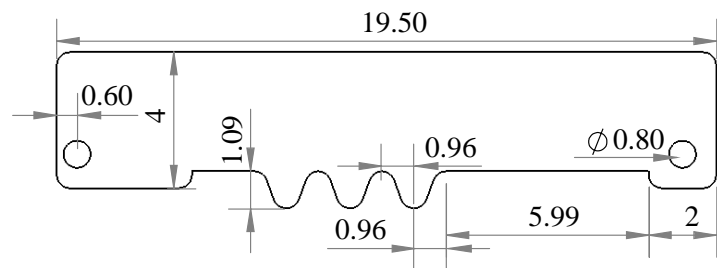


Figure 13: Dimensions of the sliding rack in the prior e-Mosquito actuator (1.75 mm thick).

Rotation would be enforced by features of the surrounding fixed layer adjacent to the skin (the “base”) that would vary depending on the degree of translation of the crossbar. Barriers blocking passage of a part of the needle-crossbar unit would cause that part to remain stationary while other parts of the unit advanced, resulting in overall rotation.

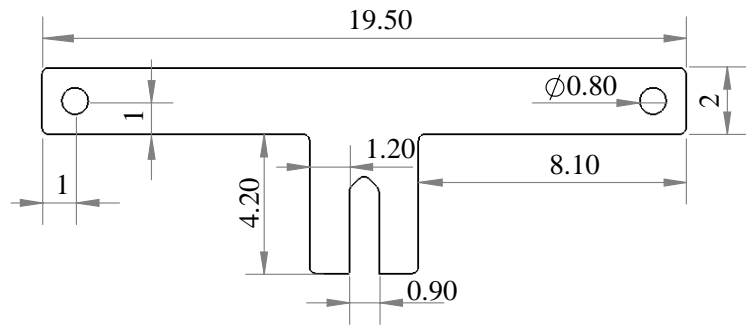


Figure 14: Sample dimensions of an early slider for driving the crossbar of Fig. 12. Compare Fig. 13.

A fundamental example of such features, used throughout subsequent designs, is provided in Fig. 15. The needle would rest in a downwards-sloping channel, the floor of the channel defined by a ramp and the ceiling by an overhang. Forward movement of the needle would cause the top side to press against the overhang and be redirected downwards, reducing θ . Thus angled, the needle would advance incrementally further horizontally and be redirected further downwards. The ramp worked analogously, forcing the needle to adopt a smaller θ when translated in the opposite direction. This ensured full withdrawal of the needle from the skin.

An early concept for integration of rotation-enforcing features with the track concept is given in Fig. 16. In this design, it was assumed that the skin would enforce downwards rotation once the needle tip entered it and that the overhang would primarily serve to prevent the needle from rotating too far upwards and thus failing to enter. More apparent in the figure are the challenges associated with the crossbar-and-track approach.

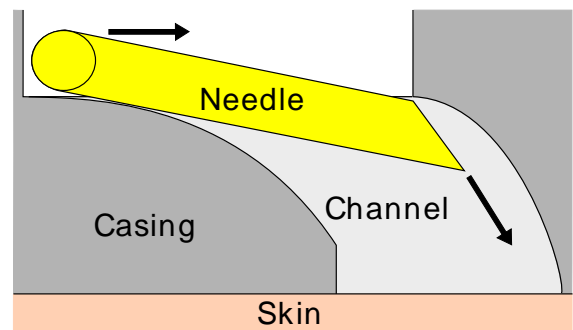


Figure 15: Basic concept of guiding a needle into skin using a channel whose geometry alters the angle of the needle relative to the skin as the needle advances. [72] ©2016 IEEE.

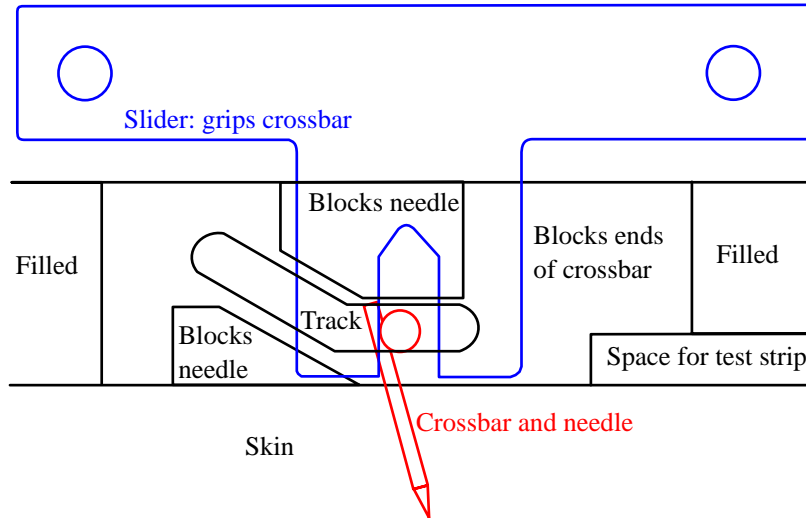


Figure 16: Multi-cross-sectional side view of an early concept for a means of enforcing translation and rotation of the needle-crossbar. The needle and crossbar (Fig. 12) are red, the slider (Fig. 14) is blue and the base is black. Sections of the base are labeled based on which coloured components may overlap with them in this projection.

If produced flat like the original, the slider could not be centred over the axis of symmetry of the combined needle-crossbar: the prongs interfacing with the crossbar would collide with the needle. To deliver force symmetrically, pairs of such prongs would be needed on either side of the needle, which would make the slider bulky and potentially difficult to prototype. Additional width in the base was required to accommodate tracks deep enough to prevent the ends of the crossbar from escaping. Available rapid prototyping technologies were unlikely to produce precise tracks in the vertical walls of an opening.

In addition, the crossbar was likely to substantially increase the unit cost of a disposable product. The small diameter of a needle would require spot welding for a secure connection. A local jeweller quoted an effective cost of C\$8 per needle, reflective of the difficulty of joining two wires of small diameter with laser welding. While the unit cost of high-volume welding might prove lower, the complexity involved would increase the production costs of a single-use component.

It was noted that half of a crossbar could be obtained by bending the lancet shank at a right angle, replacing the T of Fig. 12 with the L of Fig. 17. This eccentric approach greatly simplified part design:

- Lancets could be customized in less time and with more control over dimensions.
- There would be no concern about the quality of the welding joint.
- Attempts at symmetry could be abandoned, and the slider of Fig. 14 could thus be produced flat.
- The channel could be combined with the track, the result resembling Fig. 15 (the circle in the figure corresponds to the shank). The side walls of this single opening would prevent sideways translation of the lancet shaft.

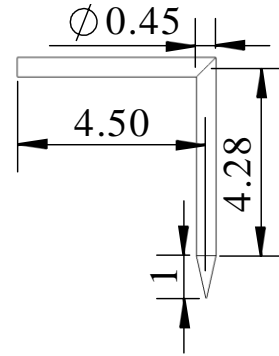


Figure 17: Sample schematic of L-shaped needle. All dimensions are in millimetres, 0.45 mm corresponding to the approximate outer diameter of a 28-gauge lancet. Arm lengths varied with other design parameters.

The simplicity resulting from this and from restriction of translation and rotation of the crossbar to the same horizontal plane allowed the prongs to retreat into the top part, reducing the slider height and leaving only a notch to hold the needle shank (Fig. 18). A lip extended from the roof of the notch to strengthen the part and to reduce sideways “roll” (rotation around the axis of translation) of the bent shank as it encountered resistance from the skin. Rotational concerns resulting from eccentricity would require increased precision and a variety of DFM measures throughout the development process.

The lower edge of the slider rested in a track in the floor of the base piece (key section in Fig. 19), trapping the lancet shank between the lip of the slider and the raised layer of material between the channel and the track. This reduced the DOF of the lancet. The track limited the range of translation of the slider while leaving the holes in the slider exposed so that wires or springs could pass through them.

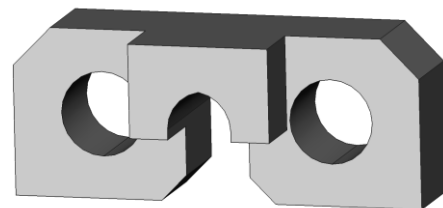


Figure 18: Slider design used in first working prototype.

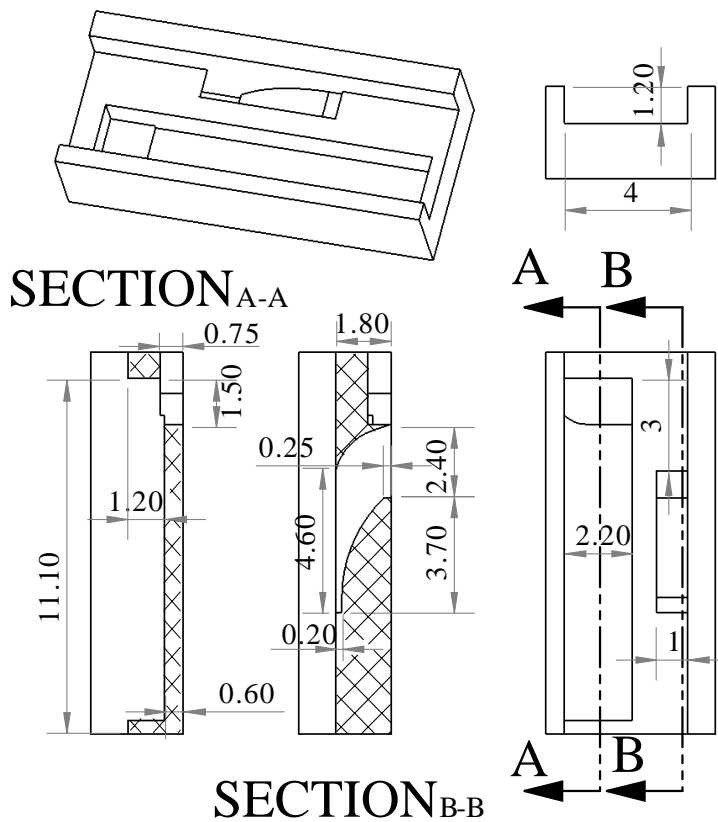


Figure 19: Key dimensions of the first physical implementation of the base.

The assembly of Fig. 17–19 (shown assembled in Fig. 20) was the first to be physically implemented: parts were printed and fit together, with minimal post-processing required to clear support material from the base channel. Operated manually, the centimetre-long assembly demonstrated that the channel concept was feasible in terms of producing translation and rotation of the needle in response to translation of the slider.

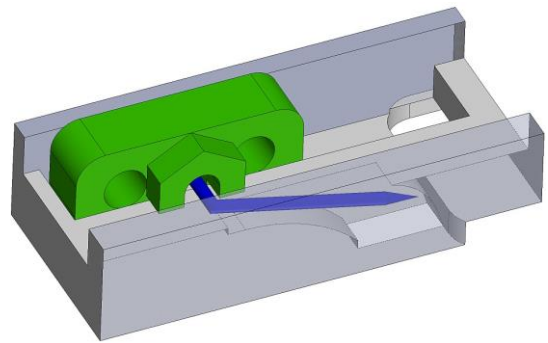


Figure 20: Model assembly of the first physical implementation of the base.

The main observed flaw was the interference of the test-strip space in the bottom of the base with the forward end of the track. The minimum depth of the

track was determined by the desire to prevent the driven part of the lancet from escaping from the notch in the centre of the slider. Since the narrow end of the test strip needed to border the end of the channel to have a chance of capturing blood from the skin, and since the longitudinal axis of the test strip should be parallel to the translational axis of the actuator to avoid greatly increasing cell area, the default way to prevent the interference would be to raise the floor of the track, and thus the floor of the base. This would increase actuator thickness, along with the length of the penetrating arm of the lancet that would never emerge from the base. Maintaining large θ and the same insertion depth would then require a longer lancet and ultimately a greater translation of the slider, problematic due to the displacement limitations of SMA actuation.

The interference was instead resolved by applying DFM to produce a thinner slider (Fig. 21) that bore little resemblance to the original rack (Fig. 14). The wire holes were rotated 90°, into the XY plane parallel to the base. The resulting shape could be printed on its “top” surface with no overhangs. The depth of the notch and the thickness of the material normally above it could thus depend on the finer resolution available in Z. While this reduced the minimum printable thickness of the slider to 0.4 mm, 1.6 mm was initially used, to comfortably accommodate the diameter of the lancet in the notch and to maintain a firm connection between the two ends of the slider.

Orienting wire holes perpendicular to the base introduced concerns about the routing of the SMA wire. As shown in Fig. 2, the wires never crossed in the original design — crossing would increase the chance of a short circuit leading to loss of current (and thus part of the heating and contraction) in one segment and greater current (and wear) in the remainder. Additionally, as the wire must be kept taut, any segment of it not perpendicular to the XY plane (such as the segment passing through a rotated hole in the slider) would be subject to torsion. To prevent the slider from being twisted, any torsion must be negated. This was done by doubling the holes, so that there were now two at each end of the slider (Fig. 21). Wire would enter one hole through the bottom of the slider (first

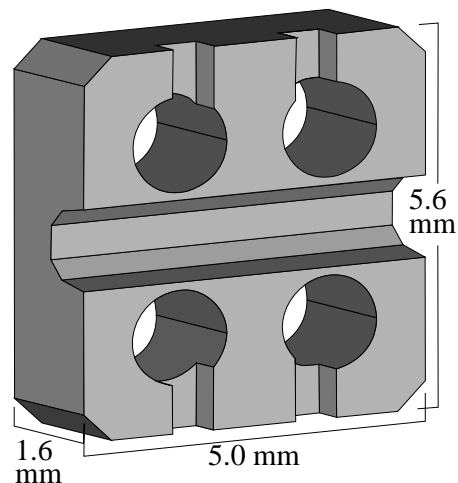


Figure 21: The revised slider design, shown from below. The trench along the centre holds the driven part of the lancet, while each pair of holes (top and bottom) accommodates an SMA wire. [72] ©2016 IEEE.

passing through a small notch to prevent it from rubbing between the slider bottom and the floor) and loop back through the neighbouring hole from the top.

The additional hole increased the area of contact of the wire with the slider and stood to reduce pressure of the wire on the slider (which was otherwise known to cause pressure-melting and reduction of the effective tension that the wire could deliver to the slider). It also widened the slider — this was good in terms of strengthening the material bridging the notch (hereafter called the “trench” due to its greater length relative to depth), and acceptable in terms of extra volume (height being more important than width for the actuator function).

Opposing tension could still be provided to the opposite end of the slider by a biasing spring, or by a second SMA wire if desired. The slider could be easily disengaged from the needle, allowing removal of the needle along with the disposable base.

The abandonment of the rack design by the slider was accompanied by removal of the track from the base. The driven shank of the L, held down by the trench, would lie on the surface of the base next to the channel, shown in Fig. 22.

***In vitro* testing**

The new assembly required testing before integration with the e-Mosquito prototype. A larger segment of the base was designed, with:

- holes surrounding the space in which the slider would move, for attachment of a flat cover over the space;
- an extension on one end, to allow space to mount the SMA wires on the base instead of on the underside of a PCB; and
- holes at the end of the extension to allow loops of steel wire that would act as pulleys for the SMA wire.

The parts were all printed with ABS and assembled as represented in Fig. 23. This assembly was then mounted on a force test

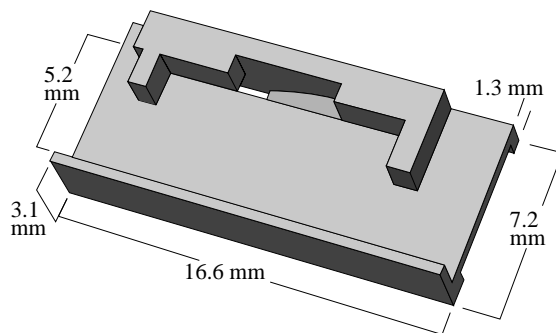


Figure 22: Key section of the redesigned base. The channel is visible at the top, while the slider moves the driven part of the lancet parallel to the longitudinal, from right to left for insertion. [72] ©2016 IEEE.

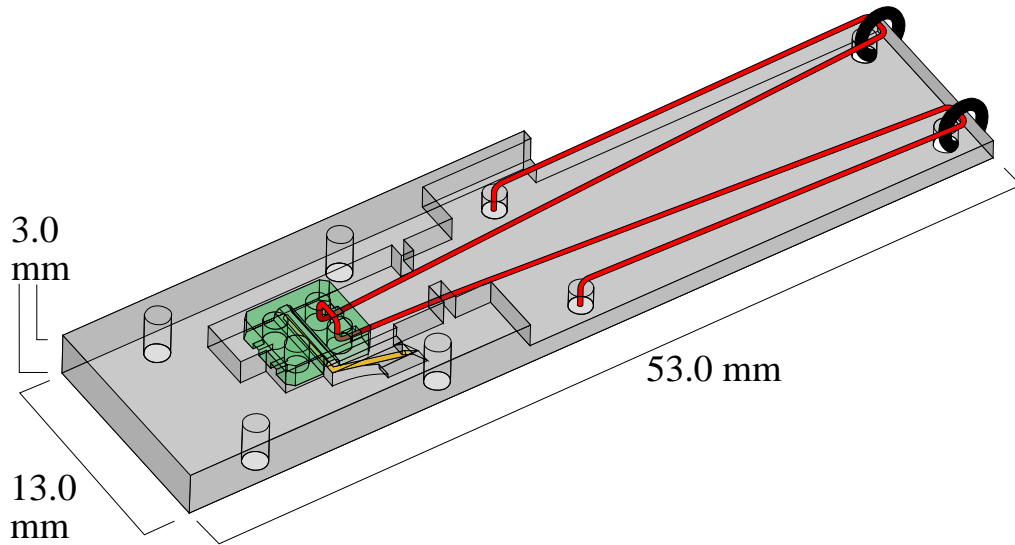


Figure 23: Model of the test assembly, showing SMA wire (red), casing base (grey), slider (green), needle (yellow), and steel wire (black rings). The slider cover and crimp sleeves are not shown.

stand (described in [25]) so that the end of the channel was positioned over a vertically movable load cell (Load Cell 2, mounted atop Micrometer 2 — see Fig. 4 in [25]). For visual clarity, this is represented with a physical model in Fig. 24, where the black ABS base has been replaced with one of matching dimensions made from machined PMMA. As described in [72] (©2016 IEEE):

The wire (1) passed through the crimp sleeves (2), around the steel wires (3), and through the slider (4, in the extended position). In the figure, the slider is positioned corresponding to a contracted SMA wire. The segment of steel wire (5) illustrates the position of the needle arm when the slider was in the retracted position. Current was supplied through eyelet terminals (6) attached to the ends of the SMA wire. The assembly was fixed atop the force test stand screws with plastic nuts (7), the strain gauge (8)

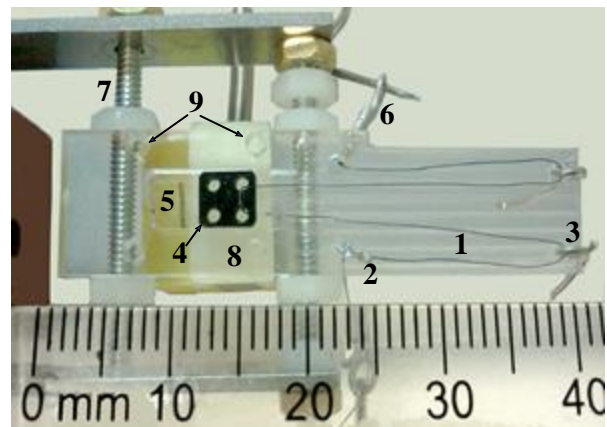


Figure 24: Model of the test assembly used for force testing, with a machined PMMA casing for better visibility. The model includes: SMA wire (1), crimp sleeves (2), steel wires acting as pulleys (3), slider (4), steel wire representing driven part (5), eyelet terminals (6), test stand screws and nuts (7); cover over strain gauge (8) and holes (9) for the slider cover. [72] ©2016 IEEE.

located between them. The cover (not shown) was attached with wires passed through holes (9) in the base piece.

The load cell was driven with $\pm 6V$ and the output voltage was amplified with a gain of 250 by an instrumentation amplifier (AD 624, Analog Devices, Norwood, MA, USA — see [86] for configuration), digitized and recorded (with a USB-6501 data acquisition module and LabVIEW Signal Express software from National Instruments, Austin, Texas, USA).

By adjusting the micrometer, the vertical distance between the top of the load cell and the bottom of the base could be controlled with sub-millimetre resolution. For each 0.1-mm increment from 0 to 2.3 mm, the lancet was manually retracted, a 3.7 V Li-ion battery connected to either end of the wire for 5 seconds, and the stable peak voltage in the resulting record used to identify the vertical force that the lancet delivered to the load cell upon contact. Forces were derived from comparison of this voltage with the voltages produced by various weights upon the cell.

The relationship of these forces with vertical extensions is presented in Fig. 25, and resembles exponential decay, with a peak force of 290 gf (zero extension) and 30 gf at 1.4 mm. The force would reach zero when the distance exceeded the maximal extensible length of the lancet or the extended length at the furthest position to which contraction of the SMA wire could bring the lancet. The force for extension beyond 1 mm appeared sufficient to allow a vertically inserted lancet to reach the capillaries.

The more pressing question was whether the device could penetrate real skin. This was initially verified with porcine leg skin — previously frozen but unprocessed, backed in places with fat, the whole varying in uncompressed thickness from 1.75 mm to 2 mm). A square (sides 2 cm long) was warmed to 37 °C and laid on a flat surface. The actuator assembly was

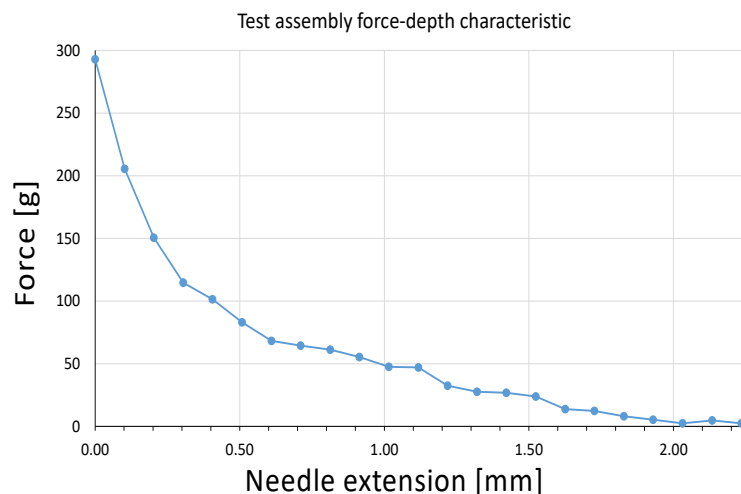


Figure 25: Vertical force-distance characteristic produced with the assembly represented in Fig. 24. [72] ©2016 IEEE.

pressed against it (lightly, 70–220 gf, or firmly, 800–1200 gf), the needle retracted. The battery was connected to the SMA wire for 1–10 s, and the cover removed so that the slider could be immobilized relative to the base. The assembly was carefully lifted while observing the lancet-skin interface. The minimum vertical extension of the lancet from the casing possible for that slider position was measured with digital calipers (Ningbo Great Wall Precision Industrial Co., Yuyao City, Zhejiang, China). The test was repeated 6 times with light pressure and 25 times with firm pressure. Measurement data are listed in Table 4 and presented as a graph in Fig. 26.

The tip of the lancet was consistently observed emerging from the skin and leaving small holes there. As reported in [72] (©2016 IEEE):

Vertical extension was measured at 0.7–1.1 mm for light pressure (mean: 0.93 mm, standard deviation: 0.17 mm) and 0.7–1.5 mm for firm pressure (1.13 mm, 0.25 mm). Variability in extension resulted from skin toughness, looseness of the grip of the slider on the needle (the needle’s vertical extension could vary by up to 0.3 mm while the slider remained stationary), and the manual measurement technique.

While penetration depth increased slightly with electric current duration up to about 7 s, the rise was so small relative to the variability of the data that it should be ignored.

The decline in exerted force (Fig. 25) resembled exponential decay — not because deformed SMA wire behaves like a nonlinear spring, but more likely due to increasing losses throughout the actuator. These losses included:

Table 4: Lancet extension lengths measured during porcine skin penetration testing.

Pressure	Time [s]	Distance [mm]	Pressure	Time [s]	Distance [mm]	Pressure	Time [s]	Distance [mm]
light	10	0.7	firm	9	1.35	firm	10	1.05
Light	2	0.8	firm	1	0.9	firm	10	1.45
Light	5	0.9	firm	3	1	firm	10	1.55
Light	10	0.9	firm	2	1	firm	10	0.95
Light	10	1.1	firm	5	0.95	firm	10	0.7
Light	8	1.2	firm	3	1.15	firm	10	0.96
Firm	5	1	firm	3	1.3	firm	10	1.52
Firm	6	1	firm	10	1.4	firm	5	1.06
Firm	5	1.1	firm	10	1.5	firm	1	0.85
Firm	7	1.1	firm	10	1.5	firm	3	0.7
Firm	5	1.1						

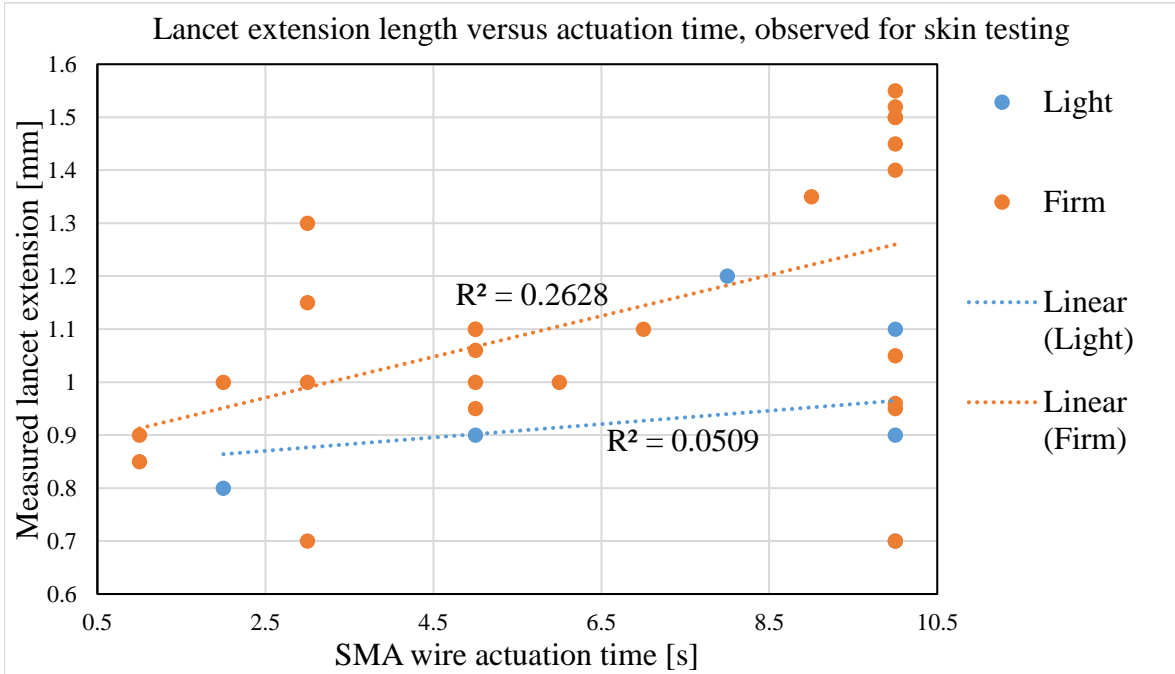


Figure 26: Graph of measured lancet extension versus actuation time for light and firm pressure of the test assembly base against porcine skin.

- the increasing friction experienced by the lancet it pushed deeper into the skin and increased the area of contact with displaced tissues in the skin;
- the increasing cooling of the SMA wire, which was proportional to the (increasing) difference between the temperature of the wire and the temperature of the surrounding air; and
- decreasing conversion of the horizontal displacement of the driven part of the needle to vertical extension of the tip, which occurred as the angle between the needle and the skin approached 90°.

The lancet extensions obtained with firm pressure appeared sufficient to reach capillary vessels, should the lancet reach this depth in the skin. The new mechanism, though requiring 30% less thickness than its predecessor when produced using the same production technology, was more dependent on part manufacturing precision for proper regulation of lancet θ due to the sliding-rotating interface between lancet and slider. Thus, the design would require further manufacturing refinement to work *in vivo*.

An assessment of the maximum extension depth is also worthwhile. The prototype used 110 mm of SMA wire (between the two attachment points), rated for a contraction of around 4% [64]. The two halves of the wire to either side of the slider ran mechanically in parallel, delivering to the slider half the displacement and twice the force that it would receive if connected to the end of a single, straight 110-mm wire contracting by 4%. The maximum theoretical contraction for the wire, 4% of 55 mm, or 2.2 mm, was the maximum horizontal translation of the slider, which was also limited to the slider space within the base (Fig. 24). The maximum vertical extension of the lancet was quite close to this, at 2.05 mm (and this should be expected, since the sharp end of the lancet rested nearly horizontally inside the base when retracted, and rotated nearly 90° to point fully extend). However, this was the distance that the lancet could hang down from the casing bottom, not necessarily how far it would extend when resisted by the skin. As visible in Fig. 15, for most of the available range of movement, a given horizontal position of the driven shank corresponds not to a single lancet angle θ , but to a range of possible angles. At the end of this range, θ should still be forced to achieve 0°. In practice, the smallest θ enforced at maximum translation was measured at 45°, corresponding to

$$extension_{vertical} = length_{needle} \sin(\theta) - height_{channel} = 5 \sin(45^\circ) - 1.8 = 1.7 \text{ mm}.$$

This was the maximum that the conservative measurement method used in the tests could have obtained.

This difference between the desired and actual orientations of the lancet, ϕ_{yz} (an angle in the yz plane, where z is the aforementioned vertical and y is the axis of motion of the slider) was not due to the characteristics of the channel along the axis of translation. At maximum translation, the slider indeed brought the upper part of the sharp end of the lancet (near the bend of L, Fig. 17) to rest against the ledge of the overhang (Fig. 15, 19). The cause lay in failure to realize a different assumption of the model: full restriction of all other undesired DOFs. Any opposing force from the skin would be transmitted by the lancet tip to other parts of the needle, which would tend to move in any direction that would reduce pressure of the tip on the skin. The worst translations that could result from under-restricted translational DOFs were simple to predict:

- translation in x was irrelevant,
- translation in y would reduce the effective horizontal translation of the lancet shank and

- translation in z would directly reduce vertical extension.

The remaining undesired rotations φ in the other planes were more complex. If the channel was wider than the lancet shaft, and the shank was similarly loose due to being narrower than the distance between the surface of the base below the shank and the roof of the trench surrounding the shank, then this might allow an unwanted rotation φ_{xz} (the worst-case scenario for the channel is shown in Fig. 27). Also of concern was the analogous rotation φ_{xy} of the lancet shank inside the trench (Fig. 28). Simulation using R (see Appendix A, “Undesired rotational degrees of freedom”) found that this could be limited to 3° with a 4 mm lancet shank (still 0.45 mm in diameter) in a 0.6-mm-wide trench, which would also limit the y DOF to 0.15 mm.

Even with perfect DFM and production resulting in perfect internal DOF restriction, the actuator would still not fully extend the lancet if the SMA wire ran out of force before the driven shank reached the maximal position. The lancet faced direct resistance in front of the tip (piercing resistance), resistance to rotation (cutting resistance), and friction from the displaced tissue pressing against the sides of the lancet as they slid past it (sliding resistance). This is addressed later.

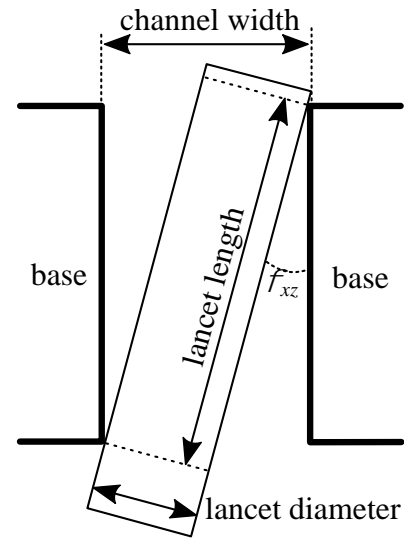


Figure 27: Undesired rotation of the lancet in the xz plane, due to channel width exceeding lancet diameter. Relevant parameters are marked.

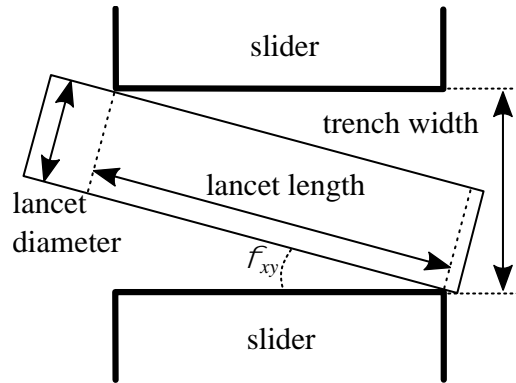


Figure 28: Undesired rotation of the lancet shank in the xy plane, enabled by a trench width greater than the lancet diameter. Relevant parameters are marked.

Chapter 4: Translating-rotating refinements

Integration design

To reduce ϕ_{xz} , the channel had to be narrowed in x , and ideally produced without overhangs. The functional section of the base was redesigned so that a cell could be produced in two parts — a thin base floor (Fig. 29) to support the slider(s) and lancet shank(s) and a thicker, narrower base channel section containing the channel (Fig. 30). In this way, the floor and the channel sidewall could each be printed flat and without overhangs (free of supports and stringing), then assembled with the major planes perpendicular. The floor served as the connecting piece, with two tabs that could be press-fitted into matching holes in each channel piece, below the channel. Snap fittings are more permanent, but require substantial space for the snapping component and adequate part flexibility, and the 3D-printed features proved too small and brittle. Like snap fits, press fits require surrounding material on all sides, and the extra transitions between parts can add extra tolerances.

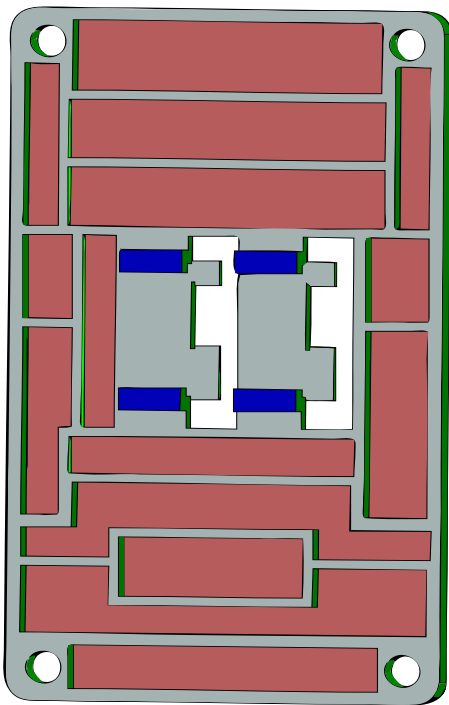


Figure 29: Design of a two-cell base floor piece with tabs for press-fit attachment of two base-channel pieces (Fig. 30). Parts of the floor are thinner (red) to accommodate PCB components, or thicker (grey) to provide structural support.

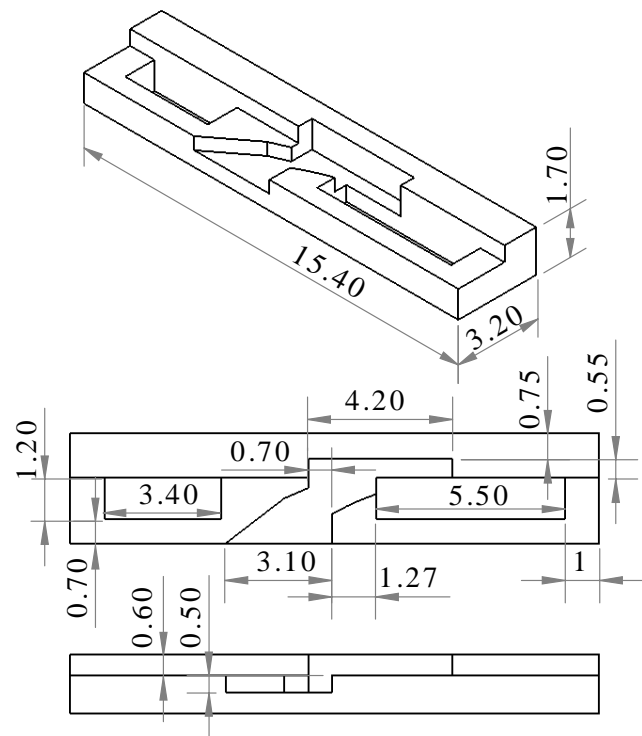


Figure 30: A channel piece implementing the press-fit concept, compatible with the floor piece in Fig. 29. The tab inserted into the slot on the right doubles as part of the lower surface of the channel.

To avoid this, one of the press fit tabs, below the horizontal portion of the channel, was merged with the channel (see Fig. 30) so that the base would serve as part of the channel floor. This also helped to reduce the vertical gap between the (newly possible) roof of the channel and the floor, in which the needle might otherwise lodge.

It was found that, since the lancet could be inserted into the channel during assembly of the base, the channel could be made much tighter, and ϕ_{xz} was reduced so much that the lancet could no longer fall out of the bottom of the base, even when the slider was absent.

The press fit was held together by a third component — a redesigned actuator PCB (Fig. 31) which would serve as the interface between the new actuator and the higher-level electronics of the existing prototype. For compatibility with the latter, no changes were made to:

- the electrical aspects of the actuator control and glucose measurement circuitry present on the board (schematic in Fig. 32, architecture in Fig. 33);
- the outer dimensions (1.6 mm x 35 mm x 62 mm);
- the positions and sizes of unsupported mounting holes — four large ones in the corners, and six smaller ones around the side for precise alignment (small holes removed in subsequent designs); and
- the positions of holes for connective pin housings (six pins on each of three sides).

Compatibility is also the cause of the asymmetry of the layout in Fig. 31: the previous e-Mosquito design used reflectional symmetry for interfacing, yet called for asymmetric integrated circuits.

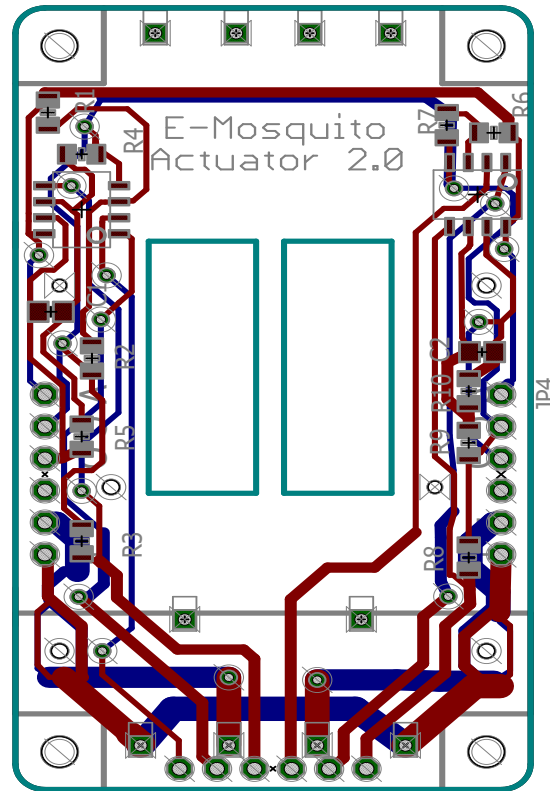


Figure 31: Initial design of two-cell actuator PCB for in-plane actuator. All mounted components are in the top (red) layer. Plated holes with no electrical connections are mounting points for the SMA wires, each looped through a slider (Fig. 21) and otherwise following the path of Fig. 2.

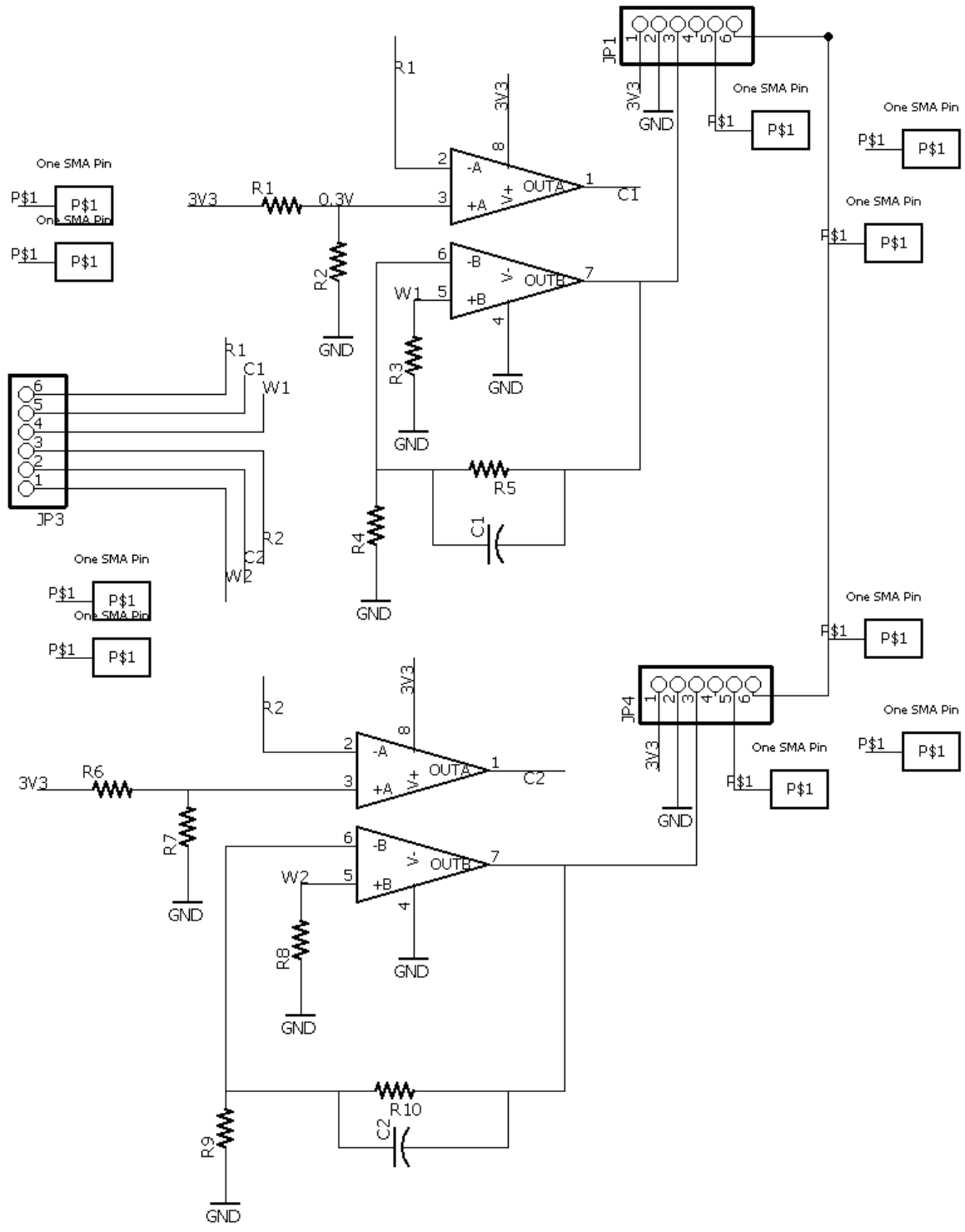


Figure 32: Electrical schematic of the pre-existing control circuitry of the e-Mosquito actuator PCB, preserved in the revised board layout of Fig. 31.

An initial suggestion had been to make the channel piece extend up through the PCB, using the milled openings that previously enabled the interface of the rack and lancet holder. This was

theoretically a practical approach that would:

- reduce thickness by eliminating the space between the PCB and the base-floor and
- keep the key electronics (on top of the PCB) separate from the replaceable component of the mechanics that would interface from underneath.

On this basis, the SMA wires and components were all mounted on the top side (see the red pads in Fig. 31). The slots were each widened to accommodate a channel piece alongside the end-walls of the sliding space (marked blue in Fig. 29). When the assembled base was aligned and meshed with the PCB, the channel section could not separate from the floor. The wider actuator space and the need to prevent contact between the heated wires and the electrical components required rearrangement of the latter. Boards were produced by Alberta Printed Circuits (Calgary, AB, Canada).

The base-floor could rest against the bottom of the PCB, wherever it was not thinned (red in Fig. 29) to accommodate the ends of through-hole components (pins for SMA wire routing and inter-PCB connections). The effective smoothness of the slider-floor interface was increased thanks to improved understanding of the slicing software: base floors were printed oriented so that ABS infill lines were parallel to the axis of the slider track.

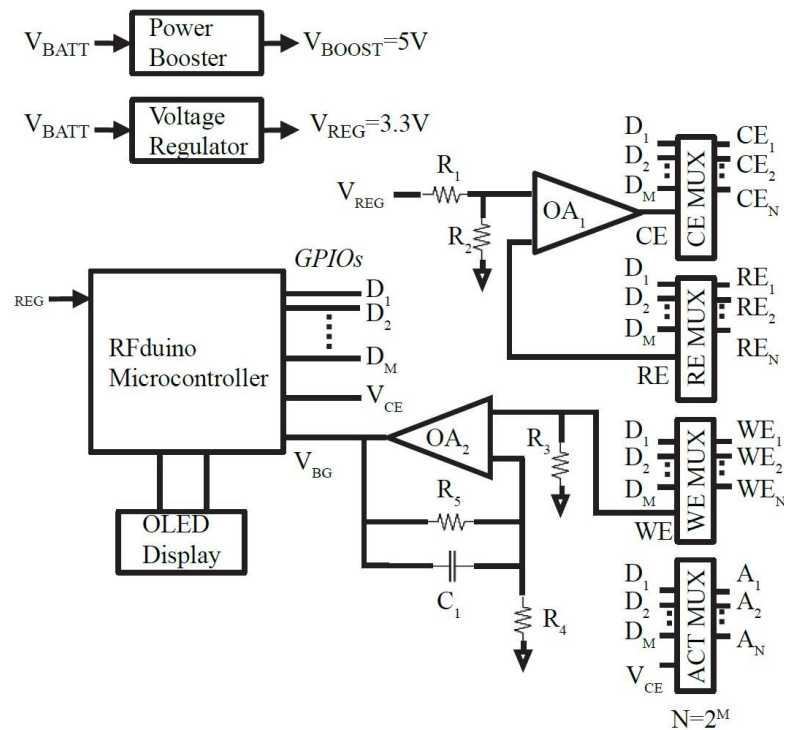


Figure 33: Architecture of the pre-existing, autonomous e-Mosquito wearable, as presented in [27] (©2016 IEEE). Power supply, processing and display systems (left) were located on upper PCBs, while actuation and glucose measurement circuitry (right, shown for one test cell) was located on the actuator PCB. The revised placement and routing of components on the circuit board did not electrically alter any part of this system.

For initial testing, an ABS cover layer was used to restrict the sliders from above. As the tops of the sliders were level with the top of the PCB, additional features were needed to restrict the sliders without interfering with other components; ridges were used (Fig. 34).

Once all components were manufactured, the system was assembled for testing in a minimal configuration, consisting of only one functional cell and omitting the control circuitry used in the e-Mosquito in favour of direct control of the actuation current. The assembly procedure was as follows:

1. Copper pulleys (3 mm in diameter, included with BMF nitinol wires purchased from Toki Corporation) were mounted on the board with brass pins (1 mm in diameter) soldered in the electrically isolated plated holes on the PCB (symmetrically arranged on either side of the line of motion of the slider), so that the pulleys could rotate freely around the pins.
2. A biasing spring was soldered to the remaining isolated hole (approximately on the line of motion) and the other end was bent to pass through one end of the slider.
3. Nitinol wire was passed through the two holes on the other end of the slider, wrapped around the pulleys and passed through the appropriate holes in the PCB. Once on the other side of the board, each end of the wire was crimped with a crimp bead (also included with the wire). Each bead was then soldered to the plating of the hole so that the wire was taut when the slider was in a position corresponding to full retraction of the needle (biasing spring unstretched).
4. For each of the two PCB traces now electrically connected to the ends of the nitinol wire, one end of a different insulated copper wire (1 mm in diameter) was soldered in a plated through-hole connected to the trace. The wires led off the PCB could be connected to a Li-ion battery.

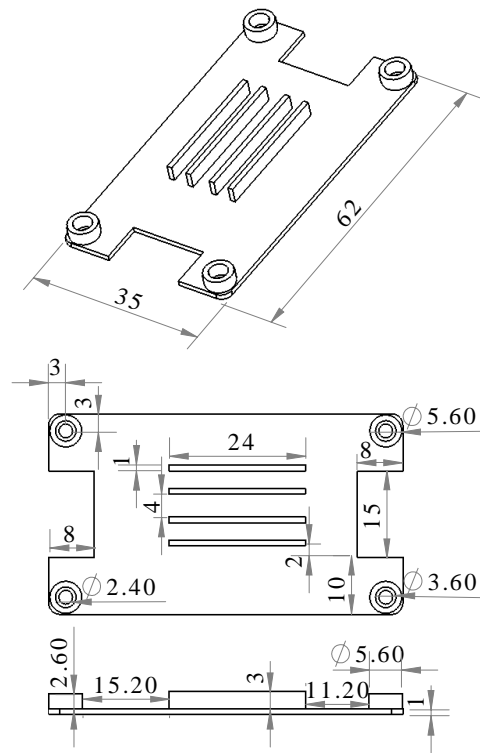


Figure 34: Dimensions of the slider cover, shown from below. Each pair of ridges is meant to support one slider.

5. A lancet needle was bent and cut to produce an L shape with the approximate dimensions of Fig. 17.
6. The dull arm of the L was placed on the section of the plastic base piece where it would slide, and a channel piece was press-fitted onto the tabs of the base piece, with care taken to ensure that the sharp end of the lancet was in the channel.
7. The assembled base was aligned with the PCB, so that the slider, the channel piece and the raised tabs on the base piece (blue in Fig. 29) fit into a slot in the PCB.
8. A cover layer was positioned over the circuit board so that ridges pressed the slider against the base piece and the corner holes of the cover were aligned with those of the PCB and the base piece.
9. The base piece, PCB and cover layer were attached with steel screws (2.3 mm in diameter) passed through each set of corner holes and secured with hex nuts.

Variants of this assembly procedure would be used to assemble all subsequent designs.

The assembly was now ready for *in vivo* testing. Testing of this and all subsequent designs was entirely qualitative in nature: for initial testing, the investigation was concerned not with the quantitative parameters of actuator performance, but merely with basic adequacy. This would be determined by a series of questions, each applicable only given a positive answer to the previous:

1. Could the actuator extend a lancet against the resistance of the skin?
2. Could the extension of this lancet produce a bleeding wound?
3. Would such a wound release a volume of blood sufficient to fill the sample volume (1 μL) of a glucose test strip?
4. Would this much blood actually reach and fill a test strip adjacent to the wound site?
5. Would this process be less painful to the wearer than a fingerstick test?

Initial tests of this and all subsequent designs were always concerned with the first two questions.

All tests were performed on one informed, consenting, adult, male volunteer, and consisted of:

1. preparing a new L-shaped lancet and channel piece;
2. sterilizing these and the base piece with rubbing alcohol and assembling the disposable section of the actuator (steps 6–9 of the previous procedure, or their equivalent for later designs with different components);

3. the volunteer washing his hands and sterilizing the skin of the left wrist with rubbing alcohol;
4. firmly pressing the assembled actuator against this area of skin;
5. connecting the jumper wires to a fully charged Li-ion battery for 10 seconds;
6. continuing to press the device for another 10 seconds after the voltage source was removed;
7. removing the device and inspecting it to see whether the needle had retracted;
8. inspecting the skin of the forearm around the channel site for wounding and blood, with observation continuing for 30 seconds after removal; and
9. disassembling the disposable section and disposing of the needle (in a separate sharps container) and the channel piece.

While this simple routine would not be enough to prove the effectiveness of the device, it would be quite sufficient to falsify that effectiveness, thus saving a great deal of effort that might be wasted on testing of a non-functional prototype. The procedure would be repeated up to ten times per design, and a series of bleeding wounds producing adequate blood would provide grounds to add glucose test strips and conduct tests on a greater number of volunteers, who would likely exhibit different skin and blood flow characteristics.

The integration prototype encountered problems on the first question: it failed to fully extend the lancet. The slider would move sideways off the ridges (whether there was one or two per cell), or the cover layer would deform, the centre being far from the screws that connected the corners of the different layers. Either of these events would prevent allow the slider to move away from the base piece and thus release the lancet before it fully extended.

Of course, the cover layer was only a surrogate for an upper PCB layer in the original e-Mosquito prototype, and that PCB would not deformation. However, it would still require extended features to restrict the sliders, like the ridges in the cover layer, since the control circuitry atop the actuator PCB would prevent it from directly contacting the top of the slider and directly blocking this undesired upwards motion of the slider. This would increase device thickness, negating the spatial efficiency of this actuator design.

It was concluded that the challenge of precisely coordinating three layers (base, actuator PCB and over layer) to restrict movement of the sliders was unjustified, and that the in-slot arrangement increased complexity without reducing overall volume.

The PCB was instead redesigned to eliminate the milled openings and allow the slider to rest against the bottom surface. The component layout (now all in the bottom layer) was similar, but the part was produced with isolation milling (Fig. 35).

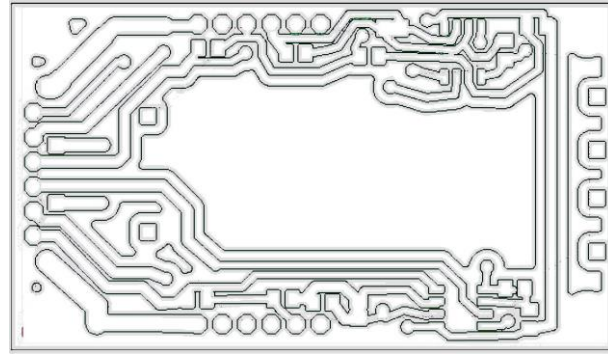


Figure 35: Isolation milling toolpath generated for bottom side of revised PCB.

Press-fitting had also proved problematic: the lancet tip tended to wedge in the gap between the base-floor and base-channel piece and thus did not extend reliably upon actuation. Since the gap could not be eliminated without sacrificing the remaining benefits of two-part channel production, press-fitting was abandoned in favour of a design emphasizing the precision of the slider and track.

Multi-track design

Following the complexity of the previous design, a simpler concept seemingly more appropriate for layered printing was identified (Fig. 36). It recognized that only one point was necessary for rotation and that the form of the manufactured channel would be more predictable if the surface adjoining this point was level.

The channel needed to be narrower to reduce ϕ_{xz} and ϕ_{yz} , and a more reliable means of preventing the lancet shank from wedging between the slider and the base was required. While the track had helped with this when the slider was narrow, a track the full width of the widened slider would make the wire holes quite deep. Worse, it would require even greater cell width so that the end of the lancet

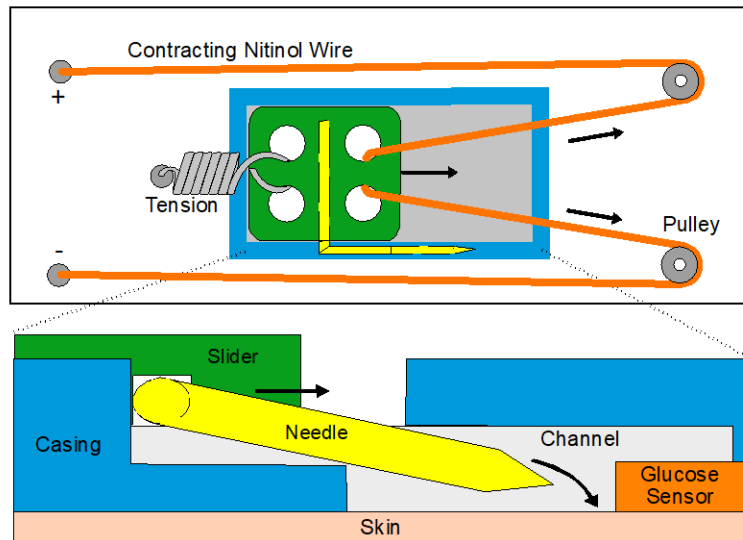


Figure 36: Actuator concept with a revised channel, as presented at IEEE Sensors 2016.

could rest beyond the far side of the track opposite the channel, instead of falling into the track and increasing ϕ_{xz} . I realized that the track could be split into multiple narrower ones, separated by raised lengths of floor that would maintain the height of the shank (Fig. 37, Section B-B).

The design of the tracks was defined by the way in which the slider would interface with them. Instead of the whole slider resting in a single track, narrow ridges now needed to extend from the bottom slider surface, past the shank, and fit into tracks. While two tracks per slider would suffice to keep the shank level, the ridges could not overlap with the wire holes in the slider. Thus, the revised design (Fig. 38) included three ridges, as narrow as the 3D printer would theoretically

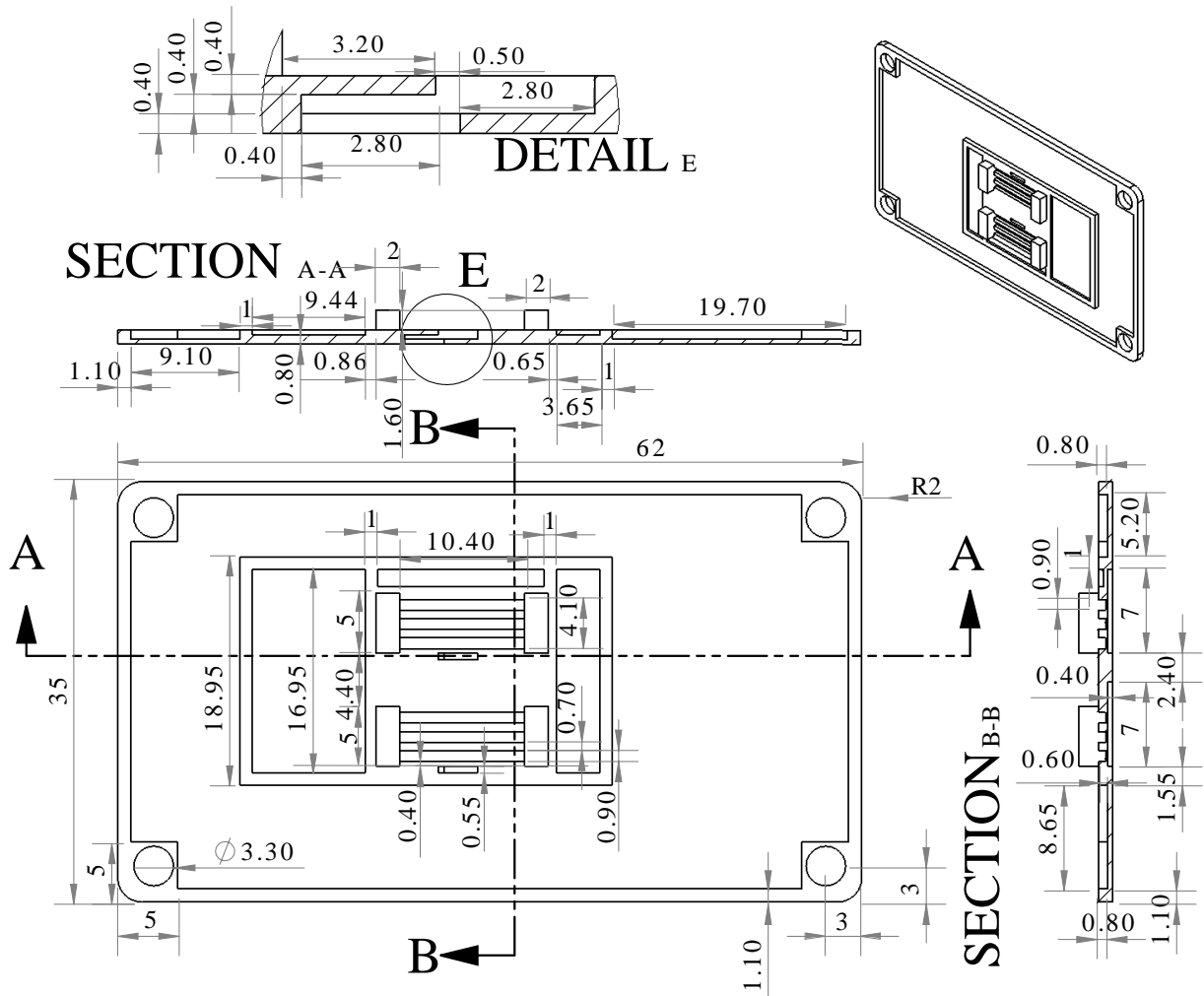


Figure 37: Dimensions of the revised unified base.

permit and with substantial clearance around the wire holes, as both ridges and holes would be printed with substantial tolerance. By the same logic, the corresponding three tracks in each cell of the base were designed to be wider than the ridges, to prevent the slider from jamming due to possible imperfections.

A drawback of the ridges was that they were extremely fine structures. Their designed widths of 0.4 mm matched the nozzle diameter of the Replicator 2X printer. Each ridge must thus be printed as a single-thickness wall, with the slider containing six such walls because the ridges could not cross the trench (Fig. 38). The driven shank needed to be inserted into the trench from below for easy replacement of disposable parts; any material on the slider below the trench would block this, even if it did not prevent the shank from fitting snugly inside the trench when inserted from the side. The slicing software (MakerBot Desktop) could plan single-thickness walls for the ridges, but consistently moved directly from the end of one ridge to the beginning of the nearest ridge across the trench. Though extrusion was halted during this movement, stringing formed undesired “bridges” over the trench. These were as strong as the (fragile) ridges, making manual removal impractical.

Production of the slider drove the shift to CNC milling. Having no overhangs, the slider was easily milled upside-down from a sheet of 2-mm-thick ABS; the base proved much more difficult. Since:

- an element of the base had to be above the lancet to deliver downwards force to it,
- the lancet tip should not protrude below the base when retracted and
- part of the lancet must remain in the channel to ensure advance through it when driven by the slider,

the ledge and the space below were essential. The narrow width of the channel, necessary to restrict φ_{xz} and φ_{xy} , also exceeded the capabilities of printing. 0.5-mm-diameter holes tended to close if printed with FDM, and trial-and-error might eventually produce simple ones using a larger

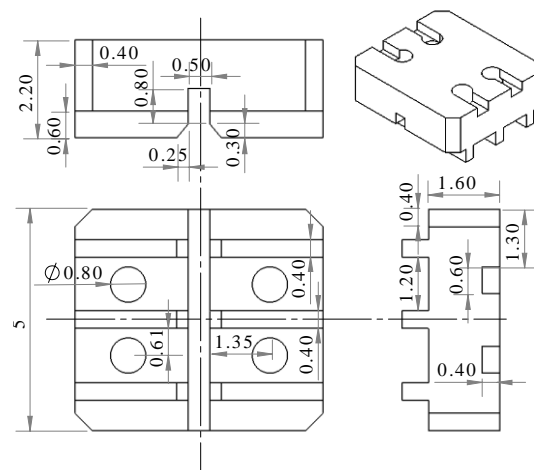


Figure 38: Dimensions of the revised slider design with three ridges, compatible with Fig. 37.

diameter, but not a complex opening with an overhang. In 3-axis milling, the channel required machining from both above and below, which required manual flipping of the stock. The challenge thus became one of producing a precise toolpath and of aligning the features produced through milling of the bottom with those milled from the top.

As MeshCAM was poorly suited for directing a small cutter along a specific path, the following manual G-code was used to plan individual movements and to implement the wasteboard-nail method (“Positioning and workholding” — Chapter 2). The following G-code was used to produce the channel in 1.6-mm-thick ABS stock using a 0.4-mm cutting bit:

g1 x0 y0 z1 f200	through other side, realign nails
m3 s9000	with holes in wasteboard)
(drill 4 symmetric openings, drive	z1 f200
nails through them and into	(change y position until cutter is over
wasteboard)	hole).
g1 z-1.8 f75	m3 s9000
z-0.8	z-0.8
y5	y5
z1	z1
m5	m5
z40 f300	z40 f30 (retract cutter)
(remove nails, flip board 180° around	
CNC x-axis, insert nails	

Besides ensuring that the channel cuts on each side overlapped correctly (and shared orientation) in *X* and *Y*, there was also the matter of alignment of depths in the *Z* dimension. Slight deflection of the part surface away from the board and a tendency of the stock to slide up the nails (which could not be hammered down fully due to the need to remove them afterwards) sometimes resulted in the bottom being cut deeper than intended (potentially destroying the overhang). Satisfactory channels were ultimately produced.

By manually modifying the .nc file produced by Carbide Motion, simplified manual code was produced for the whole base piece (see Appendix C, “Two-sided base piece”). The following sequence of operations was used for a 1.6 mm-thick sheet of ABS stock with one smooth side and one textured side:

1. Attach the stock to the wasteboard with adhesive, smooth side up.

2. Use a 0.8-mm-diameter cutting bit to make four corner holes around the part area, each extending through the stock and into the board. Drive 1 mm nails into the openings.
3. Mill the bottom of each complex channel.
4. Remove the nails, flip the board around X (so that it is now upside-down and front-to-back), insert the nails into the openings from the new top side and into the openings in the wasteboard.
5. Use a large diameter bit to quickly remove the top 0.4 mm of the stock, leaving 1.2 mm; the surface is now at $Z = -0.4$ mm for all subsequent features.
6. Use a 0.4-mm bit to mill the top of each complex channel (a 0.8-mm-deep slot 5 mm long).
7. Use a 0.8-mm bit to mill the trio of parallel tracks next to each opening.
8. Use a 1.6-mm bit to produce the openings for the corner screws and cut the base piece out of the stock.

Several attempts were required before a part design compatible with the PCB was produced. At this point, it was possible to assemble a rough powered prototype (Fig. 39) that could be tested against the skin using the same test procedure as was described for the integration design (with assembly steps simplified due to design revisions).

The target concept (Fig. 36) had finally been implemented, yet the result was unsatisfactory. The multiple tracks and ridges required considerable dexterity to fit together, impractical in any consumer device. Worse, while the lancet extended, it did not puncture when the assembly was pressed against the skin and actuated for 10 s, instead pressing sideways against the skin. More detailed analysis and modification were required to ensure that the lancet would initially extend with a point-first piecing motion.



Figure 39: Bottom side of the milled PCB with one actuator cell attached. Transparent tape isolates the SMA wire from the board. All pulleys are isolated.

Channel optimization

The idealized channel yz cross-section for the first working prototype produced by the manual code (Appendix C, “Two-sided base piece”) is presented in Fig. 40. The translation space of 5 mm was more than required by the lancet, but not responsible for the problem of angle of approach.

For the approximate analysis of insertion, the lancet-channel geometry could be simplified by:

- ignoring non-driving geometry such as the lower-left side of the channel,
- ignoring minor dimensions such as lancet diameter,
- ignoring deformations and imperfections such as φ and
- adopting a two-dimensional coordinate system (yz becoming xy).

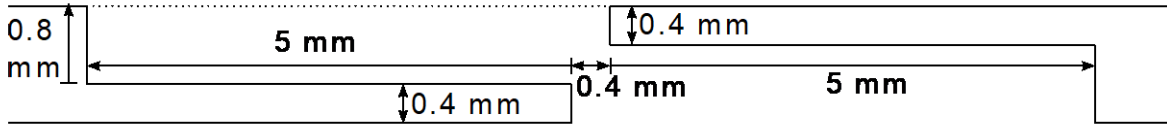


Figure 40: Cross-section of the channel (yz) as produced by the code of Appendix C.

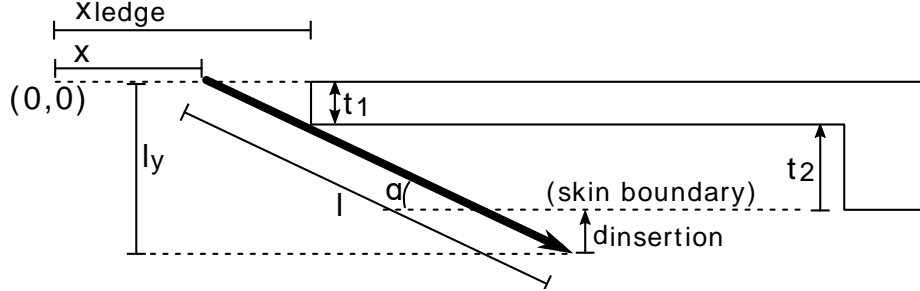


Figure 41: Simplified representation of geometry relevant to idealized motion of the lancet during insertion into the skin, based on the channel geometry of Fig. 40.

In the resulting system (Fig. 41), l was the rotating length of the lancet and $\alpha = 90^\circ - \theta$ is the lancet angle relative to the skin. The upper end of the lancet was restricted to $y = 0$ and moved to the right during insertion, while the other end faced upwards resistance from the skin. The lancet was thus pressed against the lower corner of the ledge ($x_{ledge}, -t_1$), which served as the centre of rotation so long as the motion of the lancet was not restricted by another immobile point. This enforced an insertion depth

$$d_{insertion} = l_y - t \quad (1)$$

where $l_y = l \cdot \sin(\alpha)$ is the vertical projection of the lancet and $t = t_1 + t_2$ is the thickness of the base piece below the line of motion of the lancet. Based on the triangle in the upper-left corner,

$$\sin(\alpha) = \frac{t_1}{\sqrt{(x_{ledge} - x)^2 + t_1^2}} \quad (2)$$

Thus, differentiation of (1) with respect to the distance x of the upper end from its initial position at the origin yielded the vertical extension rate

$$\frac{\partial d_{insertion}}{\partial x} = \frac{lt_1(x_{ledge} - x)}{\left((x_{ledge} - x)^2 + t_1^2\right)^{\frac{3}{2}}} \quad (3)$$

which could be treated as a non-partial derivative in the context of a single design. A point-by-point simulation (see Appendix A. “Simulated lancet paths for ledge-driven rotation”) of this rate was performed using the dimensions from Fig. 40 and a 3.2 mm lancet beginning its motion with the driven shank 2 mm from the ledge. It yielded an extension rate curve that peaks and begins to decline before the lancet has fully extended, reaching 0 when the angle reaches 90° at 2 mm translation (Fig. 42).

Angle and vertical extension rate versus horizontal translation, geometry 1

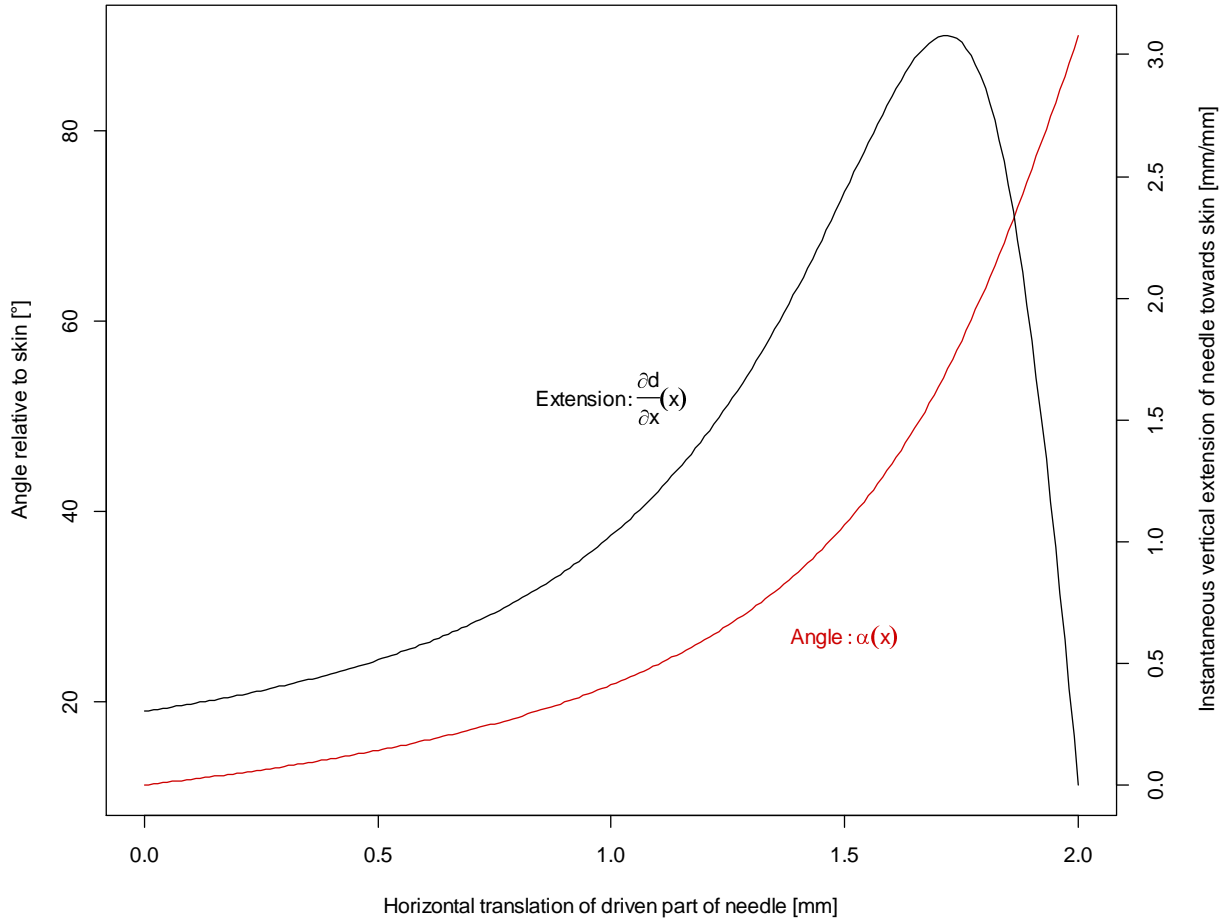


Figure 42: Graph of lancet extension rate (3) and angle (2) relative to the skin as functions of translation of the driven part of the lancet; $x_{ledge} = 3.2 \text{ mm}$, $l = 2 \text{ mm}$, other dimensions as in Fig. 40.

Though it verifies aspects of the model, Fig. 42 does little to visualize the motion of the lancet. Fig. 43 shows the paths of the driven part and tip of the lancet for the range of positions resulting from the rightward movement of the driven part. The model neglects lancet diameter while illustrating the effect of the lower ledge corner (2, -0.4) on the motion of the lancet. The angle of the (dotted) path of the tip relative to the lancet body shows whether point-first or sideways motion is dominant during a given stage of insertion. As lines representing the lancet body are shown at equal intervals of progress of the driven part, their greater density early on shows that the rotation of the lancet is initially slow relative to its advance past the corner (resulting in point-first motion), then faster as the motion of the driven part relative to the corner shifts from radial to tangential. The figure would

continue this accidental representation of a sliding Doppler shift, if not for the relevance of other features beginning at $x = x_{ledge}$. Ignoring lancet diameter, the upper ledge corner, at (2, 0) would cause immediate rotation by an additional 90° clockwise, if not for collision with the floor (on the left side of Fig. 40), the boundary of which can be placed at (2, -1.2) in Fig. 43.

The collision was an intended feature of the design, which was meant to deliver the lancet to the point of greatest depth using an actuator technology best suited for short strokes. This contrasts with the concept of Fig. 44, included in a patent application [87] for the ledge rotation concept, which demonstrates a geometry that would permit a bladed instrument to rotate nearly 180° through the skin and withdraw from it without reversing direction.

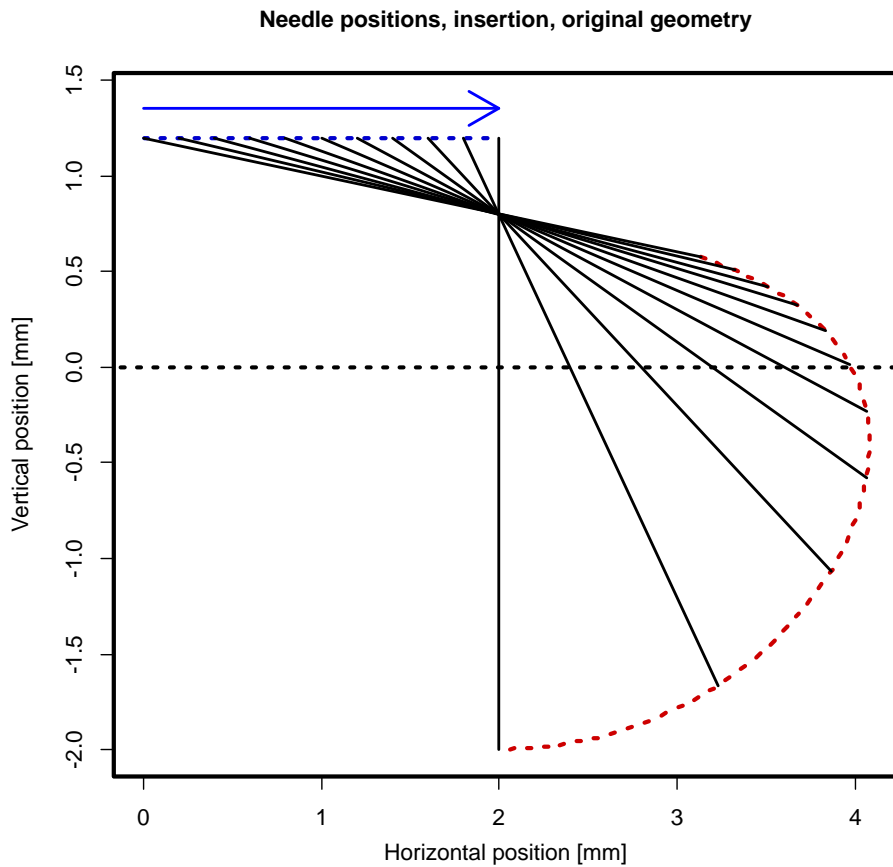


Figure 43: Visualization of the path of the lancet during insertion into the skin, for the same geometry as Fig. 42. Dotted lines mark the paths of the driven part (upper left) and tip (lower right) as the driven part is moved to the right and the lancet encounters the ledge. Solid lines representing the location of the lancet are shown for every 0.2 mm of translation of the driven part. The undistorted skin boundary runs along $y=0$ mm.

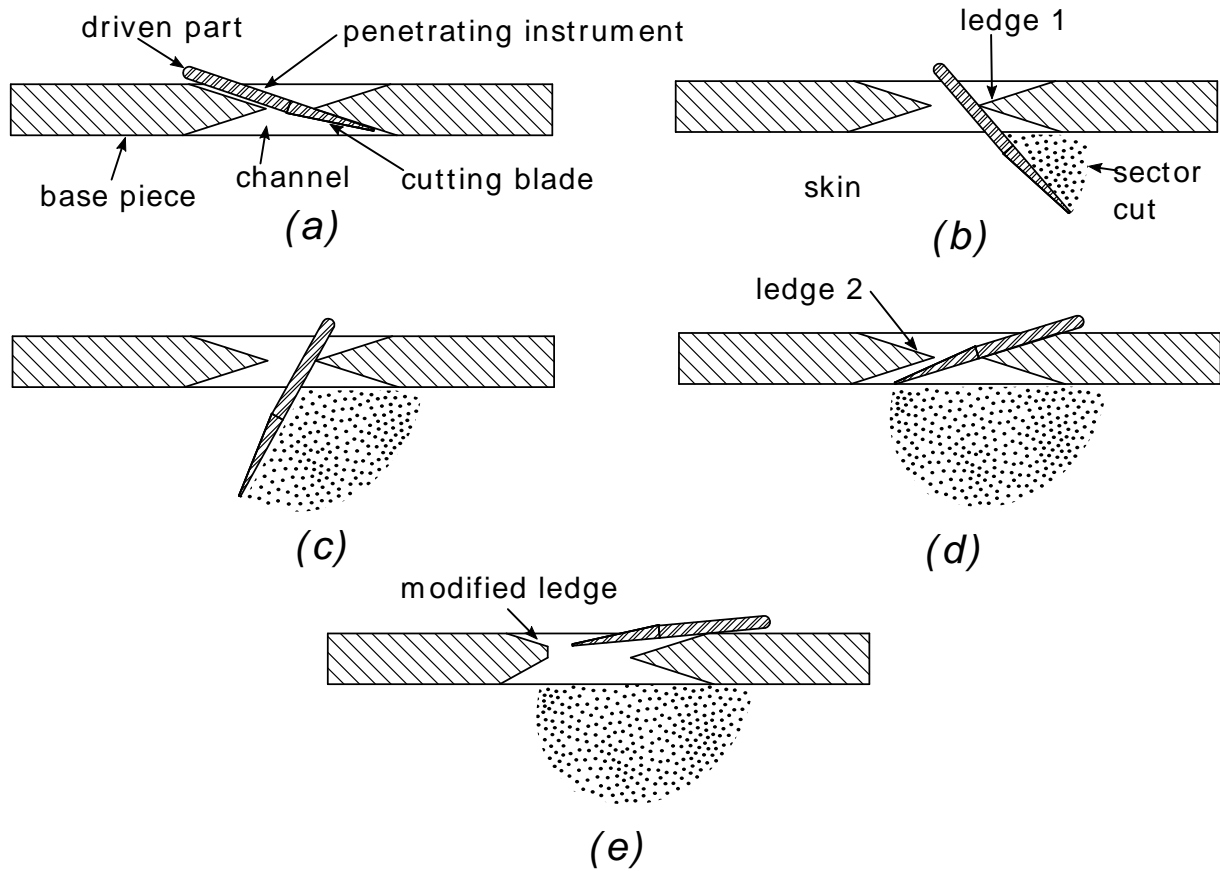


Figure 44: Re-labeled blade concept from the patent application [87]. A penetrating instrument resembling the L-lancet but possessing a blade is driven by the same means (tension applied to the upper end) and caused to move downwards by the ledge corner that it encounters to the right. The driven part continues normally past the point at which the blade is perpendicular to the skin, as the channel opening is wider and there is no upper ledge corner that would accelerate rotation. The left ledge may be modified, as in (e), to allow the blade to retract deeper into the casing and ensure that it is not reused.

Note that the model used in Fig. 43 could be directly applied to the geometry of Fig. 44a-44d. These figures make clear that rotation around a point causes an instrument to pass through tissue mostly laterally when the driven part is near the ledge corner, with point-first (and in the case of Fig. 44c-44d, point-last) motion relegated to the beginning (and end) of the motion. For Fig. 43, the point of entry into the skin occurs past $y = -1$ mm, with relatively little piercing advance remaining before the lancet movement is dominated entirely by rotation. If a needle-type instrument is not well embedded in the skin when major rotation begins, it is unlikely to break through after that (unlike the blade-type instrument of Fig. 44).

In contrast to a corner, a surface encourages point-first movement, since a flat surface can only alter the angle of a straight instrument through contact with the tip of the instrument, and is thus far from the driven part when in contact with the tip. Early designs of the part (Fig. 15) even detailed guiding surfaces, envisioning that a needle tip would travel along a downward-sloping wall. The downward slope was removed in “Multi-track design”, when it was realized that the surfaces themselves were irrelevant from the moment at which the lancet actually contacted the skin — once the tip of the lancet was touching skin, all contact between the lancet and the fixed geometry of the device must be via the lancet body, and therefore consist of edge-edge contacts. Fig. 40, the first channel design to be manufactured exactly as designed (rather than using software approximations), thus relied exclusively on the lower ledge corner.

However, the design overlooked the importance of the height of the rotation ledge. As demonstrated in Fig. 45 (lower right), locating the corner closer to the skin would privilege piercing motion with a far greater initial radius of rotation, allowing the lancet to pierce further before rotation.

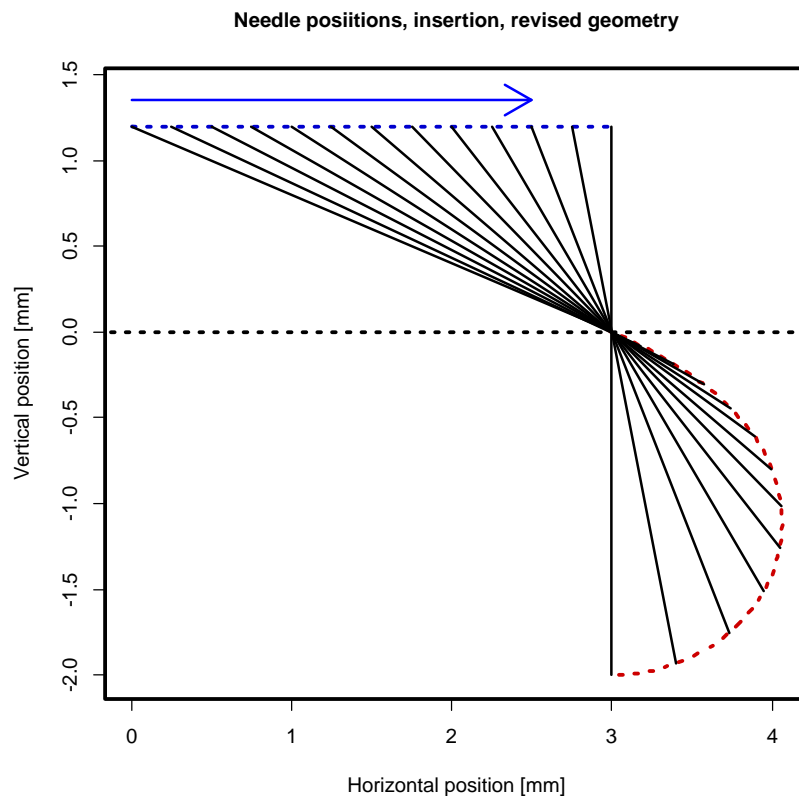


Figure 45: Visualization of the path of the lancet, analogous to Fig. 43, when the corner is brought closer to the skin.

On this basis, the design of the channel was adjusted, to the dashed outline of Fig. 46. The lateral (yz) cross-section of the opening in the top side of the base became roughly triangular, produced with two cutting passes. The overhang ensuring that the lancet remained pointed toward the skin when retracted was minimized, accommodating only the narrow tip of the lancet. As a result, the space below was small enough that it could be effectively produced with a utility knife. This greatly simplified the milling process:

- stock material could be taped down,
- the G-code for alignment holes omitted and
- certain code segments rearranged without requiring additional tool changes.

The resulting base piece functioned better than its predecessor, entering the skin but not penetrating deeply enough to produce substantial blood from the capillaries. The identified causes were:

1. difficulty in precisely coordinating the positions of the slider, tracks, channel, biasing spring and length of available SMA wire and
2. looseness of the SMA wire in the prototype due to pressure-melting of the slider and gradual escape of the wire from its attachment holes in the PCB.

Parallel and asymmetric wire actuation

To address the previously identified obstacles, the actuator needed to deliver greater displacement to the slider, dependent on fewer factors. A fundamental restriction on powered SMA wire length l_{wire} , due to wire resistance, required wire current and voltages available from compact batteries,

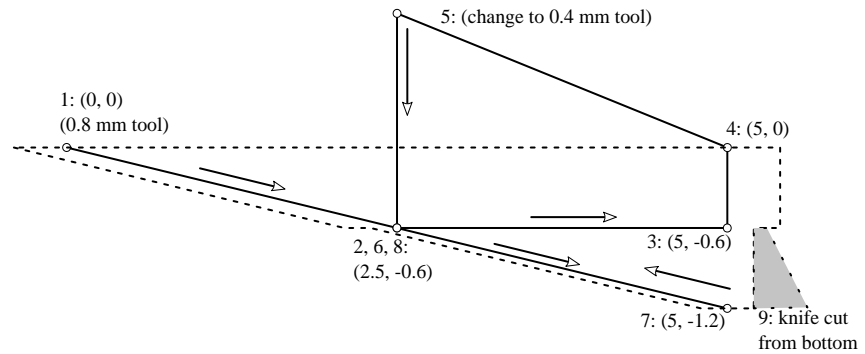


Figure 46: Side view of cutter toolpath for the revised channel. Solid lines and arrows indicate the path of the centre of the downward-pointing cutter tip through the material, with key coordinates relative to the starting point given in millimetres and numbered sequentially. The dashed lines indicate the outline of the cut (taking into account cutter diameter). Note that the tool change and knife cut are loosely represented, that the 0.4 mm cutter is moved by 0.1 mm relative to the viewing plane before returning from 7 to 8. Thus, the bottom of the channel is 0.5 mm wide, while the majority is 0.8 mm wide.

was identified in Chapter 1, “Shape memory effect”. I realized that the volumes of Li-ion batteries did not increase nearly as much with discharge current. While the battery (GSP652535, Great Power Battery Co., LTD, Zhuhai, GD, China) used by the existing e-Mosquito actuator was rated for a maximum discharge current of 1C (equal to its nominal capacity per hour as, i.e. 400 mA since the capacity was 400 mAh), others of similar capacity (e.g. the selected replacement, HJ 882540, Honghaosheng, Guangdong, China) claimed sustained maxima of 20C and several-second bursts of 40C (typically for remote-control aircraft).

I took advantage of the high discharge limits with an approach (Fig. 47) that drew multiple parallel currents from the source and supplied them to mechanically serial segments of the wire. By using conducting pulleys or other sliding electrical contacts, alternating high and low potentials could be established at (mobile) points along the wire, so that the wire effectively consisted of multiple resistors in parallel.

This was the opposite of the arrangement mentioned in [88], which sought to increase force and reduce power by supplying a bundle of wires that were connected in parallel mechanically but in series electrically. In terms of the parallel-heating, serial displacement concept, the new solution was similar to the fluid-based, non-SMA arrangement claimed by [89]. The most similar existing SMA design was [90], which provided for independent heating of individual segments of wire (via additional heating components contacting the wire), presumably using separate current for each segment. This last design was intended for local control of contraction rather than maximum contraction length, and parallel wires were included to increase force.

The parallel-current concept allowed the use of a much longer wire through a flexible approach to electrical contact; a related one doubled the amount of work that a wire of a given diameter could perform in a fixed board space, and simplified wire fixation. When considering how to firmly attach the wire, it seemed easier to securely mount the ends of the wire in a single hole in the PCB. Thus far, both points had been on the board, equidistant from the slider so that the parallel contractions of the two

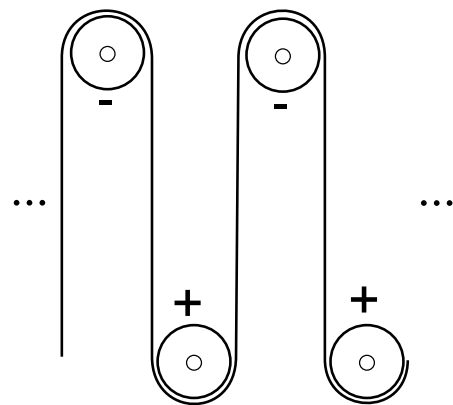


Figure 47: Electromechanical concept of parallel current actuation. Evenly spaced points along the SMA wire are alternately connected to one of two voltages (e.g., V_{cc} and ground) via contacts such as conducting pulleys.

sides would deliver balanced displacements to the wire midpoint passing through the slider, instead of pulling sideways. The parallel sections could share the same asymmetric path (and pulleys) if current could be returned to the PCB through the slider and the biasing spring. This would allow a reduce the board space and the number of mechanical attachment points required for a given wire displacement. The only requirement was that the slider be made from a conductive material.

A 2x3x4 mm concept slider was milled from 3-mm-thick aluminum (Fig. 48; G-code in Appendix C, “Aluminum slider”). The use of metal eliminated concerns about pressure melting, and the use of the same pulley by both sides of the wire passing through the slider reduced twisting. In effect, each end of the slider could be designed with a single hole. A single-track base was used for the narrowed slider, reducing precision concerns and simplifying milling of a relatively difficult material.

Though the lancet was in contact with the slider rather than the SMA wire, and the biasing spring and slider were both in contact with the PCB ground, isolation of the lancet tip was still desirable to prevent currents into the skin. Isolation was achieved by filling a narrow opening in another piece of aluminum with molten PLA and drawing the lancet shank through the opening so that the shank was fully coated.

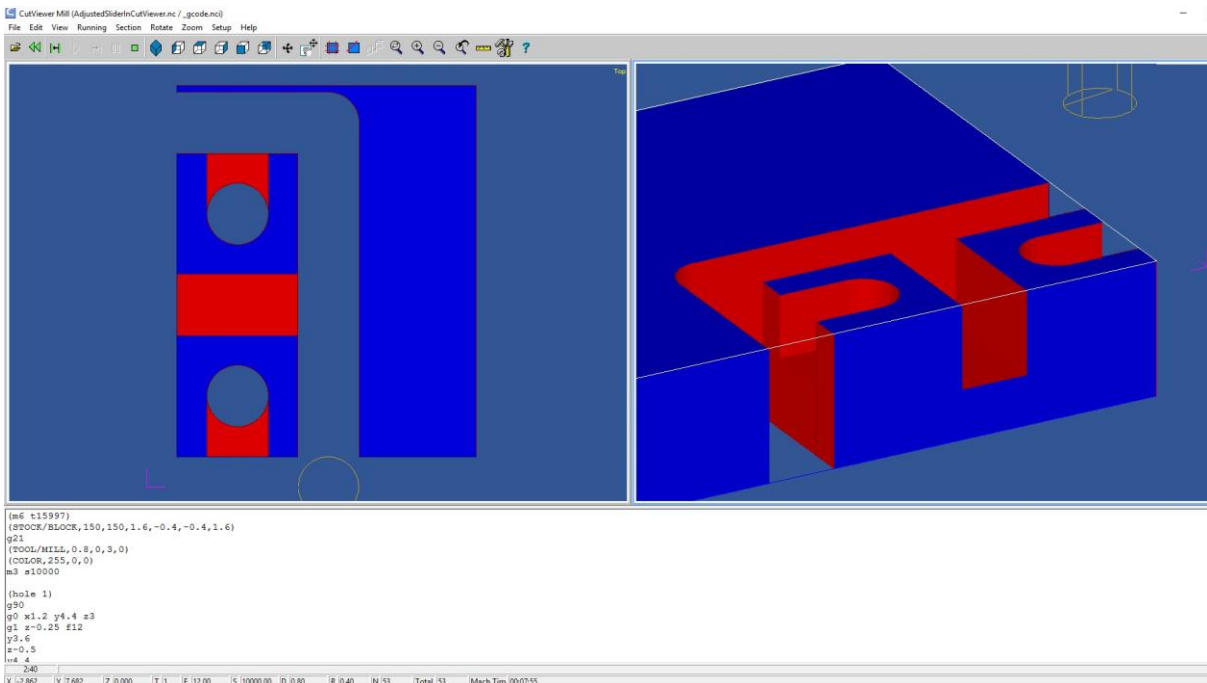


Figure 48: Screenshot of CutViewer Mill (GRZ Software) simulation illustrating the slider as it would be ideally cut by the G-code written for it.

Several pulley arrangements were considered (Fig. 49) for the asymmetric slider. The most compact option (Fig. 49a, which would have a wire end fixed in the centre of a pulley) would require a non-conductive pulley to avoid directing excess current through the wire segment nearest the slider. Since plastic pulleys tended to melt, a separate mounting point for the wire end (Fig. 49b) was more practical. Additional pulleys could be added, as in Fig. 49c, if a longer wire was needed, to satisfy a need for

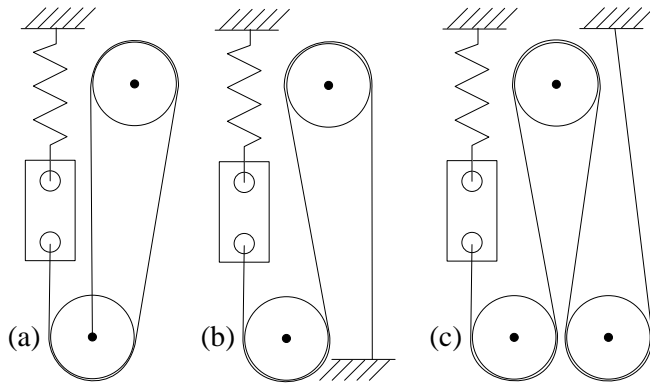


Figure 49: Examples of wire-pulley arrangements considered for one-sided actuation. Voltage is applied between the biasing spring and the ends of the wire. In (a), the ends are fixed to the centre of a pulley, which must be non-conductive. In (b), the ends are fixed separately. (c) Illustrates how more pulleys can be added to accommodate a longer wire.

- greater resistance (perhaps due to lower resistivity from the use of a thicker wire or
- greater displacement capability.

For the first prototype attempt, the latter arrangement was applied. The addition of the spring (provided with BMF-100 wire), the slider and the movable connections between these increased the resistance of the SMA wire circuit by about 15Ω , a large increase given that one straight length of wire (~ 50 mm) had a resistance of approximately 1.8Ω . This (along with a great deal of the safety concerns) could be resolved with a lower-resistance return path such as:

- a conductive wire leading from the SMA wire to the biasing spring,
- a wire leading to a different contact on the board or
- the pulley nearest the wire (this proved simplest).

Lancet-holder design

The aluminum slider allowed the lancet substantial ϕ , and was no longer required for electrical transmission. A new design was needed to combine the greater power of the methods in the previous section with a better slider-lancet interface. The multi-track design, despite its fine features, was still unable to ensure a perfect fit around the driven shank. Alternative designs were considered, which would allow sub-millimetre features to be removed or expanded to reach

millimetre scale. Greatest attention was devoted to attaching a larger part to the lancet, marking a conceptual return to the original e-Mosquito lancet holder (Fig. 1), with a very different interface.

Various means of attachment of lancet and holder were available. The lancet could be inserted into a drilled hole, inserted or merged into a temporarily molten volume of plastic, attached with an adhesive, wrapped around (to the extent that it could be bent without risk of breaking), or fastened. The original used a combination of drilled hole and adhesive. Here, the hole would still need a diameter similar to that of the lancet, but it would be a simple opening and could thus be produced by the CNC router with a sufficiently long (non-cutting) drill bit.

The geometry of the new arrangement also offered diverse options. The holder would need to rotate with the lancet while interacting with whatever proximate component delivered the linear displacement. This component did not have to be a plastic slider; since the holder would be non-conductive, the wire could directly contact the holder if practical. Regardless, a plastic holder would still have to fit within the constraints imposed by in-plane movement between two flat surfaces. To allow rotation, it would require a round feature.

Maximum roundness could be achieved with a plastic ball, the lancet inserted into a hole drilled along the radius (Fig. 50a). However, that would unnecessarily allow rotation in other planes. The preferred outer surface for a rolling holder was thus a cylinder, serving to increase the diameter of the driven part of the L-shaped lancet. It was initially assumed that the holder diameter should be three times the lancet diameter — resulting in 1.2 mm. That would leave plenty of material intact to preserve structural integrity. The hole needed to be deep enough to firmly hold the lancet, yet leave enough uncut material below to prevent the dull end of the lancet from breaking through the far side of the holder.

Two relative orientations of the lancet and cylindrical holder presented themselves.

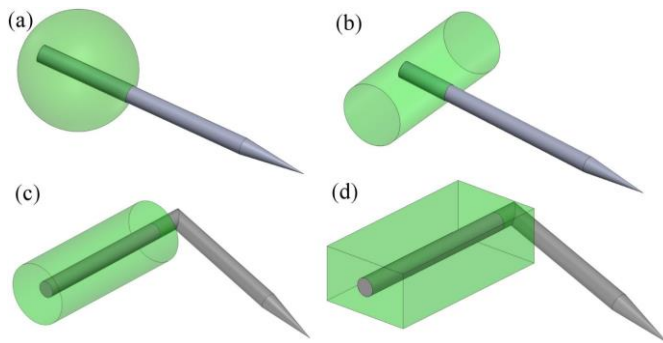


Figure 50: Alternative needle configurations considered to increase the diameter of the part of the lancet interfacing with the reusable part of the system. (a)-(c) are based on fixing the lancet shank inside a rolling solid, while (d) involves allowing the shank to rotate inside a sliding solid.

1. The hole could be drilled along the cylinder of the holder and a straight lancet inserted (Fig. 50b), resembling the (welded) T lancet concept of Fig. 12 if this was done halfway along the length of the cylinder. In that case, the base could have no protruding structures near the channel, as these would interfere with the motion of the holder.
2. An alternative that preserved the L geometry was to insert the driven shank of an L-lancet into the roller along the length of the holder (Fig. 50c). This could be accomplished with a trench along the length of the roller, or a drilled hole along the cylinder axis. The hole would require a substantially longer drill bit, as the L-shaped lancet would need to extend further into the roller to eliminate ϕ_{xz} (see Chapter 3, “In vitro testing”).

These approaches all relied on a 0-DOF connection between holder and lancet. An alternative was to make the holder a permanent, disposable attachment of the lancet, but allow one rotating DOF, so that the holder could translate with the slider and allow the lancet to rotate within it (Fig. 50d). Separation of the sliding and rotating interfaces allowed independent optimization of each, and this concept was adopted. In the resulting design, the holder (Fig. 51) was a milled ABS block with an L-shaped trench for the lancet and a large hole that admitted part of an aluminum slider (Fig. 52). The trench segment running along the narrower side held the shank, and was melted closed once the shank was inserted, providing a tight rotating joint. The other trench segment was shorter than

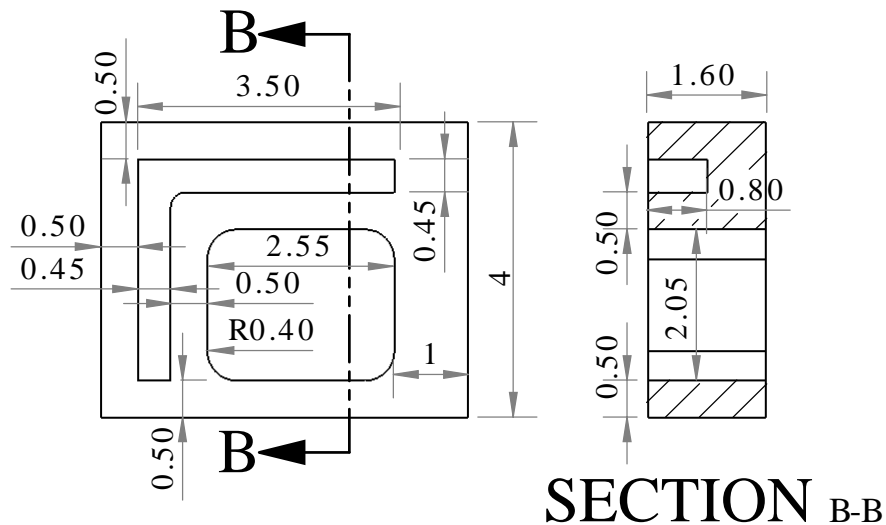


Figure 51: Bottom view of the lancet-holder design based on Fig. 50d. The segment of trench on the left holds the lancet shank, and the top is melted closed after the shank is inserted (the holder was milled from ABS). The segment along the top is shorter than the penetrating lancet arm.

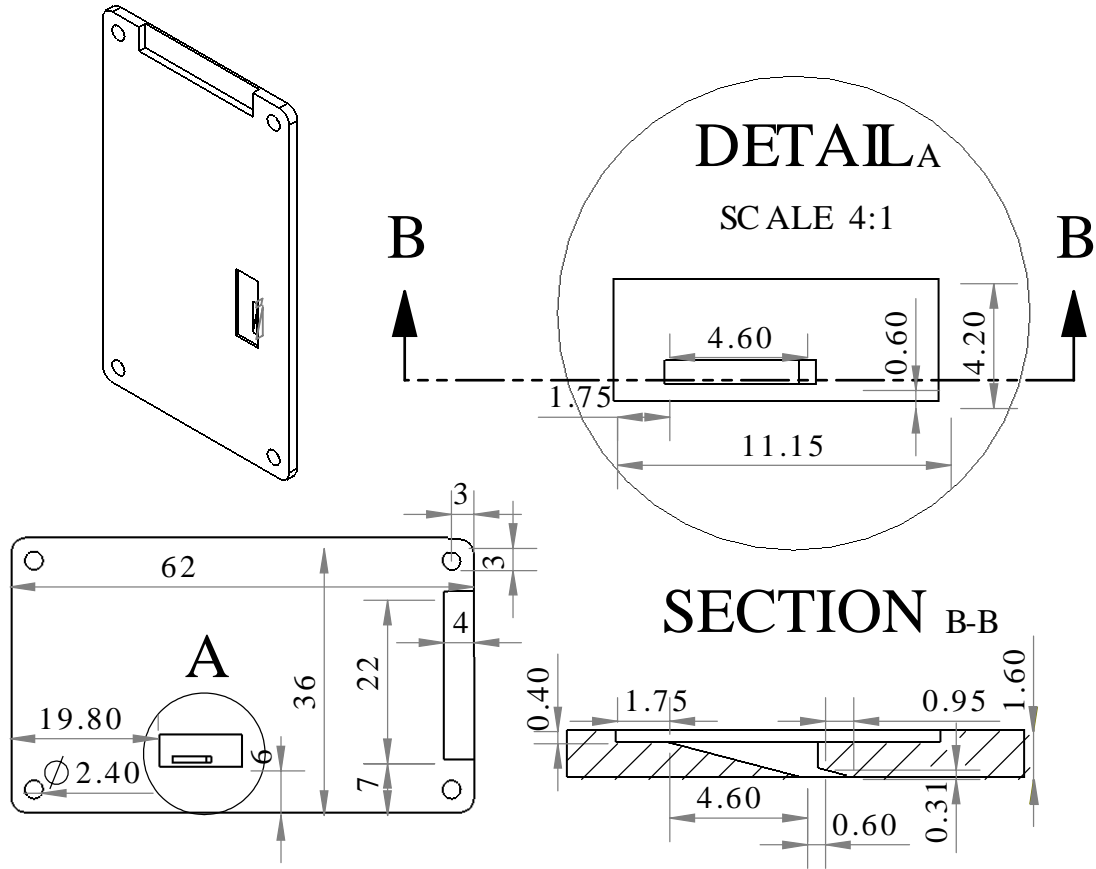


Figure 53: Dimensions of the base design for use with the sliding lancet holder. Section B-B provides an enlarged cross-section through the track and the channel below it.

- Tracks were no longer necessary to prevent the lancet from escaping the slider, as the holder provided a secure connection to each. A single track was used to prevent sideways motion of the slider and lancet.

The holder (Fig. 54) and slider (Fig. 55) were milled and mounted on a minimally milled PCB that ensured only isolation. The parts fit together (Fig. 56), and for the first time, no ϕ was observed when the device was actuated.

When held against the skin and supplied with current, the prototype still failed to draw blood. This time, precision could not be blamed. Close inspection of the lancet-skin interface produced a number of conclusions.

- The lancet was fully extending against the skin of the forearm.
- The lancet tip was contacting the skin at the desired 30–45° angle and decreasing to a θ of approximately 0°.
- The tip may press into the skin surface so as to emerge from it upon removal and leave a visible depression as observed in “In vitro testing” (Chapter 3).
- In spite of this, the tip was not breaking through the stratum corneum; the skin was able to deflect downward by the full length of the lancet, even though the lancet extended as far below the base as the e-Mosquito lancet that drew blood.

The problem clearly lay in the way that the lancet interacted with the skin, rather than in the ability of the device to extend the lancet along a desired path. Tests using unaltered lancets at various angles revealed that diagonal insertion introduced a lateral component to skin deformation. The downward deflection of skin was limited by the resistance to displacement of underlying tissues. However, skin on the forearm slides laterally by distances of even several centimetres, relative to the same tissues. Diagonal insertion allowed the skin to distribute the stress and strain over a larger surface area, allowing the section pressed by the tip to move further relative to the base without rupturing.



Figure 54: Bottom view of the (5-mm-long) milled lancet holder with the lancet inserted. The melted-over trench holding the driven shank is on the left.

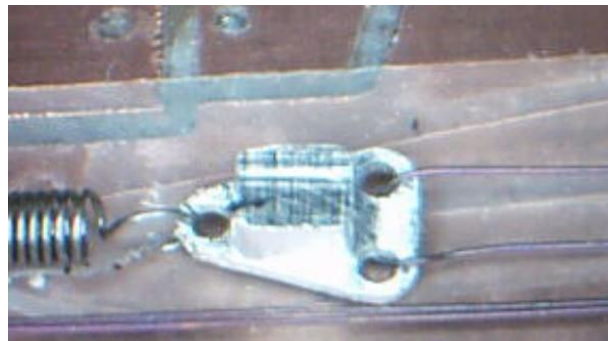


Figure 55: Bottom view of the milled aluminum slider described in Fig. 52, mounted on the PCB. A layer of transparent tape separates the slider from the board.



Figure 56: Bottom view of the lancet holder (Fig. 54) and slider (Fig. 55), assembled.

This provided a potential explanation of the mechanism behind the greater force needed for angled insertion according to [38].

The holder design allowed the lancet to be extended easily, and this was done so that the tip would extend 4 mm below the base. The asymmetric actuator arrangement of Fig. 49c was used to power 300 mm of wire (two halves of 150 mm running in parallel, allowing for 6 mm contraction). While this represented roughly double the capabilities of the rack-holder actuator in terms of displacement, it still barely broke through the skin, and drew little blood. It was concluded that the original hypothesis was false: angled insertion followed by rotation of the lancet did not increase the emerging volume of blood, but instead appeared to decrease it, if any emerged. Three possible explanations were identified.

1. The inefficient diagonal approach caused the lancet to penetrate the skin less deeply than if it had been inserted vertically from the start.
2. The flexibility of the skin may have allowed it to stretch to accommodate small lateral movements of the lancet, so that the wound was not widened.
3. Even if the wound produced in the skin by the lancet rotation had greater volume relative to the lancet, that volume may merely allow blood from nearby capillaries to pool below the skin, not emerging of its own accord through the relatively narrower top section of the wound. In Fig. 45 (which reasonably corresponds to the lancet-base geometry in question), the wound at the ideal (undeflected) skin surface is no wider than the lancet. The path of Fig. 43 would be better for widening of the upper part, provided that a lancet following that path ever penetrated.

Testing of larger sizes concluded that no standard finger-pricking lancet could consistently produce adequate capillary blood from the forearm by mere wounding. Severely increased wounding or external pressure would be required, compromising the safety and practicality of a minimally invasive device. As a result, the e-Mosquito project began to investigate other approaches.

Chapter 5: Alternative approaches

After ending development of the wrist-worn prototype, a number of concepts were investigated in collaboration with Gang Wang. Two are presented here, as they are not expected to be submitted for publication and represent other SMA-based approaches to blood sampling:

- an SMA wires load and release a spring that propels a lancet and
- a wire contracts to compress a finger and hopefully increase the volume of blood extracted by a spring-loaded device.

The general concepts are shared, but the specifics of all the presented designs are individual work.

Spring-loaded actuator

This concept was developed based on the apparent relationship between blood volume and insertion velocity [38]. It was not fully prototyped, so dimensions are omitted.

The functional core of the device consisted of the interaction between a sliding lancet holder and a latch (Fig. 57). These would be housed in a two-part casing (Fig. 58) accommodating matching pegs in the other half (Fig. 59). The casing would also hold:

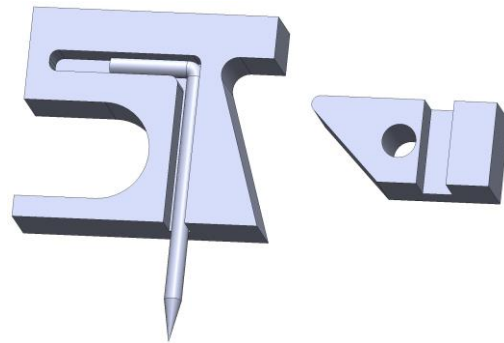


Figure 57: Lancet holder and latch for the spring-loaded actuator. The plastic part of the lancet holder is 5x5 mm. The entire holder trench is melted closed over the lancet (compare Fig. 51).

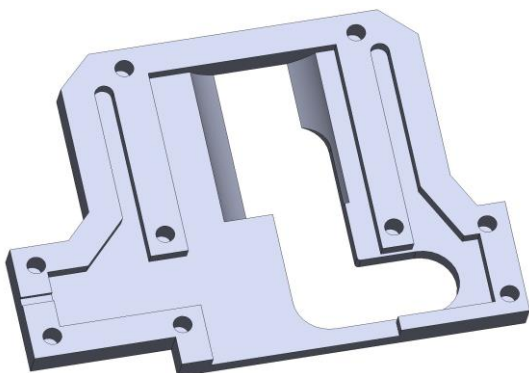


Figure 58: Inside view of the half of the actuator casing with holes.

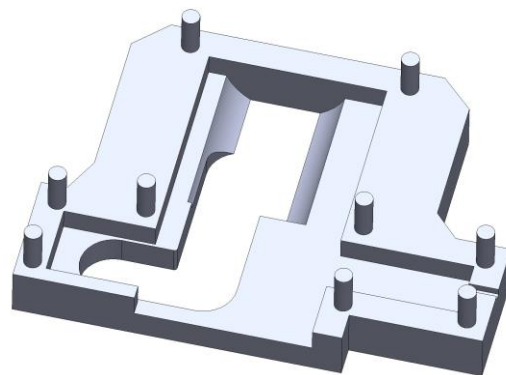


Figure 59: Inside view of the half of the actuator casing with pegs.

- a screw, pulled by SMA wire (hereafter a “tow hook”), that would fit into the large notch in the holder and pull it deeper into the device when the wire contracted;
- a coiled compression spring that would rest between the holder and the backwall, continually pushing the holder outwards;
- two straight lengths of stiff steel wire in trenches on the sides, serving as cantilever springs to push the latch and tow hook towards the centre for interaction with the holder; and
- another SMA wire, to pull the lancet away from the holder, allowing the spring to propel the holder (and lancet) into the skin.

The assembly of these components (apart from the SMA wires and compression spring) is shown in Fig. 60. The planned sequence of operations, represented in Fig. 61 as steps (a)–(i), follows.

1. The lancet holder would be inserted through the bottom of the device (a), pushing the tow hook and latch out of the way (b), the tow hook perhaps pushed to the side manually.
2. When the holder was deep enough, the steel wires would push both the latch and the tow hook into the corresponding indentations in the holder (c).
3. Actuation of the SMA wire wrapped around the tow hook would cause the hook to pull the holder upwards, the inclined plane on the left edge of the holder forcing the latch to the left while the top edge of the holder compressed the coiled spring. This would until the left edge of the holder passed the latch, which would snap to the right and lock below the holder (d).
4. In this state, the device containing the actuator could be worn, and the spring would remain loaded until the SMA wire connected to the latch was triggered, pulling the latch to the left (e).

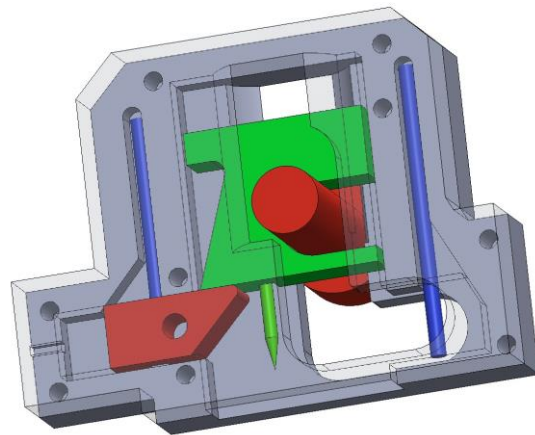


Figure 60: Model of the assembled spring-loaded system, in the loaded position. The lancet and holder are green, the latch and tow hook (screw) are red, the steel wires are blue and the casing is grey. The compression spring pushing the holder down and the SMA wires pulling the latch to the left and the tow hook up are omitted.

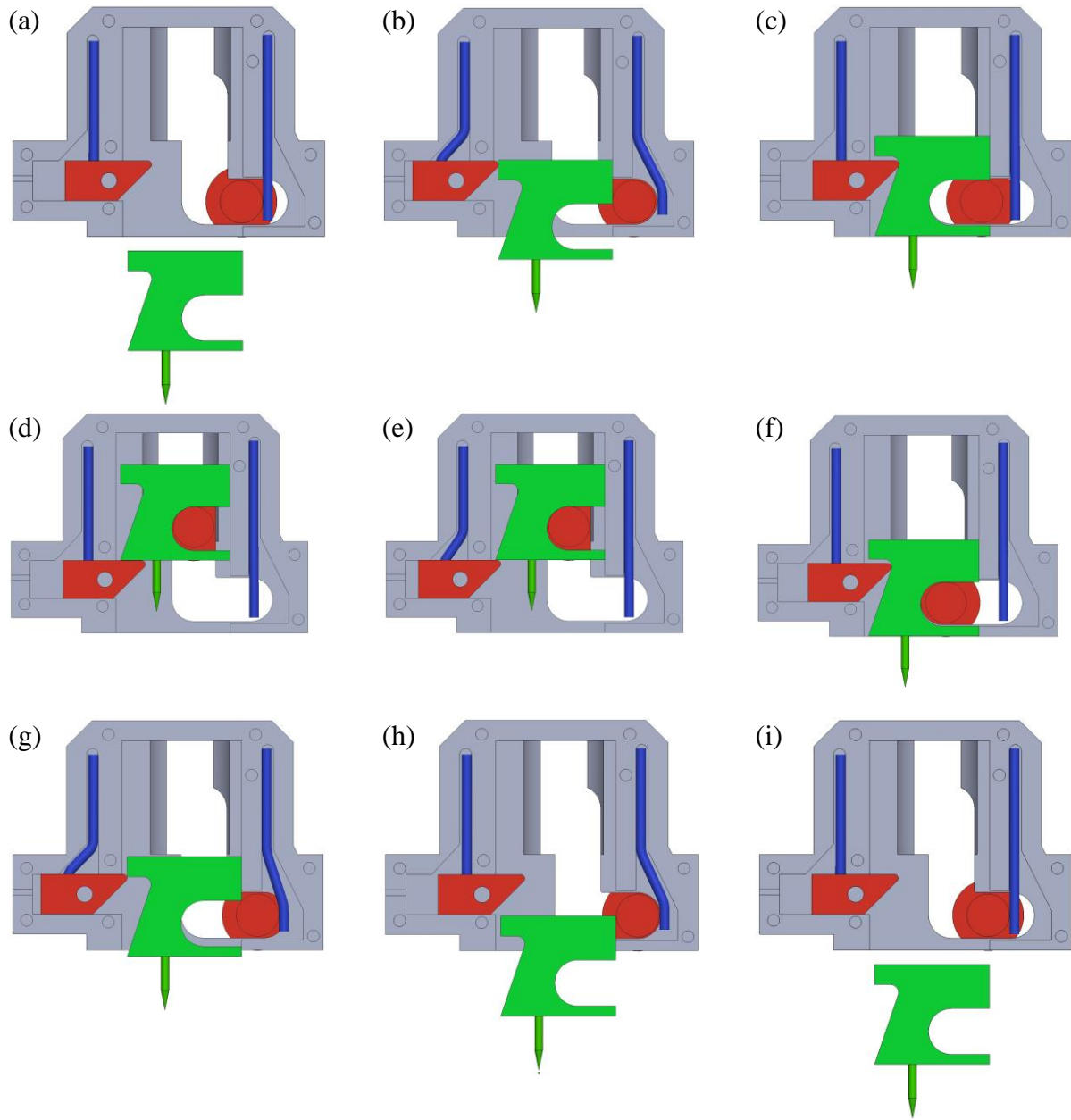


Figure 61: Operation sequence for the spring-loaded concept, corresponding to the assembly in Fig. 60. The sequence consists of lancet holder insertion (a–c), loading (c–d), firing (e–f) and removal (f–i).

5. This would allow the compression spring to extend and accelerate the holder downwards until the spring hit the lower edge of the rounded space provided to it. The lancet would continue downwards into the skin until the holder ran out of driving force and momentum, or until the tow hook reached the bend in its track. Cooling of the SMA wire would allow the latch to also block further downwards movement (f).

6. The loading process (c–d) could then be repeated to retract the lancet, or from this same position, the lancet could be removed by the user by actuating the latch and manually pulling the tow hook aside (g) until the holder was sufficiently extended (h). It could then be freed easily (i).

While a lancet holder was milled from ABS to demonstrate manufacturability (Fig. 62), the concept was not developed further. This was due to:

- the observation that no existing spring-loaded lancet appeared capable of consistently drawing substantial blood from the forearm and
- concern that the relevant intellectual property space (spring-loaded SMA mechanisms) was already crowded.



Figure 62: Physical implementation of the lancet holder of Fig. 57 for the spring-loaded actuator concept. Trench melting was difficult at this scale, but the resulting lancet fixture was firm.

Emphasis was instead placed on automatically drawing blood from the finger.

Finger compressor for blood sampler

Following realization of the impracticality of standard forearm lancing, prototypes were jointly made to test whether blood volume could be increased by applying positive pressure to the skin surrounding a wound. It was known from prior experience that a pneumatic balloon could substantially increase blood flow from a finger wound. As pneumatic squeezing for this purpose was considered insufficiently innovative to serve as defensible intellectual property for a medical product, it was investigated whether a similar effect might be achieved with a device driven by SMA wire. This would require substantial force and greater power, due to the low efficiency of SMA actuation.

To compress the finger using SMA wire, a means of shielding the finger from heat and electricity was required. While the high current through the wire would not be replicated in the finger due to the much greater resistance of the skin, above the transition temperature ($A_s = 70\text{ }^\circ\text{C}$), the uncoated metal could be expected to cause burns within 1 s of contact [91].

Besides providing reliable thermal and electrical isolation, the shielding must also:

- withstand the heat of the SMA wire, which might reach 100 °C, without igniting, melting or visibly degrading;
- withstand any forces exerted on it by the wire and the finger;
- transmit to the finger as much as possible of the pressure resulting from wire contraction;
- not overly increase the outer volume of the final part;
- be comfortable and non-toxic for brief contact (up to two minutes); and
- allow effective cleaning of skin-contacting surfaces.

A plastic shielding would remain safe to touch for several seconds at a temperature up to 85 °C [91] and should heat slowly enough slowly enough to negate the burn hazard for the expected duration of continuous wire heating. Extended consideration of heat resistance was obviated thanks to a modification of parallel current actuation (Chapter 4, “Parallel and asymmetric wire actuation”): points in the wire on either side of the finger could be grounded so that no current would flow between them. The role of the shielding was reduced to one of backup protection and comfort.

A base was designed (Fig. 63) with a large hole in the centre, against which a finger could be pressed and through which a button-triggered lancet (or perhaps a descendant of the spring-loaded design in the previous section) could be inserted to prick the finger. Holes around the outside would admit screws, around which SMA wire could be wrapped and which could also serve to attach a cover for the prototype. The base was milled from 3-mm-thick PMMA and assembled as shown in Fig. 64. The wire arrangement shown sought to maximize wire length and avoid any crossings that could short-circuit the wire. The wire was

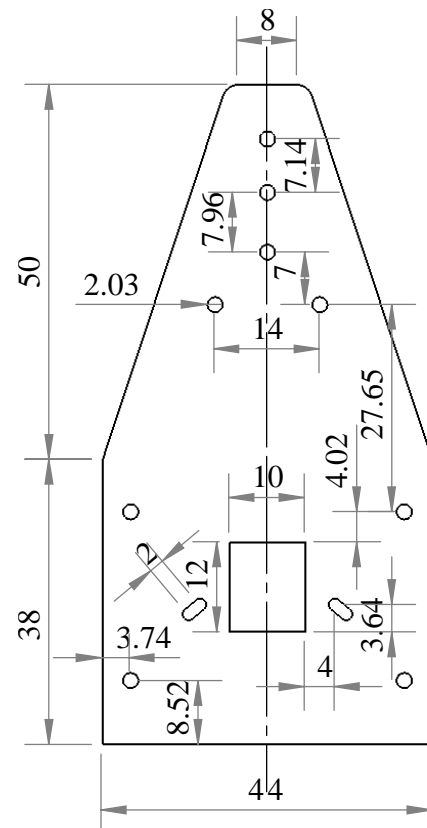


Figure 63: Dimensions of the base for the finger compressor. There is a wide range of possible thicknesses.

located on the bottom side of the base, crossing to the top side only to pass around the shielding (an ABS rectangle with two holes). Supplying 3.7V between the screw at the narrow end of the base and the wire connecting the two screws at the wide end caused the shielding to be pulled downwards and deliver perceptible pressure to the finger. As expected, no heating of the section of wire between the two grounded screws was observed.

Though it behaved as intended, the prototype demonstrated weaknesses of SMA actuation. The 17 cm of wire on each side of the base provided approximately 7 mm of downward movement. This was enough to firmly compress a finger that barely fit under the shielding when the wire was relaxed. A practical version would:

- require twice that length of wire to compress a finger as inserted by a casual user over a suitable distance;
- yet still only be suitable for a particular hand size;
- draw several amperes, an order of magnitude more than a pneumatic pump;
- yet still be weak compared to pneumatic compression.

The solution was deemed impractical for a wearable design.



Figure 64: Bottom view of the PMMA wire base for the finger compressor, with SMA wire wrapped around the screws. Voltage was applied between the steel wire at the bottom of the image (ground) and the screw at the top. The black ABS in the middle serves as shielding.

Chapter 6: Directions for future research

This research centred on the design of multiple electromechanical actuators driven by contracting wires made of shape memory alloy (SMA), all in pursuit of reliable blood extraction for the purposes of the e-Mosquito autonomous, wearable blood glucose monitoring project. The primary focus involved the refinement of compact methods for extending a lancet needle into skin at an initially shallow but increasing angle, with the goal of widening the resulting wound in order to reliably draw blood sufficient for self-monitoring of blood glucose by people with diabetes.

My initial design and testing (Chapter 3) of a minimal, 3D-printed prototype for angled lancet insertion demonstrated that a maximally flat, skin-pricking actuator system could be implemented at low cost and with a small number of parts. The work was presented at the 2016 IEEE Sensors conference [72] and was the subject of a provisional US patent application for the concept of using any of a variety of channel geometries to control the path and angle of a skin-penetrating instrument inserted [87].

The subsequent refinement and repeated redesign of the main actuator (Chapter 4) was an interplay between miniaturization and design for manufacturability, each concept (summarized in Table 5) seeking greater control of the extension of the lancet. As more sophisticated manufacturing

Table 5: Summary of refinement designs discussed in Chapter 4.

Design	Novelty	Conclusion
Integration	<ul style="list-style-type: none"> • First e-Mosquito-compatible implementation of the channel concept • Use of press-fit components for assembly of a tighter channel 	Press-fits prevented lancet from escaping but were difficult to match, and produced a gap in which the lancet regularly wedged.
Multi-track	Multiple parallel tracks to more securely move lancet shank in plane	Lancet extended by pressing dull sides against skin.
Channel optimization	Analysis of the effect of channel geometry on piercing vs. cutting motion of extending lancet	Height of rotation ledge above the skin should be reduced to privilege piercing.
Parallel-current	Electrically parallel, mechanically serial configuration of SMA wire	Length of wire suppliable by Li-ion battery greatly increased.
Asymmetric actuation	<ul style="list-style-type: none"> • Both halves of wire share the same pulleys • Current returned through slider and spring 	Achievable density of wire routing doubled.
Lancet holder	<ul style="list-style-type: none"> • Lancet rotates inside a disposable holder • Holder interfaces with metal slider 	ϕ was reduced and the lancet extended as desired.

techniques were developed, prototype quality improved until the device functioned exactly as expected, with full extension of the lancet against the skin. At this point, it was discovered that the primary obstacle lay not within the device but outside it, in the dynamic, elastic behaviour of the skin. Even when a lancet was extended further than in the original e-Mosquito design, emergence of blood was sporadic and insufficient, representing non improvement over the original e-Mosquito actuator. I concluded that no safe wound in the forearm, producible with a simple piercing or cutting motion such as might realistically be used by the e-Mosquito, could be expected to produce adequate blood without external stimulation.

As a result, the wrist-worn e-Mosquito design was abandoned in favour of radically different approaches to autonomous extraction of capillary blood, using higher-circulation areas of the body and/or external stimulation via positive pressure. Early work in this area involved

- a concept for a spring-loaded actuator for propelling disposable lancets into the skin and
- a prototype for pressing a finger against an opening with a shield driven by SMA wire, with the goal of increasing the volume of blood emerging when the finger was pricked with a lancet inserted through the opening.

Neither was deemed practical; other methods of increasing blood volume through compression remain under investigation.

Although there were no publications on the later portion of this research, given the paramount importance of drawing blood and the inability of any system to reliably do so once *in vivo* testing became possible, a variety of new designs and techniques were produced throughout the research.

Novel ideas discussed in this thesis include:

- the use of and challenges associated with T- and especially L-shaped lancet needles;
- the use of fixed and moving part geometry to enforce rotation of such lancets in conjunction with their translation;
- the creation of very flat systems that could be used to provide skin penetration for a variety of wearable applications, enabling a greater variety of autonomous devices to relieve their wearers of the burden of attention;
- simulation of the paths followed by and degrees of freedom affecting lancets subjected to sliding rotation using simplified models of such geometry;

- methods of employing hobby-grade rapid prototyping systems to produce parts with multiple features at the limits of resolution of said systems;
- the use of electrically parallel, mechanically serial SMA circuits, which can be powered with low-voltage, high-current batteries compact enough for wearable devices; and
- a potential mechanism behind the greater insertion force required for angled needle entry (identified in [38]), along with aforementioned conclusions about the viability of attempting to draw capillary blood from thick-skinned, moderate-circulation sites such as the forearm.

These topics and other observations that could not be properly explored during the research point to numerous directions of potential future research.

1. Other test sites may prove more susceptible to piercing or may bleed more freely, and adapted versions of any of the designs discussed here may meet with greater success there, though likely not painlessly. Areas of potential interest include the ankles, ears, and various points on the hands.
2. Alternatively, it may be possible to harness the natural motion of the body at bending joints (e.g., inner side of the elbow) or colliding surfaces (e.g., the underside of the foot) to provide extra force to drive a needle into one of these sites.
3. Given sufficient power and displacement, it may be possible to use the actuator to reach larger blood vessels. This would allow easier blood sampling, but not without risks that made the product unsafe for consumer use.
4. The possibility of using a cutting blade as opposed to a piercing tip was briefly mentioned, but this was never attempted. While a simple lancet cut need not bleed sufficiently, it remains possible that a rotating blade could achieve the result given a sufficiently violent actuator.
5. In the same vein, more complex needle/blade geometries are possible, including curved or greatly widening instruments. These are less easily available but certainly possible to manufacture.
6. Since the e-Mosquito was meant to extract blood for automation of the finger-stick test in diabetes, and relied on (solid) lancet needles, all attempted extraction relied on passive bleeding or bleeding assisted by positive pressure applied to skin near the wound. Given a sufficiently compact means of producing negative pressure, a hollow needle may be able to

extract blood where passive solid ones would fail. The viability of using hollow needles and microfluidics with these actuators was not investigated.

7. Similarly, the need to produce a bleeding wound may be eliminated by integrating a sufficiently low-cost sensor into the needle (lancet or otherwise), e.g. by coating it with GOx. Concern would then center on encountering adequate capillary blood within the skin and ensuring measurement quality.
8. SMA actuators are extremely inefficient, dispersing the majority of supplied energy as heat. In this research, emphasis was placed on shielding the body from both thermal and electrical currents. No e-Mosquito design has sought to harness heat as a means of increasing local blood flow (and reducing wire cooling time). The main requirement would be to use a thermally conductive material otherwise meeting the requirements for thermal shielding discussed in Chapter 6 — “Finger compressor for blood sampler”.
9. Kinematically, the sliding-rotating motion investigated here can produce a vertical, point-first extension of a length substantially exceeding the thickness within which it is stored. Although this research focused entirely on wearable medical monitoring technology, there may exist analogous applications where one of the actuation concepts disclosed here may be applied more productively.
10. Parallel-current actuation may be useful in applications beyond wearable technology, wherever electromechanical circuits using SMAs or EAPs must produce large displacements using limited voltages, but have substantial current available.

This is a short listing, and the reader can likely produce many concepts of their own, both for new applications and in pursuit of the goal of putting fully autonomous glucose monitoring wearables in the hands of people with diabetes.

Bibliography

- [1]. NCD Risk Factor Collaboration, “Worldwide trends in diabetes since 1980: a pooled analysis of 751 population-based studies with 4.4 million participants,” *Lancet*, vol. 387, no. 10027, pp. 1513–1530, 2016.
- [2]. American Diabetes Association, “Standards of medical care in diabetes - 2012,” *Diabetes Care*, vol. 35, no. SUPPL. 1, pp. S11-63, 2012.
- [3]. D. Daneman, M. Jones, A. Swerdlow, A. Burden, W. Gatling, and A. Krolewski, “Type 1 diabetes,” *Lancet (London, England)*, vol. 367, no. 9513, pp. 847–58, 2006.
- [4]. P. Zimmet, T. Tuomi, I. R. Mackay, M. J. Rowley, W. Knowles, M. Cohen, and D. A. Lang, “Latent Autoimmune Diabetes Mellitus in Adults (LADA): the Role of Antibodies to Glutamic Acid Decarboxylase in Diagnosis and Prediction of Insulin Dependency,” *Diabet. Med.*, vol. 11, no. 3, pp. 299–303, 1994.
- [5]. M. Landin-Olsson, “Latent autoimmune diabetes in adults,” *Ann. N. Y. Acad. Sci.*, vol. 958, no. 1, pp. 112–116, Jan. 2006.
- [6]. J. Wagner, C. Malchoff, and G. Abbott, “Invasiveness as a barrier to self-monitoring of blood glucose in diabetes,” *Diabetes Technol. Ther.*, vol. 7, no. 4, pp. 612–619, 2005.
- [7]. S. Il Yum and J. Roe, “Capillary blood sampling for self-monitoring of blood glucose,” *Diabetes Technol. Ther.*, vol. 1, no. 1, pp. 29–37, 1999.
- [8]. A. Heller and B. Feldman, “Electrochemical glucose sensors and their applications in diabetes management,” *Chem. Rev.*, vol. 108, no. 7, pp. 2482–2505, 2008.
- [9]. J. Bandodkar and J. Wang, “Non-invasive wearable electrochemical sensors: a review,” *Trends Biotechnol.*, vol. 32, no. 7, pp. 363–371, 2014.
- [10]. J. L. Smith, *The Pursuit of Noninvasive Glucose: “Hunting the Deceitful Turkey.”* 2015.
- [11]. C.-F. So, K.-S. Choi, T. K. Wong, and J. W. Chung, “Recent advances in noninvasive glucose monitoring,” *Med. Devices (Auckl.)*, vol. 5, pp. 45–52, 2012.
- [12]. U.S. Food and Drug Administration, “Self-monitoring blood glucose test systems for over-the-counter use: guidance for industry and Food and Drug Administration staff,” 2016.

- [13]. D. Rodbard, "Continuous Glucose Monitoring: A Review of Successes, Challenges, and Opportunities," *Diabetes Technol. Ther.*, vol. 18, no. S2, pp. S2-3-S2-13, 2016.
- [14]. R. A. Lal and D. M. Maahs, "Clinical use of continuous glucose monitoring in pediatrics," *Diabetes Technol. Ther.*, vol. 19, no. S2, p. S-37-S-43, 2017.
- [15]. S. Finfer, J. Wernerman, J.-C. C. Preiser, T. Cass, T. Desai, R. Hovorka, J. I. Joseph, M. Kosiborod, J. Krinsley, I. Mackenzie, D. Mesotten, M. J. Schultz, M. G. Scott, R. Slingerland, G. den Berghe, and T. Van Herpe, "Clinical review: Consensus recommendations on measurement of blood glucose and reporting glycemic control in critically ill adults.," *Crit. care*, vol. 17, no. 3, p. 229+, 2013.
- [16]. G. McGarraugh, D. Price, S. Schwartz, and R. Weinstein, "Physiological influences on off-finger glucose testing," *Diabetes Technol. Ther.*, vol. 3, no. 3, pp. 367–376, 2001.
- [17]. S. Faccioli, S. Del Favero, R. Visentin, R. Bonfanti, D. Iafusco, I. Rabbone, M. Marigliano, R. Schiaffini, D. Bruttomesso, and C. Cobelli, "Accuracy of a CGM sensor in pediatric subjects with type 1 diabetes. Comparison of three insertion sites: arm, abdomen, and gluteus," *J. Diabetes Sci. Technol.*, vol. 0, no. 0, pp. 1–8, 2017.
- [18]. J. P. Lock, E. Z. Szuts, K. J. Malomo, and A. Anagnostopoulos, "Whole-blood glucose testing at alternate sites: Glucose values and hematocrit of capillary blood drawn from fingertip and forearm," *Diabetes Care*, vol. 25, no. 2, pp. 337–341, 2002.
- [19]. K. A. Pasyk, S. V. Thomas, C. A. Hassett, G. W. Cherry, and R. Faller, "Regional differences in capillary density," *Plast. Reconstr. Surg.*, vol. 83, no. 6, pp. 939–945, 1989.
- [20]. L. Heineman and D. Boecker, "Lancing: quo vadis?," *J. Diabetes Sci. Technol.*, vol. 5, no. 4, pp. 966–981, 2011.
- [21]. K. Shike and V. Coffey, "Capillary blood collection via finger prick , Bond University." Bond University, Robina, pp. 1–13, 2017.
- [22]. G. E. Gattiker, K. V. I. S. Kaler, and M. P. Mintchev, "Electronic mosquito: designing a semi-invasive microsystem for blood sampling, analysis and drug delivery applications," *Microsyst. Technol.*, vol. 12, no. 1–2, pp. 44–51, 2005.
- [23]. G. E. Gattiker, "Designing a BioMEMS-based blood sampler," University of Calgary, 2006.

- [24]. G. Wang and M. P. Mintchev, "Development of wearable semi-invasive blood sampling devices for continuous glucose monitoring: A survey," *Engineering*, vol. 5, no. 5, pp. 42–46, 2013.
- [25]. G. Wang, M. D. Poscente, S. S. Park, O. Yadid-Pecht, and M. P. Mintchev, "Characterization of a cuff-based shape memory alloy (SMA) actuator," *Inf. Theor. Appl.*, vol. 22, no. 1, pp. 3–20, 2015.
- [26]. G. Wang, M. D. Poscente, S. Park, O. Yadid-Pecht, and M. Mintchev, "Autonomous shape memory alloy (SMA) based actuator reaching subcutaneous blood capillaries: results from in-vitro characterization and two pilot human studies." Diabetes Technology Society, Bethesda, MD, 2015.
- [27]. G. Wang, M. D. Poscente, S. S. Park, C. N. Andrews, O. Yadid-Pecht, and M. P. Mintchev, "Minimally Invasive Pseudo-continuous Blood Glucose Monitoring: Results from In-Vitro and In- Vivo Testing of the e-Mosquito," in *2016 IEEE International Symposium on Circuits and Systems*, 2016, pp. 321–324.
- [28]. J. A. McGrath, R. A. J. Eady, and F. M. Pope, "Anatomy and organization of human skin" in *Rook's Textbook of Dermatology*, 8th ed. Hoboken, NJ, USA, Wiley-Blackwell, 2010.
- [29]. W. S. Snyder, M. J. Cook, E. S. Nasset, et al., "Report of the task group on reference man". in: *Report Prepared for International Commission on Radiological Protection*, no. 23. Oxford: Pergamon Press, 1974, pp. 46–57.
- [30]. H. Gray, H. V. Carter, *Anatomy of the Human Body*, 20th ed. W. H. Lewis, Ed. Philadelphia, PA, USA: Lea and Febiger, 1918, plate 942.
- [31]. K. Tsuchiya, N. Nakanishi, Y. Uetsuji, and E. Nakamachi, "Development of blood extraction system for health monitoring system," *Biomed. Microdevices*, vol. 7, no. 4, pp. 347–353, 2005.
- [32]. J. McGuire, J. R. Sorrells, and J. D. Moore, "Resistance of human skin to puncture and laceration," 1973.
- [33]. A. N. Annaidh, K. Bruyère, M. Destrade, M. D. Gilchrist, and M. Otténio, "Characterization of the anisotropic mechanical properties of excised human skin," *J. Mech. Behav. Biomed. Mater.*, vol. 5, no. 1, pp. 139–148, 2012.

- [34]. J. van Gerwen, J. Dankelman, and J. J. van den Dobbelsteen, "Needle-tissue interaction forces - A survey of experimental data," *Med. Eng. Phys.*, vol. 34, no. 6, pp. 665–680, 2012.
- [35]. O. A. Shergold and N. A. Fleck, "Mechanisms of deep penetration of soft solids, with application to the injection and wounding of skin," *Proc. R. Soc. A Math. Phys. Eng. Sci.*, vol. 460, no. 2050, pp. 3037–3058, 2004.
- [36]. W. Li, B. Belmont, L. Jing, and A. Shih, "Investigation of needle bevel face up and down orientation on pediatric intravenous access," in *IWMF2014*, 2014, pp. 66–71.
- [37]. M. C. Lewis, J. P. Lafferty, M. S. Sacks, V. S. Pallares, and M. TerRiet, "How much work is required to puncture dura with Tuohy needles?," *Br. J. Anaesth.*, vol. 85, no. 2, pp. 238–241, 2000.
- [38]. X. Bao, W. Li, M. Lu, and Z. R. Zhou, "Experiment study on puncture force between MIS suture needle and soft tissue," *Biosurface and Biotribology*, vol. 2, no. 2, pp. 49–58, 2016.
- [39]. X. Q. Kong and C. W. Wu, "Measurement and prediction of insertion force for the mosquito fascicle penetrating into human skin," *J. Bionic Eng.*, vol. 6, no. 2, pp. 143–152, 2009.
- [40]. M. K. Ramasubramanian, O. M. Barham, and V. Swaminathan, "Mechanics of a mosquito bite with applications to microneedle design.," *Bioinspir. Biomim.*, vol. 3, no. 4, p. 46001, 2008.
- [41]. J. W. Y. Jor, M. D. Parker, A. J. Taberner, M. P. Nash, and P. M. F. Nielsen, "Computational and experimental characterization of skin mechanics: Identifying current challenges and future directions," *Wiley Interdiscip. Rev. Syst. Biol. Med.*, vol. 5, no. 5, pp. 539–556, 2013.
- [42]. J. S. Kochhar, T. C. Quek, W. J. Soon, J. Choi, S. Zou, and L. Kang, "Effect of Microneedle Geometry and Supporting Substrate on Microneedle Array Penetration into Skin," *J. Pharm. Sci.*, vol. 102, no. 11, pp. 4100–4108, 2013.
- [43]. H. S. Gill and M. R. Prausnitz, "Does needle size matter?," *J. diabetes Sci. Technol.*, vol. 1, no. 5, pp. 725–729, 2007.

- [44]. L. Palma, L. T. Marques, J. Bujan, and L. M. Rodrigues, “Dietary water affects human skin hydration and biomechanics,” *Clin. Cosmet. Investig. Dermatol.*, vol. 8, pp. 413–421, 2015.
- [45]. L. Overgaard Olsen and G. B. Jemec, “The influence of water, glycerin, paraffin oil and ethanol on skin mechanics,” *Acta Derm. Venereol.*, vol. 73, no. 6, p. 404–406, Dec. 1993.
- [46]. H. Fruhstorfer, G. Schmelzeisen-Redeker, and T. Weiss, “Capillary blood sampling: relation between lancet diameter, lancing pain and blood volume,” *Eur. J. Pain*, no. 3, pp. 283–286, 1999.
- [47]. D. Cunningham, T. P. Henning, E. B. Shain, D. F. Young, J. Hannig, E. Barua, and R. C. Lee, “Blood extraction from lancet wounds using vacuum combined with skin stretching,” *J Appl Physiol*, vol. 92, no. 3, pp. 1089–1096, 2002.
- [48]. H. Fruhstorfer and T. Muller, “Capillary blood sampling: how much pain is necessary?,” *Pract. Diabetes Int.*, vol. 12, no. 2, pp. 72–74, 1995.
- [49]. H. Egekvist, P. Bjerring, and L. Arendt-Nielsen, “Pain and mechanical injury following needle insertions of human skin,” *Eur. J. Pain*, vol. 3, pp. 41–49, 1999.
- [50]. H. Fruhstorfer, “Capillary blood sampling: the pain of single-use lancing devices,” *Eur. J. Pain*, no. 4, pp. 301–305, 2000.
- [51]. J. E. Huber, N. A. Fleck, and M. F. Ashby, “The selection of mechanical actuators based on performance indices,” *Proc. R. Soc. London A*, vol. 453, pp. 2185–2205, 1997.
- [52]. V. O. Del Cura, F. L. Cunha, M. L. Aguiar, and A. Cliquet, “Study of the different types of actuators and mechanisms for upper limb prostheses,” *Artif. Organs*, vol. 27, no. 6, pp. 507–516, 2003.
- [53]. Precision Microdrives, “Nano Coreless 3mm DC Motor - 8 mm Type, Model 103-100.” Precision Microdrives, London, pp. 1–5, 2015.
- [54]. J. Bell, T. J. Lu, N. A. Fleck, and S. M. Spearing, “MEMS actuators and sensors: observations on their performance and selection for purpose,” *J. Micromechanics Microengineering*, vol. 15, no. 7, pp. S153–S164, 2005.
- [55]. Y. Bar-Cohen, *Electroactive polymer (EAP) actuators as artificial muscles: reality, potential, and challenges*, 2nd ed. Bellingham, WA: SPIE Press, 2004.

- [56]. M. Irie, T. Maki, K. Melton, S. Miyazaki, I. Ohkata, K. Otsuka, T. Saburi, R. Stalmans, Y. Suzuki, T. Tadaki, K. Uchino, J. van Humbeeck, and C. M. Wayman, *Shape memory materials*. Cambridge, UK: Cambridge University Press, 1999.
- [57]. J. Xu and J. Song, “Thermal responsive shape memory polymers for biomedical applications,” in *Biomedical engineering - frontiers and challenges*, R. Fazel, Ed. Rijeka, Croatia: InTech, 2011, pp. 125–142.
- [58]. J. J. Song, H. H. Chang, and H. E. Naguib, “Biocompatible shape memory polymer actuators with high force capabilities,” *Eur. Polym. J.*, vol. 67, pp. 186–198, 2015.
- [59]. B. Konh, M. Honarvar, and P. Hutapea, “Design optimization study of a shape memory alloy active needle for biomedical applications,” *Med. Eng. Phys.*, vol. 37, no. 5, pp. 469–477, 2015.
- [60]. M. A. Thrasher, A. R. Shahin, P. H. Meckl, and J. D. Jones, “Efficiency analysis of shape memory alloy actuators,” *Smart Mater. Struct.*, vol. 3, no. 2, pp. 226–234, 1993.
- [61]. J. Uchil, K. P. Mohanchandra, K. K. Mahesh, and K. G. Kumara, “Thermal and electrical characterization of R-phase dependence on heat-treat temperature in Nitinol,” *Phys. B*, vol. 253, no. 1–2, pp. 83–89, 1998.
- [62]. K. Otsuka and X. Ren, “Physical metallurgy of Ti–Ni-based shape memory alloys,” *Prog. Mater. Sci.*, vol. 50, no. 5, pp. 511–678, 2005.
- [63]. Dynalloy Inc., “Technical characteristics of Flexinol actuator wires.” Irvine, CA, USA, pp. 1–12, 2014.
- [64]. Toki Corporation, “Artificial metal-based muscle BioMetal fiber.” Tokyo, pp. 1–2, 2010.
- [65]. V. Antonucci, G. Faiella, M. Giordano, F. Mennella, and L. Nicolais, “Electrical resistivity study and characterization during NiTi phase transformations,” *Thermochim. Acta*, vol. 462, no. 1–2, pp. 64–69, 2007.
- [66]. P. Robert, “Drive apparatus,” US 5685148 A1995.
- [67]. C. J. Corris and D. K. Dyess, “Shape memory alloy wire actuator,” US 6374608 B12001.
- [68]. R. MacGregor, “Shape memory alloy actuators and control methods,” US 20040261411 A12003.
- [69]. M. Mernøe, “Shape memory alloy actuator,” US6851260B22003.

- [70]. P. E. von Behrens and D. M. Fairbanks, “High stroke, highly integrated SMA actuators,” US7017345B22003.
- [71]. D. Reynaerts and H. Van Brussel, “Design aspects of shape memory actuators,” *Mechatronics*, vol. 4, no. 8, pp. 1799–1802, 1993.
- [72]. M. J. Berka, O. Yadid-Pecht, and M. P. Mintchev, “MEMS actuator for splinter-like skin penetration in glucose-sensing applications: design and demonstration,” in *IEEE Sensors*, 2016, pp. 1–3.
- [73]. M. Braverman, “The cutaneous microcirculation: ultrastructure and microanatomical organization,” *Microcirculation*, vol. 4, no. 3, pp. 329–340, 1997.
- [74]. Y. Ramot, M. Haim-Zada, A. J. Domb, and A. Nyska, “Biocompatibility and safety of PLA and its copolymers,” *Adv. Drug Deliv. Rev.*, vol. 107, pp. 153–162, 2016.
- [75]. W. Benz, D. E. Nerland, W. M. Pierce, and C. Babiuk, “Acute acrylonitrile toxicity: Studies on the mechanism of the antidotal effect of d- and l-cysteine and their N-acetyl derivatives in the rat,” *Toxicol. Appl. Pharmacol.*, vol. 102, no. 1, pp. 142–150, 1990.
- [76]. R. L. Melnick and J. Huff, “1,3-Butadiene: Toxicity and Carcinogenicity in Laboratory Animals and in Humans,” in *Reviews of Environmental Contamination and Toxicology: Continuation of Residue Reviews*, G. W. Ware, Ed. New York, NY: Springer New York, 1992, pp. 111–144.
- [77]. J. A. Bond and H. M. Bolt, “Review of The Toxicology of Styrene,” *CRC Crit. Rev. Toxicol.*, vol. 19, no. 3, pp. 227–249, 1989.
- [78]. MakerBot, “Replicator 2X User Manual.” MakerBot, Rochester, p. 8. 62-109, 2013.
- [79]. D. Braam, “Cura.” Ultimaker, Geldermalsen, The Netherlands, 2016.
- [80]. MakerBot Industries LLC, “MakerBot Desktop.” MakerBot Industries, LLC, New York, NY, 2016.
- [81]. MatterHackers Inc., “MatterControl.” MatterHackers, Foothill Ranch, CA, USA, 2015.
- [82]. Z. Hoeken, M. Kintel, A. Mayer, and M. Mets, “ReplicatorG.” 2012.
- [83]. J. West and G. Kuk, “The Complementarity of Openness: How MakerBot Leveraged Thingiverse in 3D Printing,” *Technol. Forecast. Soc. Chang.*, vol. 102, no. Jan. 2016, pp. 169–181, 2016.
- [84]. H. Thomas, “GPX.” GitHub, 2013.

- [85]. Carbide 3D, “Nomad 883 Pro Specifications,” 2015. [Online]. Available: <http://carbide3d.com/nomad/specs/>. [Accessed: 10-Nov-2016].
- [86]. Analog Devices, “Precision instrumentation amplifier AD624.” p. 8, 1999.
- [87]. M. J. Berka, G. Wang, O. Yadid-Pecht, and M. P. Mintchev, “Method and apparatus for a compact, in-plane skin-penetration device,” 2016 (provisional).
- [88]. M. J. Mosley, C. Mavroidis, and C. Pfeiffer, “Design And Dynamics Of A Shape Memory Alloy Wire Bundle Actuator,” in *Proceedings of the ANS, 8th Topical Meeting on Robotics and Remote Systems*, 1999, pp. 1–14.
- [89]. N. Naomasa, A. Mitsuhiro, Y. Naruse, M. Sadao, and S. Katsuhiko, “Actuator,” US5172551 A1992.
- [90]. H. Asada, K.-J. Cho, and B. Selden, “Shape memory alloy actuator system using segmented binary control,” US111145042007.
- [91]. H. Siekmann, “Recommended maximum temperatures for touchable surfaces,” *Appl. Physiol.*, vol. 21, no. 1, pp. 69–73, 1990.
- [92]. D. Bates, J. Chambers, P. Dalgaard, R. Gentleman, K. Hornik, R. Ihaka, T. Kalibera, M. Lawrence, F. Leisch, U. Ligges, T. Lumley, M. Maechler, M. Morgan, D. Murdoch, P. Murrell, M. Plummer, B. Ripley, D. Sarkar, D. T. Lang, L. Tierney, S. Urbanek, H. Schwarte, G. Masarotto, S. Iacus, and S. Falcon, “R.” The R Foundation for Statistical Computing, 2015.
- [93]. C. Mallett and S. Gray, “AutoHotkey.” AutoHotkey Foundation, LLC, Charleswood, IN, USA, 2009.

Appendix A: R code used in optimization calculations and plots

The following scripts were written for version 3.2.2 of the R language [92] for statistical computing.

Undesired rotational degrees of freedom

The following was used to simulate approximate φ values based on the remaining dimensions identified in Fig. 27 and Fig. 28).

```
#Run for calculation of maximum rotation of lancet shank in slider trench
shank_length = 4 #Length of lancet shank in trench
lancet_diam = .45 #Diameter of shank
trench_width = .60 #Width of space in which shank can move side-to-side

slack = trench_width - lancet_diam #Maximum distance that slider could move without moving
shank

angle_space_list = array(0, c(90, 2)) #Initialize array
found_angle = 0 #Stores maximum angle by which shank may rotate relative to trench in XY plane
for(angle in 1:90) {
  rad_angle = angle*pi/180
  #Contributions of each lancet dimension to filling up the clearance
  width_occupied = lancet_diam*cos(rad_angle)+shank_length*sin(rad_angle)
  angle_space_list[angle, 1] = angle
  angle_space_list[angle, 2] = trench_width - width_occupied #Clearance
  if(angle_space_list[angle-1,2]>0 && angle_space_list[angle,2]<=0){
    found_angle = angle
  }
}

print(found_angle, digits = 0)
```

Simulated lancet paths for ledge-driven rotation

The following was used to generate Fig. 42:

```
#Angle and instantaneous vertical extension, geometry 1
l=3.2 #mm
x1=2 #distance to ledge from starting position of driven part
t1=0.4 #vertical distance between ledge corner and plane of driven part
x<-0:200/100 #201 points, from 0 to 2 mm every 0.01 mm
alpha <- asin(t1*((x1-x)^2+t1^2)^-0.5)*180/pi #skin-lancet angle in degrees
di<-l*t1*(x1-x)*((x1-x)^2+t1^2)^-1.5 #instantaneous rate of vertical descent of needle tip
par(mar=c(5,5,4,5)+.1) #margins
```

```

plot(x, alpha, type="l", col="red3", main="Angle and vertical extension rate versus horizontal
      translation, geometry 1", xlab="Horizontal translation of driven part of needle [mm]",
      ylab="Angle relative to skin [°]")
mylabel1 = bquote(Angle: alpha(x)) #Create label to colour
text(x = 1.5, y = 27, labels = mylabel1, col="red3")
par(new = T) #graphical parameter
plot(x,di,type="l", axes=F, xlab=NA, ylab=NA)

axis(side = 4) #Text to the right
mtext(side = 4, line = 3, "Instantaneous vertical extension of needle towards skin [mm/mm]")
mylabel2 = bquote(Extension: frac(paste(partialdiff, d), paste(partialdiff, x))(x)) #format label
text(x = 1, y = 1.6, labels = mylabel2, col="black") #insert label

```

The following was used to generate Fig. 43:

```

#Visual path, geometry 1
l=3.2
xl=2
t1=0.4
x<-0:50/25
y<-integer(51)
alpha <- asin(t1*((x1-x)^2+t1^2)^-0.5) #Leave as radians for calculations
ly <- -l*sin(alpha)
x2 <- x+l*cos(alpha)
show <- seq(1, length(x), 5) #Select points in driven and tip curves which will be linked by lines
xvec <- cbind(x2, x) #Join for plotting
yvec <- cbind(ly, y)
matplot(xvec, yvec, type="l", lty=3, col=c("red3", "blue3"), ylim=c(-3.2, 0.2), main="Spatial plot
of needle positions during insertion, geometry 1", xlab="Horizontal position (relative to
initial position of upper end of needle) [mm]", ylab="Vertical position (relative to initial
position of upper end of needle) [mm]")
segments(x[show], y[show], x2[show], ly[show]) #Draw lines representing lancet at various
positions

```

The same code was used to generate Fig. 45, with the following minimal changes:

```

t1=1.6
matplot(xvec, yvec, type="l", lty=3, col=c("red3", "blue3"), ylim=c(-3.2,0.2), main="Spatial plot
of needle positions during insertion, geometry 2", xlab="Horizontal position (relative to
initial position of upper end of needle) [mm]", ylab="Vertical position (relative to initial
position of upper end of needle) [mm]")

```

Appendix B: Code of absolute-relative G-code converter

Manual CNC code (see, for example, Appendix C) was mostly prepared using G-Wizard (CNC Cookbook, online), a visual editor. This software was limited in its ability to convert blocks of G-code between absolute and relative coordinates (specifically to take into account which mode was already in use for a particular section of code and to convert the G90/G91 code at the beginning of that block). A simple AutoHotkey [93] utility was prepared for this purpose.

```
SetBatchLines, -1
```

```
TextAreaText := Paste G-code here
```

```
; GUI: https://autohotkey.com/docs/commands/Gui.htm#Position
```

```
Gui, Add, Edit, x0 y2 w300 h300 vTxtArea
```

```
; Create coordinate text boxes with labels:
```

```
Gui, Add, Text, x305 y5 w75 h20, Starting Offsets:
```

```
Gui, Add, Text, x305 yp+20 w10 h20, X
```

```
Gui, Add, Edit, xp+10 yp-2 w65 hp vXOffset, 0
```

```
Gui, Add, Text, x305 yp+25 w10 h20, Y
```

```
Gui, Add, Edit, xp+10 yp-2 w65 hp vYOffset, 0
```

```
Gui, Add, Text, x305 yp+25 w10 h20, Z
```

```
Gui, Add, Edit, xp+10 yp-2 w65 hp vZOffset, 0
```

```
Gui, Add, Button, Default x305 yp+25 w75 h40 gConvertToRel , Convert to Relative
```

```
Gui, Add, Button, Default x305 yp+45 w75 h40 gConvertToAbs , Convert to Absolute
```

```
Gui, Add, Text, Center, (no text)
```

```
Gui, Font, S9, Verdana
```

```
Gui, Show, , G Code Converter
```

```
Return
```

```
; Exit labels:
```

```
AppExit:
```

```
ExitApp
```

```
GuiClose: ;close Gui to Exit
```

```
ExitApp
```

```
ConvertToAbs:
```

```
ConvertEachLine(90) ;90=Absolute
```

```
return
```

```
ConvertToRel:
```

```
ConvertEachLine(91) ;91=Relative
```

return

```
ConvertEachLine(Mode) {
  PosVals := {X: 0, Y: 0, Z:0} ; initialize x, y, z
  For key, value in PosVals {
    OffsetKey := key . "Offset"
    GuiControlGet, OffsetValue, , %OffsetKey%
    if OffsetValue is number
    {
      PosVals[key] := OffsetValue
    }
  }
}

FoundStart := 0
ConvertHere := 1

GuiControlGet, OldText, , TxtArea
Loop, parse, OldText, `n ; Parse by line
{
  NewLine := A_LoopField
  If(InStr(NewLine,"(")<1)
  {
    FoundPos := RegExMatch(A_LoopField, "i)g(90|91)", Match)
    If(FoundPos>0) {
      If(Match1 == Mode) {
        NewLine := "(Originally marked G" . Mode . ", unchanged:)"
        ConvertHere := 0
      } Else If(Mode == 90 || Mode == 91) {
        NewLine := "(Original G" . Match1 . " converted to G" . Mode . ":)"
        ConvertHere := 1
      }
    }
    If(!FoundStart) {
      FoundStart := 1
      NewLine := "G" . Mode
    }
  } Else {
    For key, value in PosVals {
      SearchString := "i)(" . key . ")([0-9\\.\\-]+)" ; i) indicates case insensitive
      FoundPos := RegExMatch(A_LoopField, SearchString, Match)
      If(FoundPos>0) {
        If(!FoundStart) {
          FoundStart := 1
          NewText := "G" . Mode . "`n"
        }
        If(ConvertHere) { ;KEY: PreviousAbsolute + CurrentRelative = CurrentAbsolute
          If(Mode == 90) { ; Rel->Abs:
            Temp := PosVals[key]
```


Appendix C: Manual G-code

The following sections are provided as raw G-code because they were written by hand rather than generated as the result of CAD files which could be given as schematics.

Two-sided base piece

The following code represents manual modification of a .nc file produced by MeshCam, based on the design of Fig. 37.

(FILENAME: Base2.nc)	G1Y65F120	M3S9000
G21	X4	G1 Z-1.4 F80
G90	Y-65	(now a set of 3 in straight,
(TOOL/MILL,1.5875,0.79	X4	relative movements)
375,6.350,0.0)	(end unit, repeat 4.5 times	G91
(start with medium-fine 0.8	to cross part)	G0 X1.4 Y-3.20
mm)	Y65	G1 Z-4.6 F80
M6 T15997	X4	Y10
G0 X0.000 Y0.000 Z3.800	Y-65	Z4.6
(drill 4 symmetric	X4	G0 X1.6
openings)	y65	G1 Z-4.6
G0 X-27 Y20	X4	Y-10
M3 S9000	Y-65	Z4.6
G1 Z-3 f80	X4	G0 X1.600
Z3.8	Y65	G1 Z-4.6
G0 X25 Y20	X4	Y10
G1 Z-3	Y-65	Z4.6
Z4	X4	(move over and next 3:)
G0 x25 Y-20	Y65	G0 X6.2
G1 Z-3	X4	G1 Z-4.6
Z4	Y-65	Y-10
G0 X-27 Y-20	X4	Z4.6
G1 Z-3 F80	Y65	G0 X1.6
Z4	G90	G1 Z-4.6
(rough bit to reduce 2 mm	(surface thinned, switch to	Y10
to 1.2)	finer bit)	Z4.6
M6 T112	Z4	G0 X1.600
(make sure it's measuring	M6 T15997	G1 Z-4.6
AFTER the change)	(drive nails through	Y-10
G0X-20Y-30Z10	openings and into	Z4.6
M3 S9000	wasteboard)	(done with repetitive
G1Z-0.8F80	(before parallel tracks:	motions, back to
G91	4mm above surface)	absolute:)
(basic repetition unit for	(surface now at Z=-0.8)	G90
smoothing)	G0 X-9.4 Y0 Z3.2	

(switch to 0.4 mm for top of channel)
M5
M6 T15995
M3 S9000
(zero over the center of the hole, the point that goes clear through)
G0 X-9.4 Y0.000 Z40
G1 Z3.2 F70
G1 Z-2
(back up and sideways for top part of channel:)
Z-1.6
Y5
(out, sideways to 2nd channel)
Z3.2
G0 X0 Y0
G1 Z-2
(back up and sideways for top part of channel:)
Z-1.6
Y5
Z3.2
(out, stop, space to reverse board:)
M5
(tool change causes Carbide Motion to wait for permission to continue:)
M6 T15995
(remove nails, flip board 180° around x-axis:)
(now upside-down and back-forwards, left-right unchanged)
(insert nails through other side, realign nails

with holes in wasteboard)
(change Y until cutter is over hole, then start:)
G0 Y0 Z6
M3 S9000
G1 Z1 F80
(in, sideways - rotation means that cut is diametrically opposite to previous)
Z-0.8
Y5
(out, sideways to 2nd channel)
Z4
G0 X0 Y0
(back up and sideways for top part of channel:)
G1Z-0.8 F70
Y5
Z4
M5
G0 Z40
(Switch to larger tool)
M6 T112
G0 X0.000 Y0.000 Z6.800
(move to first screw hole)
G0 X0.000 Y0.000 Z6.800
(move to first screw hole)
G0 X-15.05 Y32.07
G0 X-15.751 Y32.833
M3 S9000
G1 Z-2 F70.0
G91
G2 X0 Y0 I0.33 J-0.77 F60
G90
G0 z4
(2nd hole:)
G0 X-15.746 Y-23.163
G1 Z-2 F70.0

G91
G2 X0 Y0 I0.33 J-0.77 F60
G90
G0 z4
(3rd hole:)
G0 X13.25 Y32.836
G1 Z-2 F70.0
G91
G2 X0 Y0 I0.33 J-0.77 F60
G90
G0 z4
(4th hole:)
G0 X13.248 Y-23.165
G1 Z-2 F70.0
G91
G2 X0 Y0 I0.33 J-0.77 F60
G90
G0 z4
(holes done; cut out:)
M3 S9000
G21
G0 X17.443 Y-25.041
G1 Z-2 F70.0
G2 X14.743 Y-27.741 I-2.7 J0 F80
G1 X-16.519 Y-27.743
G2 X-19.219 Y-25.043 I0 J2.7 F80
G1 X-19.218 Y33.143
G2 X-16.518 Y35.843 I2.7 J0
G1 X14.743 Y35.842
G2 X17.443 Y33.142 I0 J-2.7
G1 Y-25.041
(loop done, stop and end)
M5
M30

Aluminum slider

The slider was cut from a 2-mm-thick plate of aluminum stock. It was cut from a corner to reduce the amount of cutting required.

G21	X1.8	Z-0.25
(TOOL/MILL,0.8,0,3,0)	Z-0.25	X2.4
M3 S10000	X-1.8	Y-4.8
	Z1	Z-0.25
(hole 1)		Y4.8
G90	G90	X-2.4
G0 X1.2 Y4.4 Z3		G1 Z-0.25
G1 Z-0.25 F12	(hole 2)	X2.4
Y3.6	G1 X1.2 Y0.4	Y-4.8
Z-0.5	Z-0.25	Z-0.25
Y4.4	Y1.2	Y4.8
Z-0.75	Z-0.5	X-2.4
Y3.6	Y0.4	Z-0.25
Z-2	Z-0.75	X2.4
Z1	Y1.2	Y-3.8
	Z-2	Z-0.25
(trench)	Z1	Y3.8
G1 X0.3 Y2.4		X-2.4
Z-0.25	(outside)	Z-0.25
	G1 X2.4 Y0	X2.4
G91	G90	Y-4.8
X1.8	Z-0.25	
Z-0.25	G91	G90
X-1.8	Y4.8	Z1
Z-0.25	X-2.4	

One-sided base piece for asymmetric actuator

The following was used to produce the simple base piece for the first asymmetric actuator (Chapter 4, “Parallel and asymmetric wire actuation”).

(FILENAME:	G21	G0 X1 Y0 Z5
BaseForMetalSlider.n	G90	(start, move to end surface
c)	(1/4 in. for thinning)	level; +0.05 for tape)
(cut a 35x62 mm	M6 T201	M3 S9000
rectangular base)	(move to 5 mm above plate,	G1 Z1.25
(default: mm/absolute,	3.4 mm above stock	
smooth side up)	surface)	G91

(basic repetition unit for smoothing)

G1Y65F100

X4

(cautious stop before rotation reversal)

M5

(reversing rotation for smoother surface)

M4 S9000

Y-65

X4

M5

M3 S9000

(end unit, 4 more times to cross extents)

(2)

Y65

X4

M5

M4 S9000

Y-65

X4

M5

M3 S9000

(3)

Y65

X4

M5

M4 S9000

Y-65

X4

M5

M3 S9000

(4)

Y65

X4

M5

M4 S9000

Y-65

X4

M5

M3 S9000

(5, exclude last X)

Y65

X4

M5

M4 S9000

Y-65

M5

M3 S9000

G90

(switch to 0.8 mm for slider track)

M6 T15997

(start cutter and enter track) (27.4+.4, 19+.4-.2 due to diameter and round corners)

G0 X27.8 Y19.2 Z5

M3 S9000

G1 Z0.65 F80

(back-and-forth, track l=6.5, w=1.7)

G91

Y6.1

X0.2

M5

M4 S9000

Y-6.1 X0.5

X0.2

M3 S9000

Y6.1

(Y6.1)

(X0.45)

(Y-6.1)

(X0.45)

(Y6.1)

G90

G0 Z5

(only one track in this version)

(Shallow front of channel)

(X:27.4+1.7channel+1gap+.4diam)

(Y:19+1.4slider_end+.4diam)

G0 X30.5 Y20.8

G1 Z1.25

(deeper towards back, slope l=2.5)

G91

Y2.5 Z-0.85

G90

(and straight down for back wall)

Z0

G0 Z5

(1/16 in. for holes and cutout)

M6 T112

(move to 1st screw hole)

G0 X33 Y59 Z5

M3 S9000

G1 Z0 F70.0

(diameter 1.3+0.8)

G91

Y0.65

G2 X0 Y0 I0 J-0.65 F60

G1 Y-0.65

G90

G0 Z5

(2nd hole)

X3 Y59

G1 Z0

G91

Y0.65

G2 X0 Y0 I0 J-0.65 F60

G1 Y-0.65

G90

G0 Z5

(3rd hole)

X3 Y3

G1 Z0

G91

Y0.65

G2 X0 Y0 I0 J-0.65 F60

G1 Y-0.65

G90

G0 Z5

(4th hole)
X33 Y3
G1 Z0
G91
Y0.65
G2 X0 Y0 I0 J-0.65 F60
G1 Y-0.65
G90
G0 Z5
(holes done; cut out with
rounded corners)

(start above lower right
corner - remove thin
edges first)
(0.8mm margin around end
edges; corner radius
1.5mm)
G0 X36.8 Y1.9
G1 Z0 F70.0
G2 X34.1 Y-0.8 I-2.7 J0
F80
G1 X1.9

G2 X-0.8 Y1.9 I0 J2.7 F80
G1 Y60.1
G2 X1.9 Y62.8 I2.7 J0
G1 X34.1
G2 X36.8 Y60.1 I0 J-2.7
G1 Y1.9
G0 Z5

(loop done, stop and end)
M5
M30

Appendix D: Copyright permissions

This thesis contains content for which the copyrights belong to other parties, which have granted conditional permission to reuse the content as follows:

Figures 1, 2 and 33

Figures 1, 2 and 33 are from [27]. The copyright is held by the Institute of Electrical and Electronics Engineers. The IEEE issued the following message through the RightsLink interface (accessible by visiting <http://ieeexplore.ieee.org/document/7527235/>, clicking Request Permissions on the left, then selecting “reuse in a thesis/dissertation”):

Thesis / Dissertation Reuse

The IEEE does not require individuals working on a thesis to obtain a formal reuse license, however, you may print out this statement to be used as a permission grant:

Requirements to be followed when using any portion (e.g., figure, graph, table, or textual material) of an IEEE copyrighted paper in a thesis:

- 1) In the case of textual material (e.g., using short quotes or referring to the work within these papers) users must give full credit to the original source (author, paper, publication) followed by the IEEE copyright line © 2011 IEEE.
- 2) In the case of illustrations or tabular material, we require that the copyright line © [Year of original publication] IEEE appear prominently with each reprinted figure and/or table.
- 3) If a substantial portion of the original paper is to be used, and if you are not the senior author, also obtain the senior author's approval.

The citation and the copyright data are included in each figure’s caption.

Figure 3

The rights to Figure 3 are held by Cancer Research UK (<https://www.cancerresearchuk.org/>), which granted permission to Wikimedia Commons to share the image under a “Creative Commons Attribution-Share Alike 4.0 International” license. This grants the right to distribute and reuse the content given attribution (copyright indicated in the figure caption) and sharing of any modified versions of the content under the same conditions (no changes or additions were made). Wikimedia Commons retains the permission email; details are available at

[https://commons.wikimedia.org/wiki/File:Diagram showing the structure of the skin CRUK 371.svg](https://commons.wikimedia.org/wiki/File:Diagram_showing_the_structure_of_the_skin_CRUK_371.svg).

Figures 15, 21, 22, 24 and 25, and excerpts

Figures 15, 21, 22, 24 and 25, and two block quotes on pages 44 and 46 were produced as part of this research and published in [72]. The IEEE holds the copyright and permitted reuse in this thesis under the same terms as the other IEEE figures (at <http://ieeexplore.ieee.org/document/7808549/>, Request Permissions, then select “reuse in thesis/dissertation”). The citation and copyright data are listed next to each item.